Document Number**:** H2020-ICT-52/RISE-6G/D3.3

Project Name:

Reconfigurable **I**ntelligent **S**ustainable **E**nvironments for **6G** Wireless Networks

RISE-6G

Deliverable D3.3

RISE-6G RISE environment final model

Date of delivery:	31/12/2022	Version:	Final
Start date of Project:	01/01/2021	Duration:	36 months

Deliverable D3.3
RISE-6G RISE environment final model

Project Number:	101017011
Project Name:	**R**econfigurable **I**ntelligent **S**ustainable **E**nvironments for **6G** Wireless Networks

Document Number:	H2020-ICT-52/RISE-6G/D3.3
Document Title:	RISE-6G RISE environment final model
Editor(s):	G. Gradoni (UNOT)
Authors:	UNOT: G. Gradoni, S. Terranova, H. Taghvaee, M. Richter, G. Tanner CEA: R. D'Errico, A. Clemente, G. Makhoul, A. Mudonhi, S. Garbieh, M. Bouslama, M. Tazloum, F. Munoz GNW: Jean Baptiste Gros, Youssef Nasser CNRS: N. M. Di Renzo CNIT : L. Bastianelli, F. Moglie, V. Mariani Primiani, E. Colella TIM: D. Micheli AAU : O. Franek NKUA : G. Alexandropoulos, I. Vinieratou ORA : P. Ratajczak, D.-T. Phan-Huy, Yohann Benedic NEC: P. Mursia, V. Sciancalepore
Dissemination Level:	PU
Contractual Date of Delivery:	31/12/2022
Security:	Public
Status:	Final
Version:	2.0
File Name:	RISE-6G_WP3_D3.3_Final

Content

List of Figures

List of Tables

List of Acronyms

ACF	Autocorrelations Functions
AWGN	Additive White Gaussian Noise
BOI	Band Of Influence
BS	Base Station
CAD	Computer Aided Design
CEA	Commissariat à l'énergie atomique et aux énergies alternatives
CFR	Channel Frequency Response
CG	Channel Gain
CH	Channel Hardening
DC	Direct Current

DEA	Dynamical Energy Analysis
DL	Downlink
DoA	Direction of Arrival
DoD	Direction of Departure
DS	Delay Spread
E2E	End-to-End
EM	Electromagnetic
EMF	Electromagnetic Field
FDTD	Finite Difference Time Domain
GOE	Gaussian Orthogonal Ensemble
GSTCs	Generalized Sheet Transition Conditions
InF	Indoor Factory
IOS	Intelligent Omni-Surface
LOS	Line-of-Sight
MI	Mutual Information
MIMO	Multiple Inputs Multiple Outputs
MGF	Moment Generating Function
MoM	Method of Moment
MPC	Multi-Path Component
NLOS	Non-Line-of-Sight
OLOS	Open Line-of-Sight
OPEX	OPerating EXpenditure
PBC	Periodic Boundary Conditions
PWB	Power Balance Method
PDF	Probability Definition Function
PDP	Power Delay Profile
PEC	Perfect Electric Conductor
RA	Reflect Array
RC	Reverberation Chamber
RCM	Random Coupling Model
RF	Radio Frequency
RT	Ray Tracing
RIS	Reconfigurable Intelligent Surface
Rx	Receiver

SAGE	Space Alternating Generalized Expectation maximization
SDR	Software-Defined Radio
SISO	Single Input Single Output
TA	Transmit Array
Tx	Transmitter
UC	Unit Cell
UE	User
UL	Uplink
UWB	Ultra-Wide Band
US	Uncontrolled Scatterer
VCA	Virtual Cubic Array
VNA	Vector Network Analyser
WDF	Wigner Distribution Function

1 Introduction

NEW: Discuss advancements in scientific literature.

The recent scientific literature has remarked the importance of fundamental RIS modelling for self-consistent network design and coverage planning [DDT21, GDD+21]. The advanced EM models created in RISE-6G are grounded on physics and stand on solid mathematical wave modelling to provide simulation tools that are at the forefront of 6G mobile network research. The scientific community has widely accepted impedance-based RIS design and End-to-End (E2E) channel models [GD21]. Before discussing our project achievements, it is worth mentioning that parallel research has been conducted outside RISE-6G that pertain the following technical aspects:

- Scattering matrix channel model of RIS structures with non-diagonal phase shift matrices [SCM22]
- Accurate current model of finite-size RIS structures by MoM [SA21]
- Impedance model of dynamic Meta-surface antennas including mismatch and insertion loss [WRY+22]
- Equivalent model of finite-size wall-backed RIS structures including mutual coupling [DKT22]
- Diffraction effects in polygonal RIS structures [MM22]
- Analytical model for the reflection coefficient of realistic RIS structures [HMS+22]

In the next sections, we describe the RISE-6G modelling activity in detail, describing its main components, and elaborating a harmonization strategy that brings together all the different angles through which reconfigurable meta-surfaces are characterized. We will start with the *circuital* angle, which takes on full-wave simulations and culminates with simplified equivalent circuits describing the reconfigurable capabilities of the RIS. This angle is prone to integration of

multipath fading via RCM. We then proceed with the *scattering* angle, which includes the reflection coefficients and various mathematical forms of it, useful to capture frequency dispersive and thus achieve wideband channel models. We develop on the scattering angle by devising a wide-band model for the reflection coefficient that captures the resonant behaviour of the RIS UCs. We continue by embracing a *field* angle that culminates into a modified FDTD scheme, useful to further wide-band studies via time-domain computations. The *energy* angle leads to a power conservation model in both free space and confined space, a challenge that is reformulated in *phase-space* to devise energy flow equations within arbitrary indoor environments and thus enable coverage planning studies in real-life environment where idealized assumptions (free space and rich fading) are not fulfilled.

Central to the harmonization strategy is the novel paradigm of environment-aware RIS modelling, whose goal is to predict the best reflection phase matrix of the RIS by including the back-reaction of the environment into the radiative properties of the loaded RIS UCs self-consistently. This integration requires the understanding of the RIS re-radiation properties under spatial and frequency dispersion. To this end, field-based re-radiation scattering models introduced in D3.1 have been extended and exploited to inform high-frequency asymptotic tools. In the next sections, will appreciate the inherent importance of phase-space Ray Tracing (RT) methods to fully capture the physics of re-radiation in a multi-reflective environment. Advanced tools such as Wigner functions have been adopted to fully describe joint positional and directional properties of RIS re-radiation. This boils down to fundamental modelling challenges whose solution is under deep investigation. Preliminary results will be presented on a novel phase-space method for smart wireless environments in limited 2D cases.

Furthermore, in presence of Ricean multipath fading within the RIS-assisted wireless link, we describe how the use of RMT tools give access to better understanding via analytical closed-form and iterative mathematical expressions. We have elaborated ways to incorporate multipath fading within impedance/scattering channel matrix models and have shown a clear relation between uplink/downlink fading parameters and RIS reflection state matrix. An immediate application of those enriched model leads to the prediction of CH in RIS-assisted SISO systems.

1.1 Reflective RIS Design

We present the architecture and the amplitude-phase response of two reflective RIS prototypes operating at two frequency bands in the mmWave and sub-6GHz respectively. While the project activities have produced a wealth of innovative RIS UC architectures, we use the following prototypes as a proxy to show the validity of the impedance-based channel model.

1.1.1 Reflective UC RIS design in the Ka band based on PIN diode

The schematic of the proposed linearly-polarized UC is shown in **Figure 1-1**, It is composed of four metal layers printed on two Isola Astra MT77 substrates ($\varepsilon_r = 3, tan\delta = 0.0017$) and bonded with Astra MT77 pre-preg bonding film ($\varepsilon_r = 2.95, tan\delta = 0.0019$).The top layer is the radiating element. It consists of center-fed O-slot rectangular patch antenna working in reflecting (Rx) mode. The patch antenna is connected by a metalized via hole located at its center to the ground plane. Two pin diodes MA4AGP907 are flip-chipped on the patch antenna to tune the reflection phase; a bias line printed on the opposite side of the substrate controls them. The patch is also connected to a delay line, printed as well on the opposite side of the substrate.

The two pin diodes are biased in opposite states (one pin diode is switched ON while the other one is in OFF state). Due to the presence of the aforementioned delay line, a 90° phase-shift ($\Delta\phi$) of the current distributions is obtained. Since the patch is operating in the reflection mode

thus the reflection coefficients phase shift is equal to $2 \times \Delta\phi$ $(180°)$. The bias networks include microstrip radial stubs to isolate the RF signals. The DC connection to ground is realized with a short circuit stub.

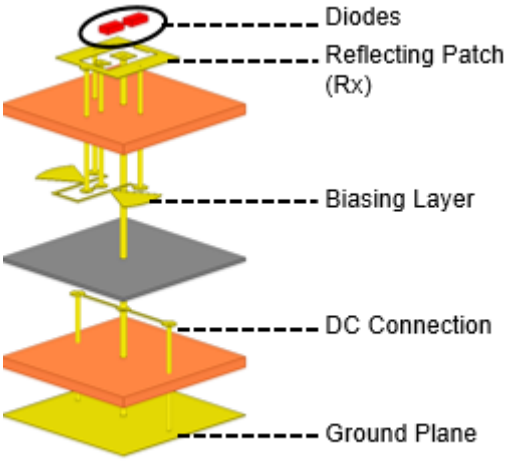

Figure 1-1 Schematic view of the Reflecting RIS UC

The two generated states of the UCs will be referred to as the following: State000 and State180. This 1-bit UC has been simulated for its two-phase states using the commercial software Ansys HFSS with periodic boundary conditions on the UC lateral faces and Floquet port excitation as already explained in the previous section. The UC presents a phase difference of almost $180° \pm 20°$ (the red curve labeled "old" in **Figure 1-2**(b)). The reflection coefficient magnitude is smaller than 2dB over the frequency band for both UC states (the red curve labeled "old" in **Figure 1-2**(a).

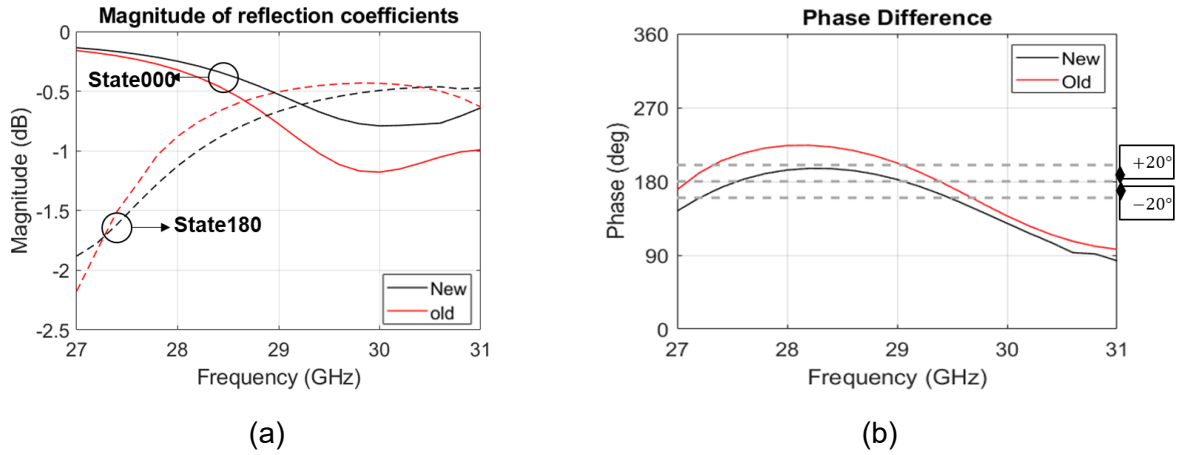

(a) (b)

Figure 1-2 S-parameters Reflecting UC

1.1.2 Reflective UC RIS design in the Sub-6 GHz band based on PIN diode

The schematic of the proposed dual linearly polarized UC operating at a central frequency of 5.2 GHz is shown in **Figure 1-3**. It is composed of one metal layer consisting of two orthogonal folded dipoles and a matching network circuit printed on a thin 0.1 mm FR4 substrate. This FR4 substrate, characterized by $\varepsilon_r = 4.3$ and $tan(\delta) = 0.01$ is placed upon a thick 3mm LERD spacer ($\varepsilon_r = 1.04, tan(\delta) = 0.0001$) and backed by a metallic 1mm ground plane realized with an aluminium reflector. At the top layer, two-radiating elements are present, placed normal to each other to cope two orthogonal polarizations. Two pin diodes are connected to the inner printed matching network and are biased in opposite states (one pin diode is switched ON while the other one is in OFF state).

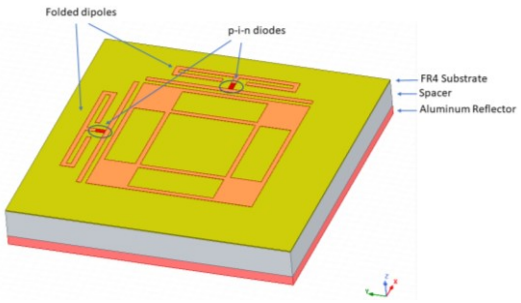

Figure 1-3 Schematic view of the Reflecting RIS UC

By operating in this binary mode, it is possible to obtain a reflection coefficient phase of 0 or 180 degrees, depending on the polarization state of the diodes. This 1-bit UC has been simulated for its two-phase states using the commercial software Ansys HFSS with periodic boundary conditions on the UC lateral faces and Floquet port. As shown in **Figure 1-4**(a) and (b) the UC exhibits a phase difference of almost 180° while the reflection coefficient magnitude is smaller than 2.5dB over the frequency band for both UC states.

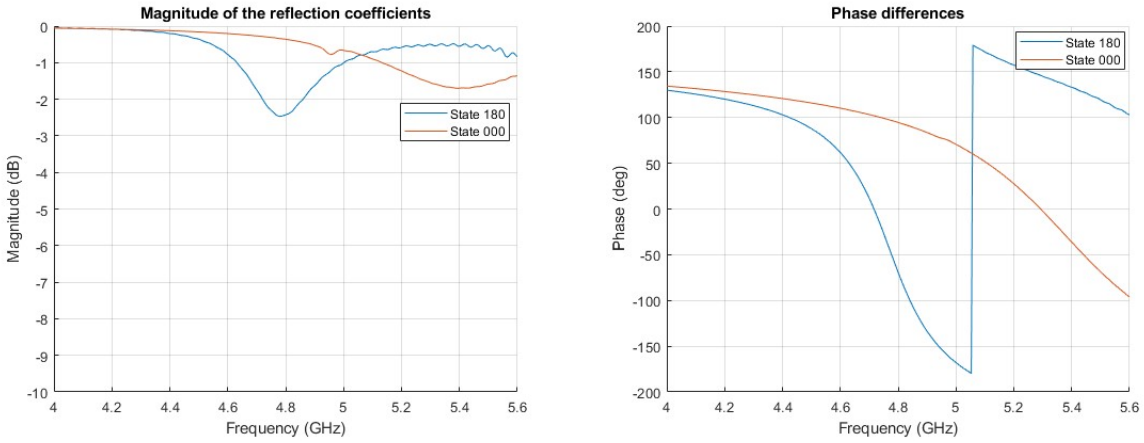

(a) (b)

Figure 1-4 S-parameters Reflecting UC

2 Fundamental RIS modelling

2.1 Discrete model overview

The project activities at M24 have consolidated the original models introduced in D3.1. The focus of the advanced EM modelling research has been on discrete models based on impedance and scattering matrices. Extensions of the free-space models detailed in D3.1 include multipath fading and scattering clusters, as well as frequency dependence over wide bands of operation. Harmonization of the physics-based models with system-level models has been addressed. In particular, the availability of full-wave simulation of the baseline (open-port, non-reconfigurable) structure has been exploited to find mathematical expressions that relate the RIS reflection matrix to the equivalent circuit elements of the RIS UCs. Table 2-1 reports a classification of the advanced EM models developed within RISE-6G, including their main domain of applications and range of validity. The models have been developed through a tight collaboration between academic and industrial project participants, also undertaking measurements campaigns that involve selected sub-6GHz and mmWave prototypes in order to continuously guide and validate the physics-based communication models of the RIS-assisted channel. This choice is oriented to create simulation tools that support design and analysis of the RISE-6G RIS prototypes accounting for the EM environment where they operate upon deployment.

We have elaborated on the importance of defining inherent reconfigurable capabilities of the RIS via the loaded scatterer theory [MH73]. Furthermore, we have assessed the cascaded impedance matrix channel model beyond the dipole array approximation. Specifically, the model presented in D3.1 has been verified for both the GNW (sub-6GHz) and the CEA (mmWave) reflective RIS architectures by extracting all the required active and mutual impedance matrices from commercial full-wave solvers (Dassault Microwave Studio and Ansys HFSS). The impedance-based RIS state matrix has been related to the RIS reflection matrix widely used in wireless communication. This activity sparks more analysis that enables the impedance matrix model to be used in the core technical work packages WP4-WP6.

Table 2-1 Classification of the advanced EM models developed

RIS Model	Range	Environment	State	Function
Impedance	Near/far-field	Free space	Port imp.	Refl/tran
Scattering	Far-field	Rich fading	Port scat.	Refl/tran
Power Bal.	Far-field	Free space	Refl/tran coefficient	Refl/tran
RCM	Far-field	Rich fading	Port imp	Refl/tran
RT	Far-field	Arbitrary	Refl/tran coefficient	Refl/tran
DEA	Far-field	Arbitrary	Refl/tran coefficient	Refl/tran
Resonant	Far-field	Free space	Refl/tran coefficient	Refl/tran

An RMT formulation of the antenna impedance matrix, leading to the RCM, allowed us to integrate the effect of rich multipath fading in the equivalent circuital model of the E2E wireless link. An alternative formulation of the RIS-assisted channel model based on scattering matrix has

been reported for completeness, where a multi-domain strategy based on Huygens boxed has been adopted fruitfully to include rich multipath fading in the LOS channels between Tx/Rx and RIS.

Importantly, in our discrete models we have captured the frequency response of the RIS prototypes through the concept of BOI, introduced in WP6, which describes the largest bandwidth within which specific RIS architectures perturb/change/control the propagation characteristics of the channel. The BOI is related to important RIS design parameters, i.e., quality factor and resonant frequency deviations, of wideband models that we have introduced through the 'inverse Lorentzian' model. A link with power balance methods adopted in WP6, i.e., with focus on EMF assessment besides design, has been established through an augmented FDTD method, which consists of a random plane wave superposition exciting the finite-size RIS structure in time domain. This methodology constitutes a valuable approach for the analysis of wideband RIS-assisted wireless link under multipath fading. This aspect is key for assessing the performance of WP7 testbeds where the fading is emulated by the reverberation chamber. Finally, we devoted special attention to the integration of field based RIS models within classical and phase-space Dynamical Energy Analysis (DEA) RT algorithms. These approaches are also crucial in WP7 as the project activity moves towards smart factory/train station field trials. In fact, while the rich multipath fading assumption is useful for environment-aware design and performance analysis, the assessment of real-life implementation and deployment would no doubt benefit from models that capture more realistic propagation channels.

2.2 End-to-end impedance model validation

2.2.1 Impedance Model of GNW reflective RIS prototypes: Sub-6 GHz

The simulation layout for the RIS prototype briefly presented in section 1.1.2 consists of two co-polarized linear dipole antennas acting as a transmitter and a receiver respectively. The two dipole antennas are placed in the far-field of a reflective RIS consisting of 2×2 UCs. The Tx and Rx dipole antennas, as well as the RIS, operate at a central frequency of 5.2 GHz; the numerical simulations were therefore performed over a wide frequency bandwidth ranging from 4 to 6 GHz. The UC design used to conveniently simulate this finite size reflective RIS has been developed by GNW and has the topology of two folded dipoles to cope both the polarizations, a suitable printed matching network both placed on a FR4 substrate backed by a ground plane. The proposed UC is therefore presented in **Figure 2-1** along with the equivalent circuits of the pin diodes in the ON and OFF state respectively. The prototype has been simulated through Ansys EM HFSS 2022©. The method that we used to verify the E2E model starts by extracting the impedance matrices as described in [GR21]. The interactions between Tx/Rx antenna and RIS UCs are calculated by a frequency domain solver in the form of open circuit impedance matrices. It is interesting to point out that to build the E2E matrix, we have defined discrete ports within the UCs. Those ports are left in open circuit or terminated by an equivalent circuit of the pin diode in turn. Given that each UC has two pin diodes, one for each wave polarization, only the folded dipoles co-polarized with the Tx and Rx dipoles will be used for RIS reconfiguration. However, the general impedance matrix of the E2E system in this configuration consists of 10 ports in total: 8 that will be used for RIS configuration via pin diodes, with the 8 diodes replaced by discrete ports, plus the two feed ports of the dipole antennas. The resulting impedance matrix will therefore have dimensions 10×10.

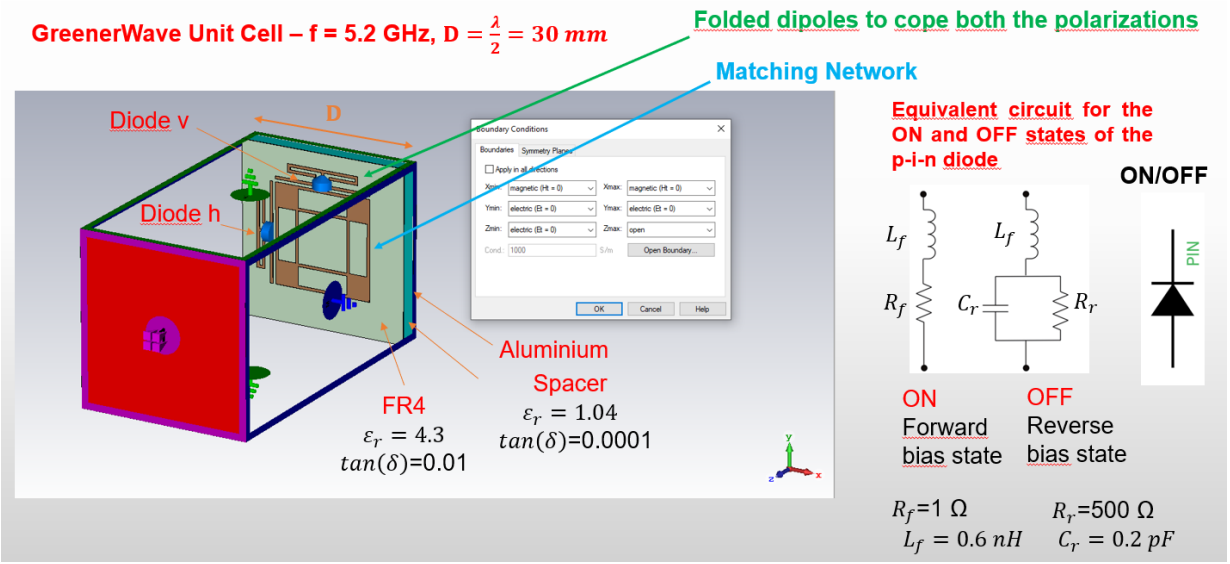

Figure 2-1 . On the left a schematic View of the proposed reflective RIS 1 bit UC. On the right the Equivalent lumped-elements models of the pin diode in the ON and OFF state.

To summarize, the approach employed to validate the E2E transfer function model, starts by determining all impedance matrices comprised in the HE2E model and in particular Z_{RIS} that is the impedance of the reflective RIS structure obtained by switching diode states, Z_{SS} or the active impedance obtained with discrete ports which replaced the pin diodes in a particular ON/OFF state. To calculate the H-matrix, the mutual impedances between the Receiving and Transmitting antennas Z_{RT}, between the Tx antenna and RIS Z_{ST} , and between the receiving antenna and RIS or Z_{RS} will also be considered. To generate all impedances described in the use of the general HE2E model, all scenarios are simulated in Ansys EM HFSS can be described as follows in **Figure 2-2**:

- Scenario 1: In this configuration, all active elements in the reflective RIS UC are changed by lumped ports and the dipole antennas are also excited with lumped ports: the general impedance matrix with all ports (10 ports) is extracted with MATLAB to calculate the E2E transfer function model H_{E2E} of the system. The resulting active impedance Z_{SS} matrix has 10x10 dimensions (8 ports in the R_RIS Structure and 2 in the dipole antennas)
- Scenario 2: The second configuration is presented by active elements placed in 2x2 reflective RIS UCs which are biased in State 000 and only the dipole antennas R/T are excited with lumped ports. Consequently, the impedance Z_{21} (the impedance of the receiver-transmitter) is extracted to be compared with H_{E2E} calculated from the simulation Multi-ports elements.
- Scenario 3: The third configuration is presented by the active elements placed in 2×2 reflective RIS UCs which are biased in State 180 and only the dipole antennas R/T are excited with lumped ports. Therefore, the impedance Z_{21} (the impedance of the receiver-Transmitter) is extracted to be compared with the E2E transfer function model H_{E2E}.

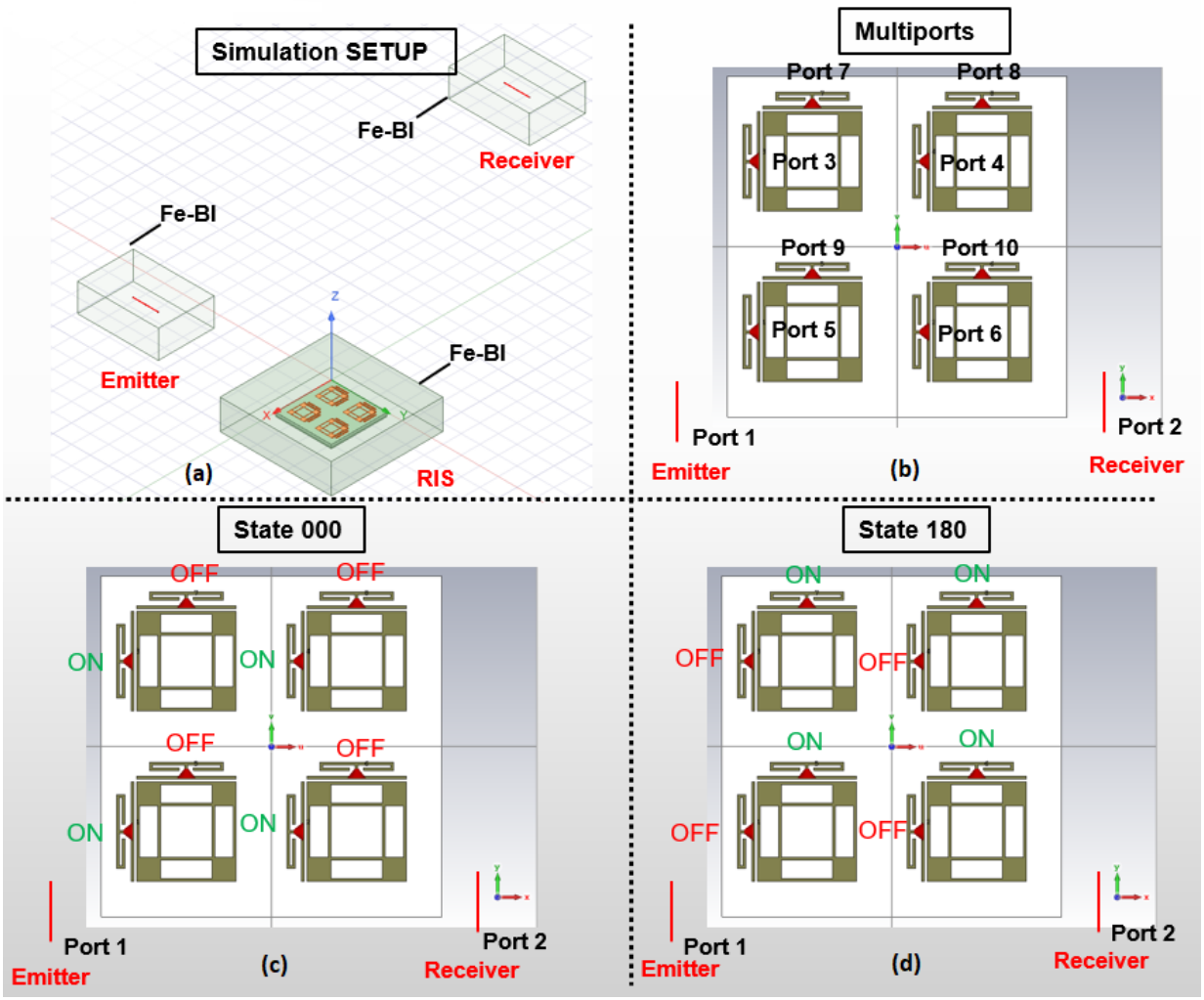

Figure 2-2 (a) Simulation layout of the reflective RIS prototype provided by Greenerwave, (b) Multi-ports reflective RIS configuration, (c) Reflective RIS Configuration in state 0°, (d) Reflective RIS Configuration in state 180°.

In this section, we report the comparison between the predicted E2E transfer function obtained with the proposed model, applied to the reflective RIS design and the impedance Z_{21} extracted from Ansys HFSS obtained with simulations of the loaded RIS in the two states. The simulation results of impedance model have been extracted with a Matlab script, which outputs the total scattering or impedance matrix of the multi-port configurations to validate the E2E transfer function model HE2E. As we can see from **Figure 2-3**, the impedance plots referred to as proposed model are in good agreement with the Z_{21} extracted from the Ansys HFSS simulation with diodes in the $0°$ and $180°$ state cases. Furthermore, we have also extracted active impedance from the UC placed in Periodic Boundary Conditions and used this approach to validate the proposed HE2E transfer modal in the infinite case of reflective RIS arrays.

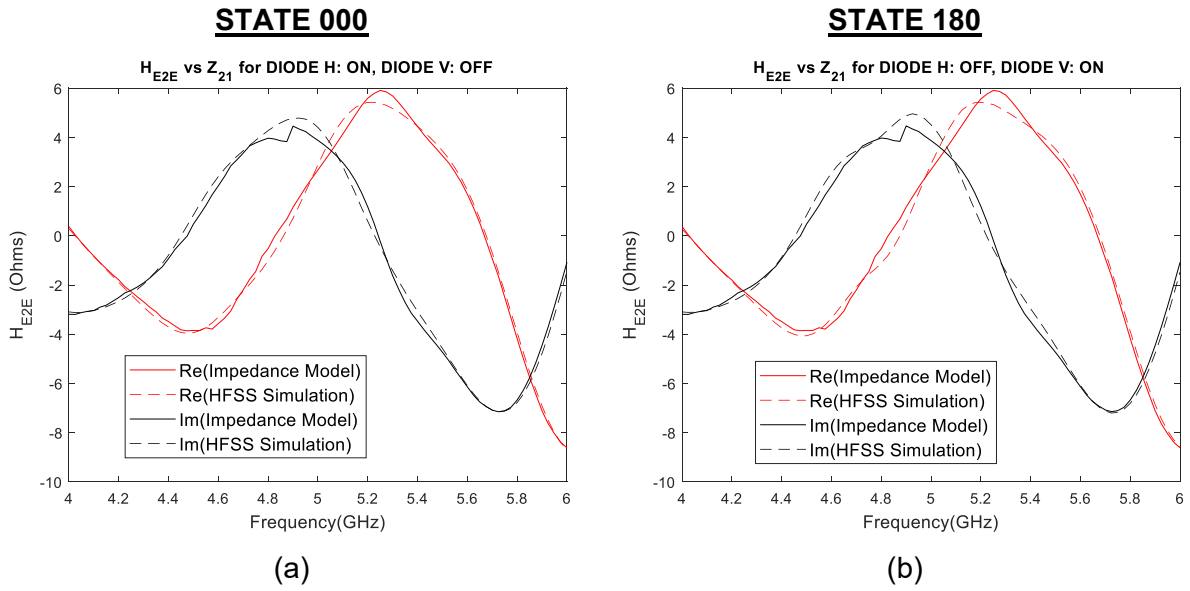

Figure 2-3 Comparison between the real and imaginary part of the Impedance model (red and black solid curves) and the predicted impedance $\boldsymbol{Z_{21}}$ extracted from HFSS Simulator obtained with simulations of the loaded RIS (red and black dashed curves) in case: STATE 000 (a), STATE 180 (b)

As a next step, the validation of the E2E model varying the distance of the receiving antenna from the RIS has been carried out, assuming the Transmitting antenna fixed at a given position. In **Figure 2-4 Schematic view of the setup. The transmitting antenna is supposed fixed and in far field. The receiver is placed at 45° with respect to the normal emerging from the RIS (z-axis) and can vary its position radially from 1 to 4 λ.**a schematic view of the setup is shown while in the **Figure 2-5** are depicted the comparison between the impedance model and the full wave simulation carried out with Ansys HFSS. As the periodicity of the UC is $\lambda/2$, being λ the wavelength of the incident radiation at the central frequency of 5.2 GHz, for this RIS consisting of 2×2 cells, the beginning of the Far-field region will occur at a distance of 4λ. As can be seen from **Figure 2-5** the agreement between simulations and model is valid in the far field but also remains valid for distances of less than 4λ, degrading near the surface, i.e., at λ.

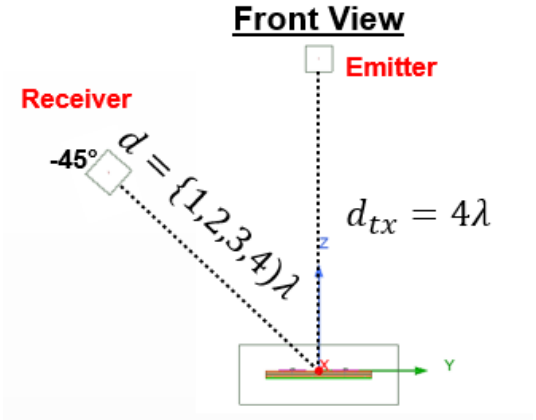

Figure 2-4 Schematic view of the setup. The transmitting antenna is supposed fixed and in far field. The receiver is placed at 45° with respect to the normal emerging from the RIS (z-axis) and can vary its position radially from 1 to 4 $\boldsymbol{\lambda}$.

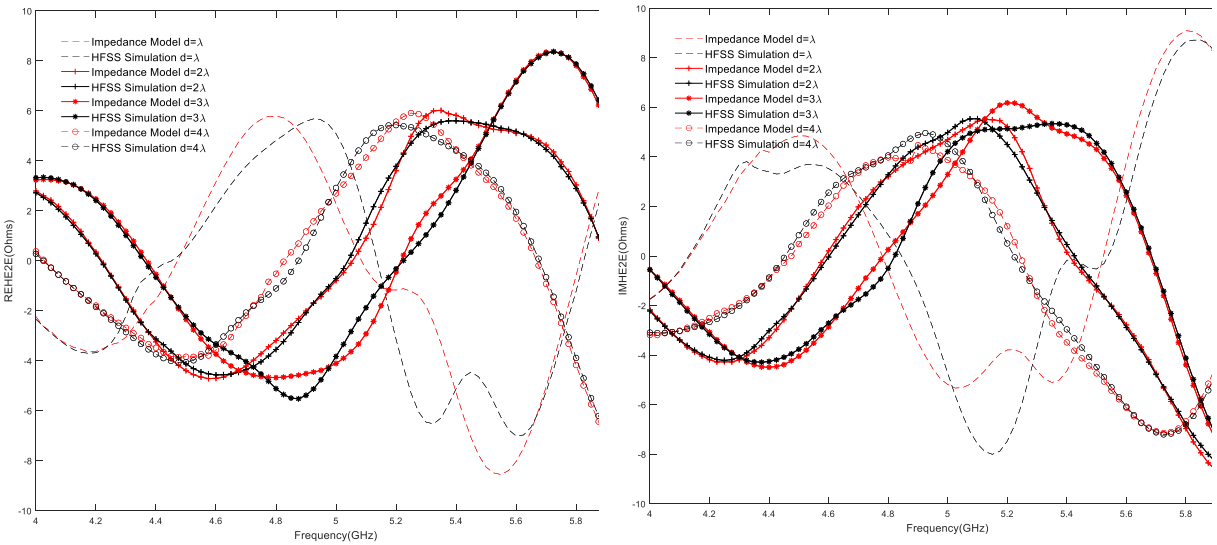

Figure 2-5 Comparison between the real (a) and imaginary (b) part of the Impedance model (red curves) the predicted impedance Z_{21} (black curves) extracted from Ansys HFSS obtained with simulations of the loaded RIS in STATE 0° case. The figures show this comparison at different distance of the receiver from the RIS.

Another interesting validation of the E2E model has been conducted to account for the stability of the results with respect to an angular variation of the receiver, again assuming that the transmitter is kept fixed, as can be seen from the sketch in the **Figure 2-6** and in **Figure 2-7**.

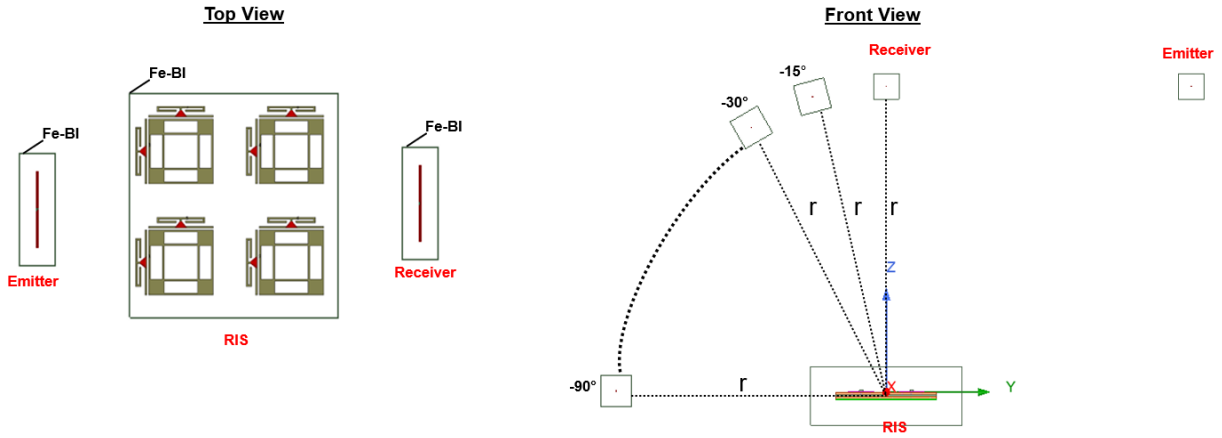

Figure 2-6 Schematic view of the setup. The transmitting antenna is supposed fixed and in far field. The receiver is placed at a distance of $4\,\lambda$ from the RIS and can change its position angularly from $-15°$ to $-90°$, where an angle of $0°$ corresponds to the z-axis.

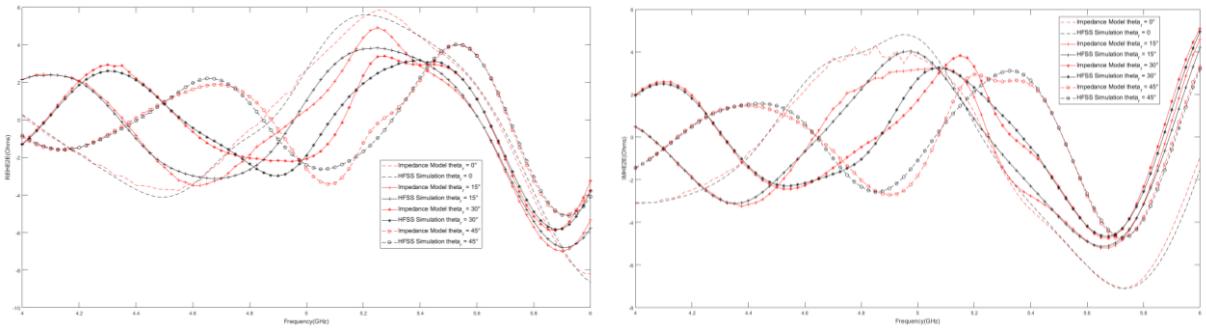

(a) (b)

Figure 2-7 Comparison between the real (a) and imaginary (b) part of the Impedance model (red curves) the predicted impedance $\boldsymbol{Z_{21}}$ (black curves) extracted from Ansys HFSS obtained with simulations of the loaded RIS in STATE 0° case. The figures show this comparison at different angle of the receiver from the RIS maintaining fixed its radial distance.

A final analysis finally turned to the calculation of the so-called active impedance matrix, i.e., the Z_{ss}, both for this presented structure of a 2x2 reflective RIS and for a larger RIS, i.e., a 5x5. A schematic of the two different RISs is reported in **Figure 2-8**.

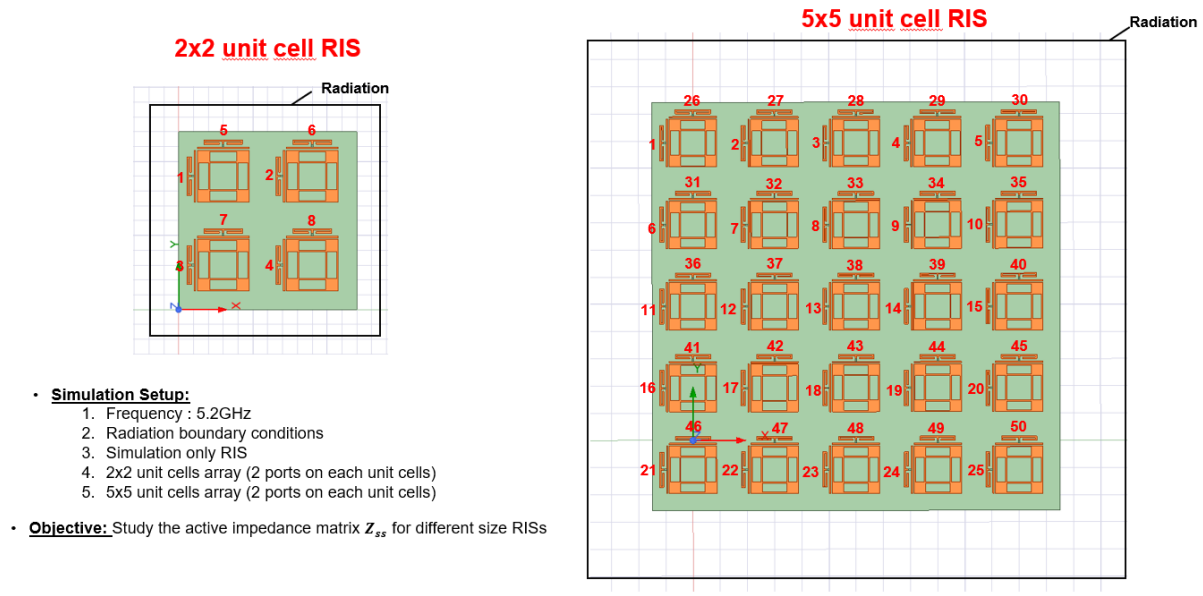

Figure 2-8 Schematic view of the two different RISs: On the left the **2x2** RIS with **2** port for each cell. On the right a **5x5** RIS UC, consisting of **25** elements and **50** ports.

In figure **Figure 2-9** (a) and (b), the real and imaginary part of the active impedance matrix for both $2x2$ and $5x5$ RIS are thus shown. It is interesting to note that by increasing the dimension of the RIS structure from 2x2 to 5x5, the active impedance matrix Z_{SS} is more diagonal, i.e., it becomes similar to the Z_{SS} matrix that would be obtained in case of an infinitely extended periodic structure.

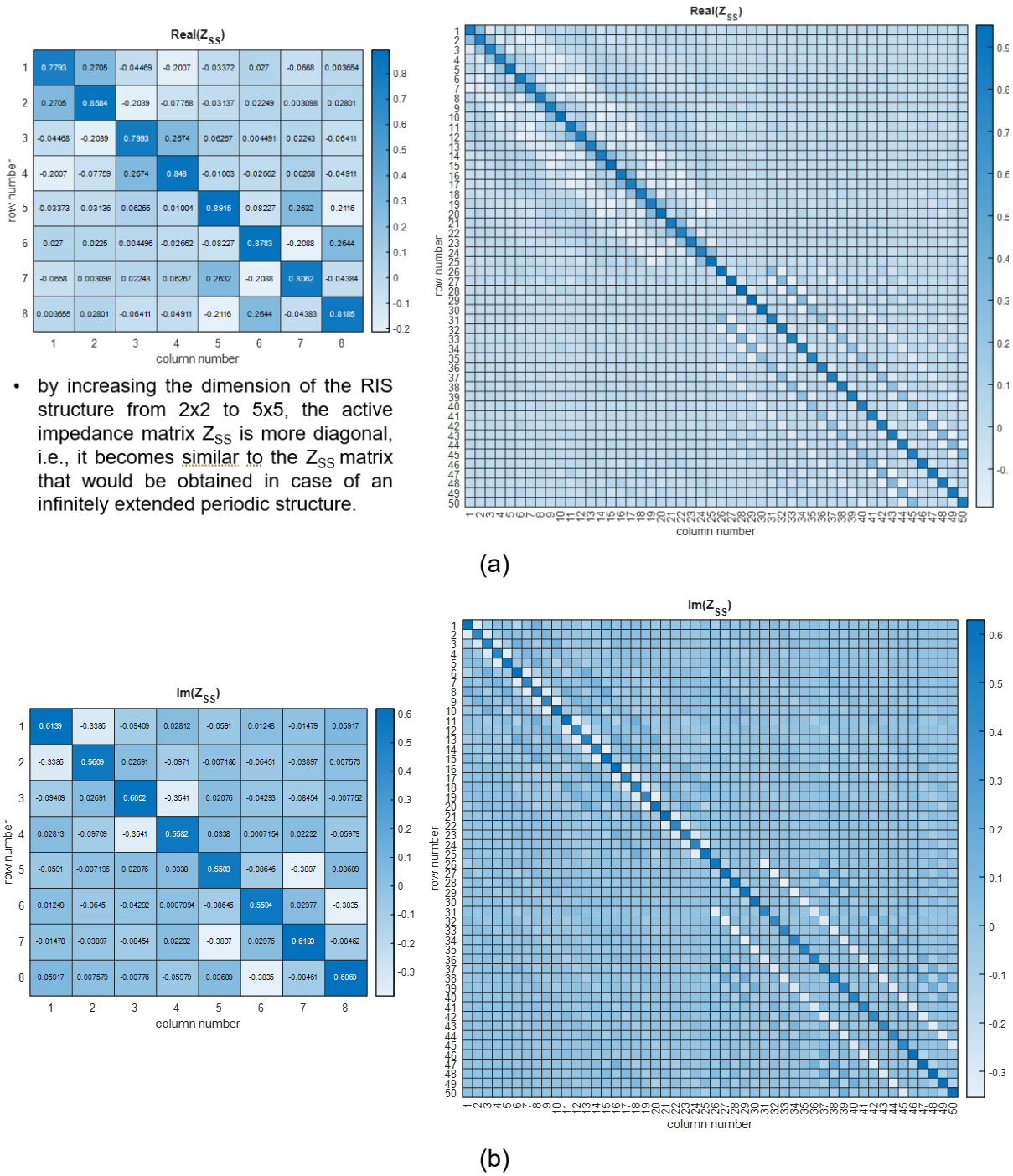

- by increasing the dimension of the RIS structure from 2x2 to 5x5, the active impedance matrix Z_{SS} is more diagonal, i.e., it becomes similar to the Z_{SS} matrix that would be obtained in case of an infinitely extended periodic structure.

Figure 2-9 In (a) real and (b) imaginary part of the active impedance matrix for both $\boldsymbol{2x2}$ and $\boldsymbol{5x5}$ RIS are shown. It is worth mentioning that by increasing the RIS structure, the active impedance matrix Z_{SS} is more diagonal.

2.2.2 Impedance Model of CEA reflective RIS prototypes: mmWave

In this section we analyse the applicability of the impedance model on reflecting RIS based on UC design presented in Section 1.1.1. The configuration model prototype operates in Ka-band. The simulation setup for model validation is represented in **Figure 2-10**. In a first step a full

wave simulation is realized in the two states: namely “000” and “180” as depicted in **Figure 2-10**(a)-(b). Then the diodes are replaced by lumped port to realize a multi-port simulation in order to retrieve the Z_{SS} active impedance matrix. Additionally, a simulation with PBC is performed **Figure 2-10** (d).

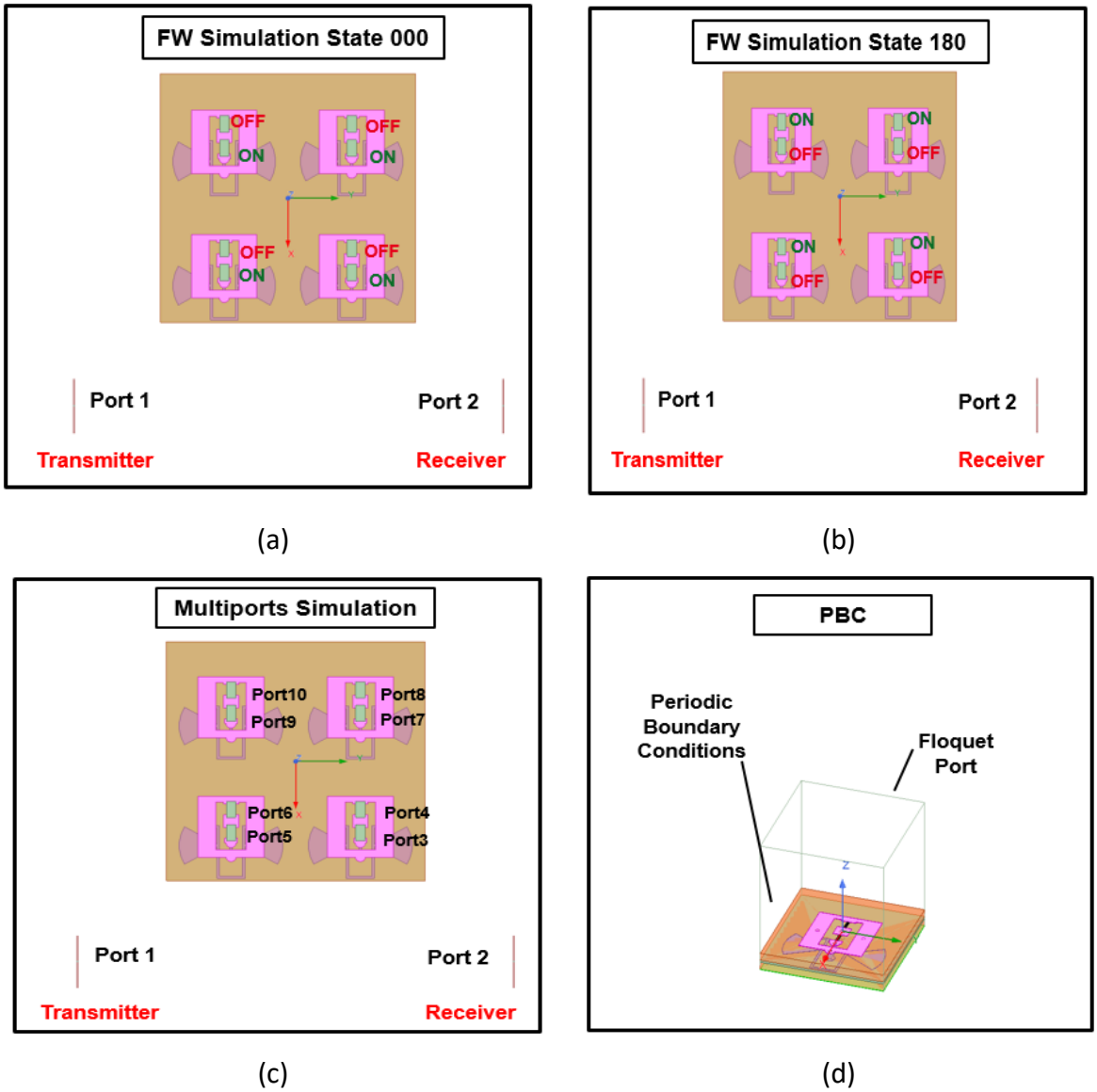

Figure 2-10 (a) Reflective RIS Configuration in state $\mathbf{0}$°, (b) Reflective RIS Configuration in state $\mathbf{180}$°, (c) Multi-ports Reflective RIS configuration, (d) PBC UC

As an example, we considered a configuration with finite RIS with 2×2 UC elements and two dipole antennas. As shown in **Figure 2-11** the impedance obtained from the model using the multiport simulation data, is in good agreement with the full-wave stimulation for different distances of the antennas from the RIS.

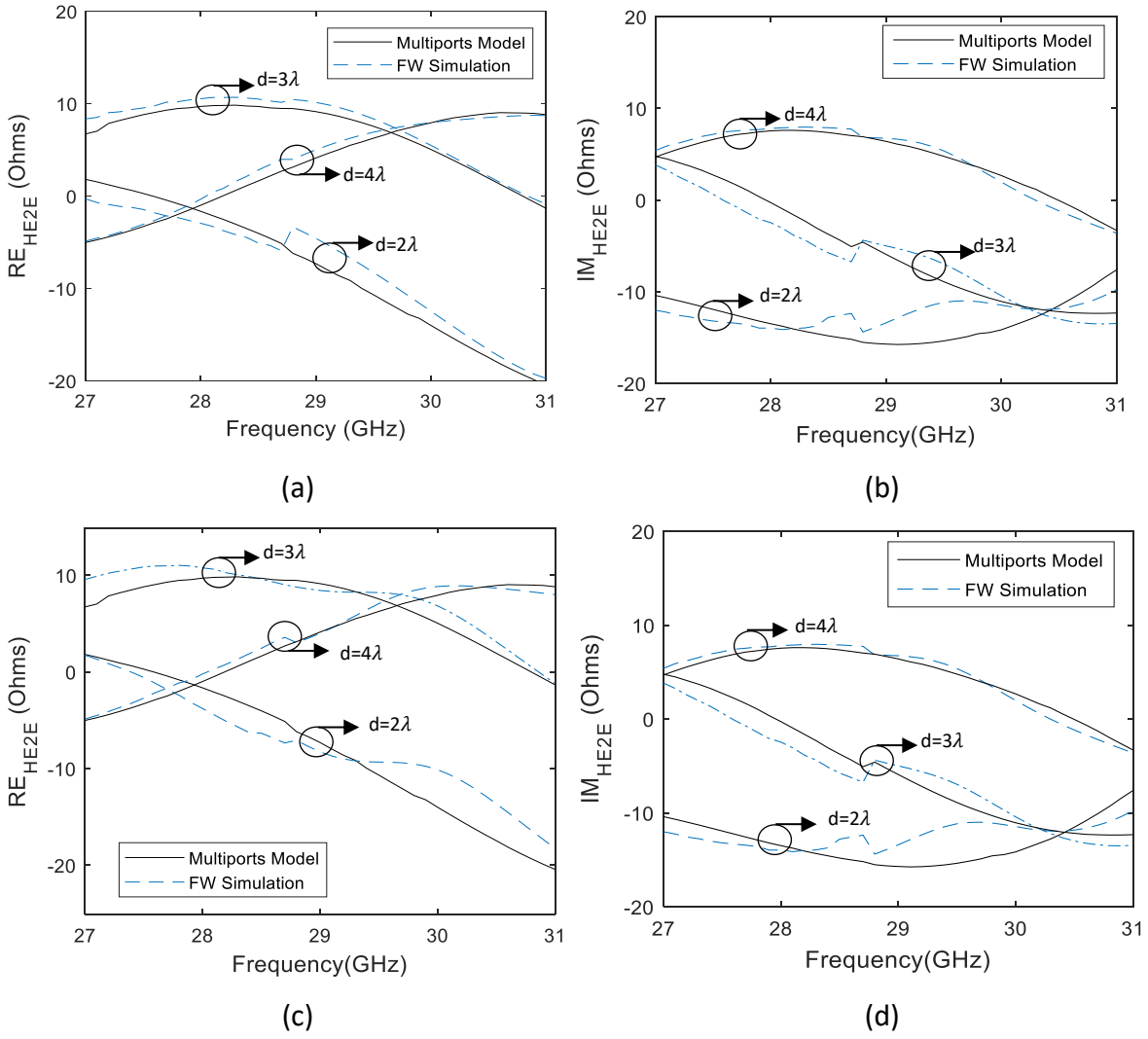

Figure 2-11 (a) Comparison between the impedance model and the impedance Z_{21} extracted from simulation of the RIS for different distances $\boldsymbol{d = \lambda, 2\lambda, 3\lambda, 4\lambda}$: Case **000**: Real part (a), Imaginary Part (b), Case **180**: Real part (c), Imaginary Part (d).

However, in the E2E matrix the mutual coupling between the transmitter and receiver could be higher than the RIS channel itself. Hence, coupling has been subtracted to the full E2E transfer function (i.e., S parameter) of the full wave simulation, to emphasize the RIS impact. In order to evaluate the RIS effect, we considered two cases with all UCs at state "000" or, alternatively, "180". The phase difference between the two channels is shown in **Figure 2-12** (a), when using horn antennas as transmitter and receiver in broadside direction. It can be shown that the phase difference is close to the expected ones. Despite the finite dimensions of the RIS, the phase shift is very close to the one obtained from PBC simulation. Additionally, one of the horn antennas was moved at a different angular position. While the phase difference changes according to the phase, this is still close to the 180° shift expected **Figure 2-12** (b).

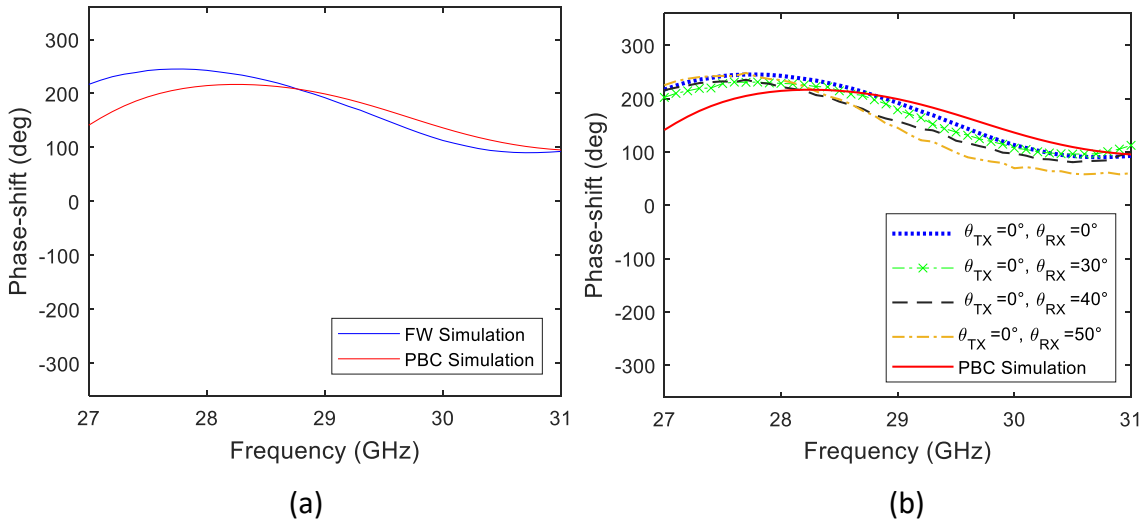

Figure 2-12 Phase shift with finite RIS and two horn antennas (without mutual coupling) in broadside (a) and different receiver angular positions (b)

A preliminary validation of the model is based on the analysis of this shift when using the model as compared to the full wave simulation. In **Figure 2-13** we show the results in the case of single UC or finite 2×2 RIS. The phase shift of the model is roughly in agreement with the full-wave simulation especially at the central frequency. On the extremity of the band, a larger disagreement is found, and the reasons are under investigation and left for further discussion in D3.4.

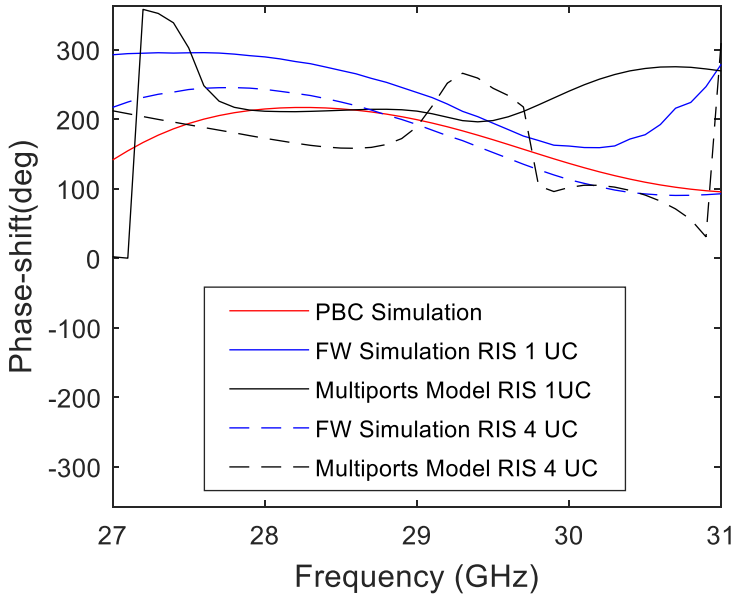

Figure 2-13 Model and full wave simulation phase-shift comparison for different cases.

2.2.3 Modeling the Mutual Coupling of Reconfigurable Meta-surfaces

In this work [RGC22], we have discussed the engineering relevance of considering reconfigurable surfaces whose scattering elements are spaced more densely than half-wavelength, to model the presence of evanescent waves in the close vicinity of the surface, and to be able to control them for realizing extreme manipulations of the EM waves with high power efficiency. In these implementations, the mutual coupling among the scattering elements cannot be ignored. Departing from the approach recently introduced in [GR21] for modeling the mutual coupling among closely spaced scattering elements, we have shown that the E2E channel transfer function matrix can be formulated in a closed-form expression in terms of exponential integral functions, which are built-in functions in state-of-the-art programming and numeric computing platforms. This greatly simplifies the analytical calculation of the E2E channel transfer function matrix in [GR21], and the corresponding optimization of the tuning elements of the surface for maximizing the system performance [QR21], [ADR21].

In [GR21], the authors have recently introduced a circuits-based approach for modeling the mutual coupling of reconfigurable surfaces, which comprise sub-wavelength spaced passive scattering elements coupled with electronic circuits for enabling the reconfiguration of the surface. The approach is based on a finite-length discrete dipole representation of a reconfigurable surface, and on the assumption that the current distribution on each thin wire dipole is a sinusoidal function. Under these assumptions, the voltages at the ports of a Multi-antenna receiver can be formulated in terms of the voltage generators at a multi-antenna transmitter through a transfer function matrix that explicitly depends on the mutual coupling and the tuning circuits through the mutual impedances between every pair of thin wire dipoles. In [GR21], the mutual impedances are formulated in an integral form. In this work, we show that the mutual impedances can be formulated in a closed-form expression in terms of exponential integral functions.

For simplicity, we depart from [GR21, Corollary 1] that is applicable to single-antenna transmitters and single-antenna receivers under the assumption that they are in the far-field of each scattering element that constitutes an electrically large reconfigurable surface made of N reconfigurable elements. Therefore, the model is applicable to the near-field and the far-field regions of the whole surface. For self-consistency, a schematic illustration of the impedance-based model introduced in [GR21] is reported in **Figure 2-14** [RDT22].

The E2E channel can be written as follows:

$$\boldsymbol{h}_{e2e} = \boldsymbol{z}_{\mathbf{RT}} - \boldsymbol{z}_{\mathbf{RS}}^{T}(\mathbf{Z}_{\mathbf{SS}} + \mathbf{Z}_{\mathbf{RIS}})^{-1}\boldsymbol{z}_{\mathbf{ST}} \qquad 2\text{-}1$$

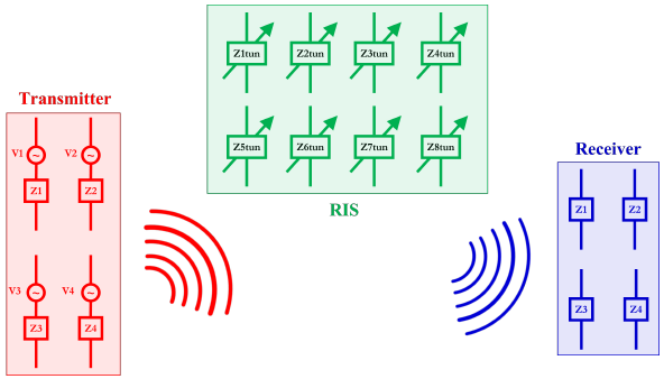

Figure 2-14 Schematic illustration of the impedance-based model for relay-type surfaces introduced in [GR21], [RDT22].

Where z_{RT} is the mutual impedance between the transmitter and the receiver, $\boldsymbol{z}_{\mathrm{RS}}$ is the $N \times 1$ vector of mutual impedances between the N reconfigurable elements of the surface and the receiver, $\boldsymbol{z}_{\mathrm{ST}}$ is the $N \times 1$vector of mutual impedances between the transmitter and the N reconfigurable elements of the surface, $\mathbf{Z}_{\mathrm{RIS}}$ is the $N \times N$ diagonal matrix containing the N equivalent impedances of the tuning circuits enabling the reconfigurability of the surface, and $\mathbf{Z}_{\mathrm{SS}}$ is the $N \times N$ (full) matrix containing the mutual impedances between every pair of scattering elements of the surface. Under the modeling assumptions in [GR21], $\mathbf{Z}_{\mathrm{SS}}$ is independent of $\mathbf{Z}_{\mathrm{RIS}}$.

We are interested in computing the generic element of $\mathbf{Z}_{\mathrm{SS}}$. For ease of writing, let us denote the (qp)th element of $\mathbf{Z}_{\mathrm{SS}}$ by z_{qp}. Specifically, z_{qp} denotes the contribution of the electric field generated by the current flowing through the pth reconfigurable element of the surface when it is observed on the qth reconfigurable element of the surface. From [GR21], we have the following:

$$z_{\mathrm{qp}} = \frac{j\eta}{4\pi k}\int_{-h_q}^{+h_q} \boldsymbol{E}_{qp}(z)\boldsymbol{f}_q(z)\,\boldsymbol{dz} \tag{2-2}$$

$$\boldsymbol{E}_{qp}(z) = (\boldsymbol{\partial}_z^2 + \boldsymbol{k}^2)\int_{-h_p}^{+h_p}\left(\frac{\exp\left(-jkR_{qp}(\xi,z)\right)}{R_{qp}(\xi,z)}\right)\boldsymbol{f}_p(\boldsymbol{\xi})\boldsymbol{d\xi} \tag{2-3}$$

$$\boldsymbol{f}_p(\boldsymbol{\xi}) = \frac{\sin\left(k(h_p-|\xi|)\right)}{\sin(kh_p)}, \quad \boldsymbol{f}_q(\boldsymbol{z}) = \frac{\sin\left(k(h_q-|z|)\right)}{\sin(kh_q)} \tag{2-4}$$

$$\boldsymbol{R}_{qp}(\boldsymbol{\xi},\boldsymbol{z}) = \sqrt{\boldsymbol{d}_{qp}^2 + \left(\boldsymbol{z}_{\mathrm{q}} - \boldsymbol{z}_{\mathrm{p}} + \boldsymbol{z} - \boldsymbol{\xi}\right)^2} \quad \text{if } \boldsymbol{p} \neq \boldsymbol{q} \tag{2-5}$$

$$\boldsymbol{R}_{qp}(\boldsymbol{\xi},\boldsymbol{z}) = \sqrt{\boldsymbol{a}_q^2 + (\boldsymbol{z}-\boldsymbol{\xi})^2} \quad \text{if } \boldsymbol{p} = \boldsymbol{q} \tag{2-6}$$

Where $d_{qp}^2 = \left(x_q - x_p\right)^2 + \left(y_q - y_p\right)^2$. In Eqs. 2-2 to 2-5, the following notation is utilized: h_p and h_q denote the half-length of the pth and qth reconfigurable element, respectively; a_q denotes the radius of the qth reconfigurable element; $(x_p; y_p; z_p)$ and $(x_q; y_q; z_q)$ are the center locations of the pth and qth reconfigurable element, respectively, which are all aligned along the z-axis; $k = 2\pi/\lambda$ where λ is the wavelength; η is the intrinsic impedance of free space; j is the imaginary unit; and ∂_z^2 is the second-order partial derivative with respect to z. The computation of z_{qp} requires the calculation of the electric field in Eq. 2-3 and then the integral in Eq. 2-2.

The electric field in Eq. 2-3 can be formulated in a closed-form expression by applying the approach proposed in [O16, Section 25.1]. The result is the following:

$$E_{qp}(z) = k\frac{\exp\left(-jkR_{qp}(\xi=+h_p,z)\right)}{R_{qp}(\xi=+h_p,z)} + k\frac{\exp\left(-jkR_{qp}(\xi=-h_p,z)\right)}{R_{qp}(\xi=-h_p,z)}$$

$$-\,\boldsymbol{2k\cos(kh_p)}\frac{\exp\left(-jk\boldsymbol{R}_{qp}(\boldsymbol{\xi}=\boldsymbol{0},\boldsymbol{z})\right)}{\boldsymbol{R}_{qp}(\boldsymbol{\xi}=\boldsymbol{0},\boldsymbol{z})} \tag{2-7}$$

Given the closed-form expression of the electric field in Eq. 2-6, z_{qp} can be formulated in terms of exponential integral functions. Specifically, we first rewrite the function $f_{\mathrm{q}}(\mathrm{z})$ as follows:

$$f_q(z) = \frac{1}{2j\sin(kh_q)} \times \sum_{s_0=\{-1,+1\}} s_0 \exp\left(js_0kh_q\right)\exp(-js_0k|z|)$$

$$z_{\mathrm{qp}} = \frac{\eta c_q}{8\pi}\sum_{s_0=\{-1,+1\}} s_0 \exp\left(js_0kh_q\right) I_{qp}(\xi_p = +h_p; s_0)$$

$$+\,\frac{\eta c_q}{8\pi}\sum_{s_0=\{-1,+1\}} s_0 \exp\left(js_0kh_q\right) I_{qp}(\xi_p = -h_p; s_0)$$

$$-\frac{\eta c_{qp}}{8\pi}\sum_{s_0=\{-1,+1\}} s_0 \exp(js_0 kh_q)\, I_{qp}\left(\xi_p = 0; s_0\right) \quad \text{2-8}$$

where $c_q = 1/\sin(kh_q)$, $c_{qp} = 2\cos(kh_p)c_q$, and

$$I_{qp}(\xi_p; s_0) = \int_{-h_q}^{0} \frac{\exp\left(-jk\sqrt{\rho_{qp}^2 + \left(z-\xi_p\right)^2}\right)}{\sqrt{\rho_{qp}^2 + \left(z-\xi_p\right)^2}} \exp(js_0 kz)\, dz$$

$$+\int_{0}^{+h_q} \frac{\exp\left(-jk\sqrt{\rho_{qp}^2 + \left(z-\xi_p\right)^2}\right)}{\sqrt{\rho_{qp}^2 + \left(z-\xi_p\right)^2}} \exp(js_0 kz)\, dz \quad \text{2-9}$$

with $\rho_{qp}^2 = d_{qp}^2$ if $p \neq q$ and $\rho_{qp}^2 = a_q^2$ if $p = q$, respectively. The integral in Eq. 2-9 can be formulated in terms of exponential integral functions by applying the change of variable in [O16, Appendix G]. Specifically, the following notable integral holds:

$$\int_L^U \exp(-jks_0\zeta) \frac{\exp\left(-jk\sqrt{d_0^2 + (\zeta - z_0)^2}\right)}{\sqrt{d_0^2 + (\zeta - z_0)^2}} d\zeta$$
$$= s_0 \exp\left(-jks_0 z_0\right) E_1(jkL_0)$$
$$- s_0 \exp\left(-jks_0 z_0\right) E_1(jkU_0)$$
$$L_0 = \sqrt{d_0^2 + (L - z_0)^2} + s_0(L - z_0)$$
$$U_0 = \sqrt{d_0^2 + (U - z_0)^2} + s_0(U - z_0)$$

$$E_1(c) = \int_c^{\infty} \frac{\exp(-u)}{u} du \quad \text{2-10}$$

Where $E_1(c)$ is the exponential integral function with c being a complex number whose phase is such that $|\arg(c)| \leq \pi$.

2.2.4 Model for joint transmitting and reflecting RIS

The IOS is a dynamic meta-surface that has recently been proposed to achieve full-dimensional communications by realizing the dual function of anomalous reflection and anomalous refraction. In this work [ZZD22], we have proposed a new reflection-refraction model for the reconfigurable elements of IOSs. The circuit-based model has been verified through full-wave EM simulations. Based on the obtained equivalent circuit model, we have demonstrated the influence of the angle of incidence and the IOS structure on the reflection and transmission coefficients. Also, we have studied the asymmetry between the reflection and transmission coefficients. Moreover, the proposed circuit-based model has been integrated into a mathematical framework for jointly optimizing the digital beamformer at the transmitter and the analog beamformer at the IOS. To verify the theoretical findings and evaluate the performance of the full-dimensional beamforming, we have implemented an IOS hardware prototype and have deployed an IOS-assisted wireless communication testbed and have experimentally characterized the beam pattern of the IOS and the achievable rate.

Existing research works provide only simplified models for the reflection and refraction responses of the IOS, which do not explicitly depend on the physical structure of the IOS and the angle of incidence of the EM wave. Therefore, the available reflection-refraction models are insufficient to characterize the performance of full-dimensional communications. In this work, we propose a complete and detailed circuit-based reflection-refraction model for the IOS, which

is formulated in terms of the physical structure and equivalent circuits of the IOS elements, as well as we validate it against full-wave EM simulations.

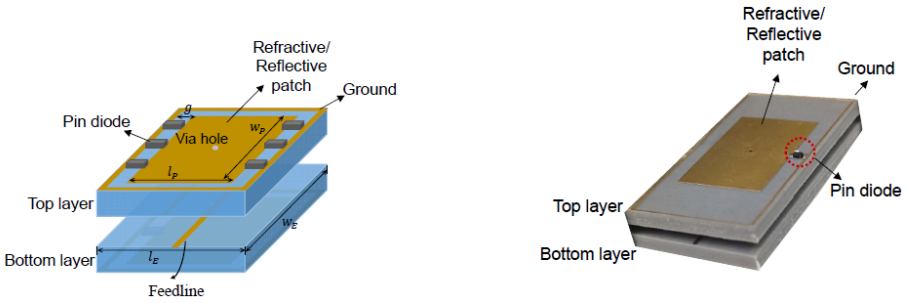

(a) Structure of an IOS element (b) Photo of an implemented IOS element

Figure 2-15: Structure and one example of an IOS element

An IOS is a two-dimensional array of electrically controllable scattering elements with equal size. Each reconfigurable element consists of two symmetrical layers, and each layer contains one metallic patch and N PIN diodes that are evenly distributed on a dielectric substrate, as shown in **Figure 2-15**. The metallic patch is connected to the ground via the PIN diodes. According to predetermined bias voltages, the PIN diodes can be switched between their ON and OFF states, and the state of each IOS element is determined by the states of the PIN diodes on the element. At the bottom of each layer, there is a feedline that is connected to the metallic patch through a via hole. The feedline is utilized to provide the required bias voltages to the PIN diodes. Therefore, the reflection and refraction properties of the IOS element depend on the state of the element, i.e., the configuration of the PIN diodes. Among all the possible states of the IOS element, N_S states are selected to control the EM waves. The set of selected states is denoted by S. To completely characterize the reflective and refractive characteristics of the IOS, a model for the reflection and transmission coefficients is required.

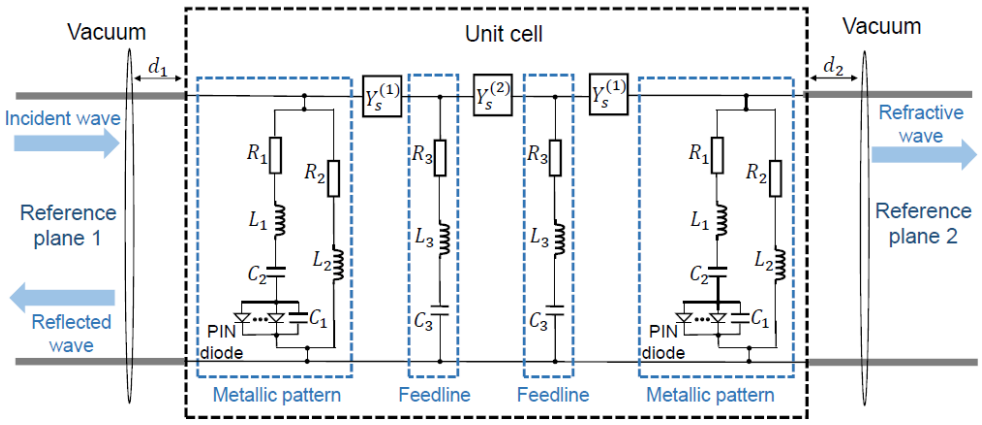

Figure 2-16: Equivalent circuit model of the IOS element

To model the reflection and refraction properties of an IOS element, we introduce an equivalent circuit model, as shown in **Figure 2-16**. Each metallic layer of the IOS element is modeled with an equivalent parallel admittance that is represented by an RLC circuit. The RLC equivalent circuit for the metallic pattern consists of two capacitors, two inductors, one resistor, and several PIN diodes. The RLC equivalent circuit of the feedline is constituted by the series of the resistance, the inductance, and the capacitance.

Based on the equivalent two-port network illustrated in **Figure 2-16**, the ABCD transmission matrix of the obtained network can be expressed as [P05]:

$$\begin{bmatrix} A & B \\ C & D \end{bmatrix} = \begin{bmatrix} 1 & 0 \\ Y_p^{U,M} & 1 \end{bmatrix} \begin{bmatrix} 1 & \frac{1}{Y_s^{(1)}} \\ 0 & 1 \end{bmatrix} \begin{bmatrix} 1 & 0 \\ Y_p^{U,F} & 1 \end{bmatrix} \begin{bmatrix} 1 & \frac{1}{Y_s^{(2)}} \\ 0 & 1 \end{bmatrix} \begin{bmatrix} 1 & 0 \\ Y_p^{L,F} & 1 \end{bmatrix} \begin{bmatrix} 1 & \frac{1}{Y_s^{(1)}} \\ 0 & 1 \end{bmatrix} \begin{bmatrix} 1 & 0 \\ Y_p^{L,M} & 1 \end{bmatrix} \quad 2\text{-}11$$

where $Y_p^{U,M}$, $Y_p^{U,F}$, $Y_p^{L,F}$, $Y_p^{L,M}$, $Y_s^{(1)}$, and $Y_s^{(2)}$ denote the parallel admittances that correspond to the metallic pattern on the top layer, the feedline on the top layer, the feedline on the bottom layer, the metallic pattern on the bottom layer, the coupling admittance between the metallic pattern and the feedline, and the coupling admittance between the feedline on the top layer and the feedline on the bottom layer, respectively.

Based on the ABCD transmission matrix, the reflection and transmission coefficients of the considered IOS element can be formulated as [TMN16, Table 4.2]:

$$\Gamma_r = \frac{(A+B/Z_0)-Z_0(C+D/Z_0)}{(A+B/Z_0)+Z_0(C+D/Z_0)} \exp(-j2\beta d_1) \quad 2\text{-}12$$

$$\Gamma_t = \frac{2}{(A+B/Z_0)+Z_0(C+D/Z_0)} \exp(-j\beta(d_1+d_2)) \quad 2\text{-}13$$

where d_1 and d_2 represent the distances between the reference planes and the surface of the IOS element and $\beta = 2\pi/\lambda$ the propagation constant of the equivalent transmission line.

We aim to validate the proposed model with the aid of full-wave EM simulations. To this end, we consider an implementation of the IOS element, and compare the reflection and transmission coefficients against those obtained by using a full-wave simulator. In the considered example, each IOS element is assumed to be reconfigurable according to two states: both PIN diodes are set to the ON state, i.e., the state (ON, ON), and both diodes are set to the OFF state, i.e., the state (OFF, OFF).

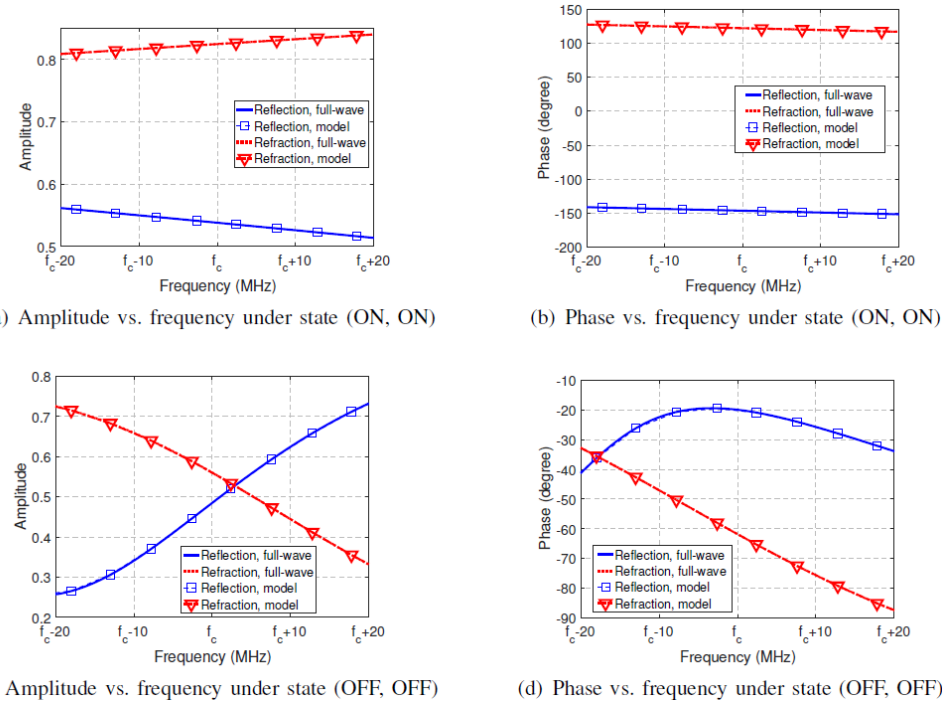

(a) Amplitude vs. frequency under state (ON, ON)

(b) Phase vs. frequency under state (ON, ON)

(c) Amplitude vs. frequency under state (OFF, OFF)

(d) Phase vs. frequency under state (OFF, OFF)

Figure 2-17: Amplitude and phase responses of the IOS element versus the operating frequency under normal incidence. Comparison between full-wave simulations and the proposed model ($f_c = 3.6\,GHz$)

The comparison between the full-wave simulations and the proposed circuit-based model is reported in **Figure 2-17**. The obtained results show that the proposed model provides a good accuracy for the considered case study.

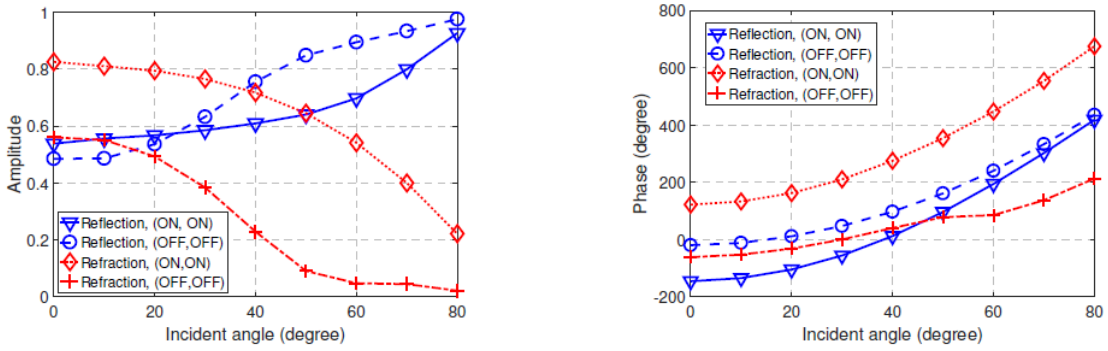

(a) Amplitude vs. the angle of incidence

(b) Phase vs. the angle of incidence

Figure 2-18: Full-wave simulations of the reflection and transmission coefficients vs. the angle of incidence. The operating frequency is 3.6 GHz.

Figure 2-18 confirms that the reflection and transmission coefficients depend on the angle of incidence. From **Figure 2-18**(a), we see that the amplitude of the reflection and transmission coefficients increases and decreases, respectively, with the angle of incidence. This implies that, in general, the amount of power that is reflected and refracted depends on the angle of incidence. From **Figure 2-18**(b), we see that the designed IOS element offers, however, better performance in refraction than in reflection. The reason is that the phase difference between the two states of the IOS element is approximately equal to 180° for the refracted wave, while it tends to shrink for the reflected wave as the angle of incidence increases. This implies that, for the reflected waves, it is not possible to impose the required phase shift on the waves that

impinge on the IOS from a wide angle of incidence. Good reflection capabilities are obtained for angles of incidence that are less than 40°.

2.3 End-to-end field model validation

2.3.1 Electromagnetic model based on Huygens' box

An overview of the proposed electromagnetics-based model is shown in **Figure 2-19**. The RIS is positioned at the origin of spatial coordinates (0,0,0) with its top-layer oriented in the x-direction. The TX and RX represent the participants in the RIS-assisted wireless communication, and may have arbitrary positions in space, provided that the distances between the devices d ensure far-field conditions [B15],

$$\boldsymbol{d} > \frac{\boldsymbol{2D^2}}{\boldsymbol{\lambda}} \qquad \text{2-14}$$

where D is the largest physical dimension of either of the two involved devices, and λ is the wavelength.

The far-field condition Eq. 2-14 is not a "hard" limit, but for lower distances the accuracy of this model quickly deteriorates. The reason for this limitation is twofold. First, if the far-field condition (1) is satisfied, we can assume TX, RX, and RIS to be irradiated by plane waves (or good approximations thereof), which reduces the amount of EM simulations that need to be performed to characterize each device, so that this approach can be considered practical. Second, the plane wave assumption allows to easily incorporate arbitrary complex weights w_{TR}, w_{TS}, w_{RS}, between the devices (T stands for TX, R for RX, and S for the RIS), that can emulate for example fading or blockage using the usual path-loss formalism.

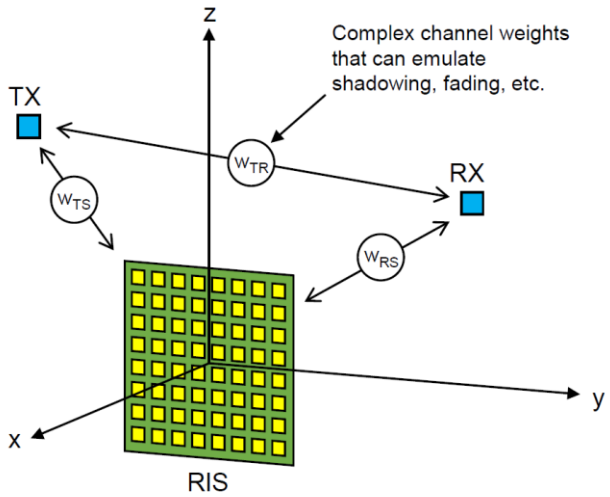

Figure 2-19: Overview of the proposed electromagnetics-based model: The RIS is positioned at the origin of coordinates facing the x-direction, TX and RX represent the wireless communication participants at arbitrary positions; All 3 devices are characterized by EM simulations and communication between them is established via EM plane waves with arbitrary complex weights on each segment.

The EM principle of the RIS channel model is depicted in **Figure 2-20**. The problem of obtaining the communication channel is divided into three parts following the three involved devices: TX, RX, and RIS. For each of these devices, a set of EM simulations is performed to characterize it in terms of incoming and outgoing power waves at each port and incoming and outgoing plane waves in free space. For the latter, a Huygens' box [B12] is formed, entirely enclosing each

device (green dashed rectangles in **Figure 2-20**) and used for a) illuminating the device with plane waves and b) recording of the EM fields radiated or scattered from the device. The recorded fields are then developed using the near-to-far-field transformation into radiation or scattering patterns that express the magnitude and phase of the produced plane wave at the far-field distance.

At this point, the model does not yet know the positions of TX and RX with respect to RIS, as this information will only be provided by the user of the model. Therefore, each device must be electromagnetically characterized in advance, assuming arbitrary positions of the other devices, which could easily lead to excessive number of simulations needed. To keep the approach practical, we chose to illuminate the devices by plane waves (implying far-field conditions (1)) from finite number of spatial directions. In particular, the spatial directions are distributed in a rectangular grid of two spherical coordinates θ and ϕ with predefined angular steps $\Delta\theta$ and $\Delta\phi$. If we denote the sizes of the grid in the θ and ϕ dimensions as $N_\theta = \pi/\Delta\theta$ and $N_\phi = 2\pi/\Delta\phi$, respectively, then the total number of simulations for each polarization will generally be $N = (N_\theta - 1)N_\phi + 2$ (as each "pole" of the spherical coordinate system needs to be counted only once). However, if the device is symmetrical, as is often the case with RIS in the form of planar arrays, we can take advantage of available geometrical and functional symmetries and reduce the number of simulations accordingly.

Each device is characterized by three distinct matrices: 1) the port scattering matrix $\mathbf{S}^{[M\times M]}$, which carries information about coupling between the M ports of the device, 2) the radiation matrix $\mathbf{H}^{[N\times M]}$, which carries information about the radiation (and, by reciprocity, reception) properties of the device in N directions for each port, and 3) the plane wave scattering matrix $\mathbf{\Sigma}^{[N\times N]}$, which carries information about scattering from the device in N directions when illuminated by a plane wave from each of the N directions. In the following, let us assume only single polarization with all the devices. If the simulation engine provides complex values for the radiated E-field of the chosen polarization at 1 m distance in the matrix $\mathbf{E}_{\mathrm{rad}}^{[N\times M]}$, then the radiation matrix can be calculated

$$\mathrm{H} = \mathrm{E}_{\mathrm{rad}} \frac{\lambda \mathrm{e}^{\mathrm{j}k}}{\mathrm{j}\sqrt{\eta_0}} \qquad 2\text{-}15$$

where $k = 2\pi/\lambda$ is the wavenumber, η_0 is the free space wave impedance, and j is the imaginary unit. Similarly, the scattered E-fields at 1 m distance normalized to an incident plane wave of 1 V/m provided in the matrix $\mathbf{E}_{\mathrm{scat}}^{[N\times N]}$ can be converted to the plane wave scattering matrix

$$\mathbf{\Sigma} = \mathrm{E}_{\mathrm{scat}} \frac{\lambda \mathrm{e}^{\mathrm{j}k}}{\mathrm{j}} \qquad 2\text{-}16$$

The three matrices $\mathbf{S}$, $\mathbf{H}$, and $\mathbf{\Sigma}$ are then stored in a file.

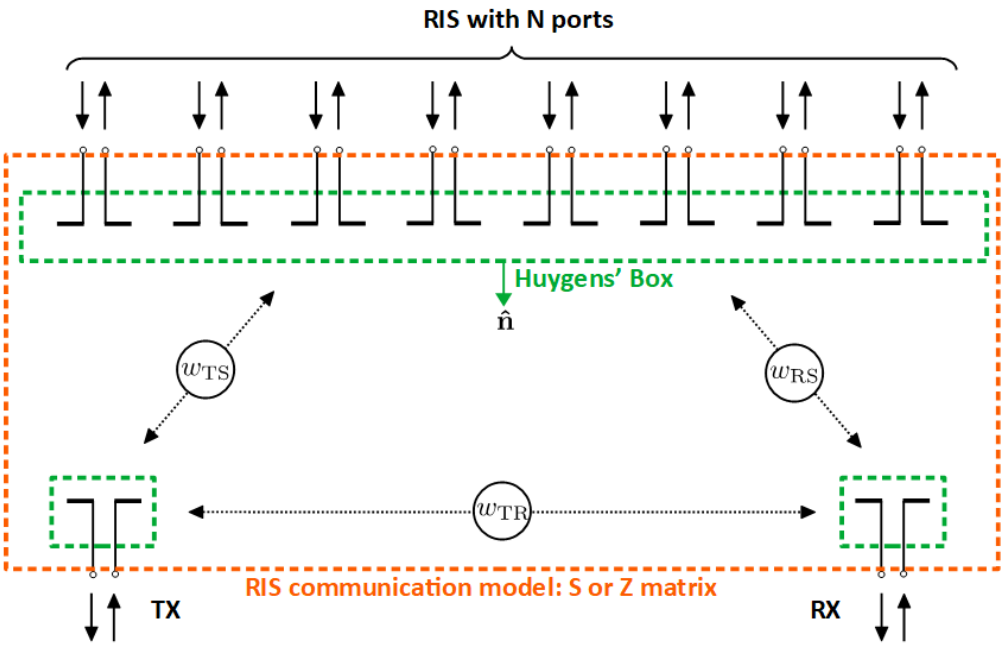

Figure 2-20: Schematic view of the underlying EM model: TX, RX, and RIS are enclosed in Huygens' boxes (green dashed rectangles) that allow plane wave communication between each of these 3 devices with arbitrary channel weights $\boldsymbol{w}_{\mathrm{TR}}$, $\boldsymbol{w}_{\mathrm{TS}}$, $\boldsymbol{w}_{\mathrm{RS}}$; the user is given an S- or Z-matrix of the entire system (red dashed rectangle) that exposes only the ports of the 3 devices.

The final step in obtaining the model is to assemble the three devices into one system, by coupling all pairs of devices with their plane wave ports (dotted arrows in**Figure 2-20**). This step is only possible after the user provides the positions of the TX and RX. First, the precomputed matrices are loaded from the file, and reduced to include only relevant directions, so only those columns corresponding to the directions toward the other devices are retained in $\mathbf{H}$ and the rows and columns with these same indices are retained in $\boldsymbol{\Sigma}$. If the directions do not exactly coincide with the data grid, interpolation may be employed.

All matrices for TX, RX, and RIS are gathered together into system matrices

$$\mathrm{S}_{\mathrm{sys}} = \mathrm{blkdiag}(\mathrm{S}_{\mathrm{TX}}, \mathrm{S}_{\mathrm{RX}}, \mathrm{S}_{\mathrm{RIS}}) \quad 2\text{-}17$$

$$\mathrm{H}_{\mathrm{sys}} = \mathrm{blkdiag}(\mathrm{H}_{\mathrm{TX}}, \mathrm{H}_{\mathrm{RX}}, \mathrm{H}_{\mathrm{RIS}}) \quad 2\text{-}18$$

$$\boldsymbol{\Sigma}_{\mathrm{sys}} = \mathrm{blkdiag}(\boldsymbol{\Sigma}_{\mathrm{TX}}, \boldsymbol{\Sigma}_{\mathrm{RX}}, \boldsymbol{\Sigma}_{\mathrm{RIS}}) \quad 2\text{-}19$$

where $\mathrm{blkdiag}()$ is a shorthand for block diagonal matrix. The three devices are then linked together using free space propagation terms [F17] multiplied by the user-provided complex channel weights

$$\mathrm{F} = \mathrm{diag}\left(\boldsymbol{w}_{\mathrm{TR}} \frac{\mathrm{j}e^{-\mathrm{j}\boldsymbol{k}\boldsymbol{r}_{\mathrm{TR}}}}{\boldsymbol{\lambda}\boldsymbol{r}_{\mathrm{TR}}}, \boldsymbol{w}_{\mathrm{TS}} \frac{\mathrm{j}e^{-\mathrm{j}\boldsymbol{k}\boldsymbol{r}_{\mathrm{TS}}}}{\boldsymbol{\lambda}\boldsymbol{r}_{\mathrm{TS}}}, \boldsymbol{w}_{\mathrm{RS}} \frac{\mathrm{j}e^{-\mathrm{j}\boldsymbol{k}\boldsymbol{r}_{\mathrm{RS}}}}{\boldsymbol{\lambda}\boldsymbol{r}_{\mathrm{RS}}}\right) \quad 2\text{-}20$$

where r_{TR}, r_{TS}, r_{RS} are the geometric distances between the three devices. The path loss matrix $\mathbf{F}$ is instrumental in creating the connector matrix

$$\mathrm{C} = \begin{bmatrix} \mathbf{0} & \mathrm{F} \\ \mathrm{F} & \mathbf{0} \end{bmatrix} \quad 2\text{-}21$$

that is finally used to eliminate the internal plane wave ports to give the user the total scattering matrix $\mathbf{S}_{\mathrm{tot}}$ of the entire system (red dashed rectangle in **Figure 2-20**) with only the physical ports (dual arrows in **Figure 2-20**) of the TX, RX, and RIS exposed,

$$\mathrm{S}_{\mathrm{tot}} = \mathrm{S}_{\mathrm{sys}} + \mathrm{H}_{\mathrm{sys}}^{\mathrm{T}}\left(\mathrm{C}^{-\mathbf{1}} - \boldsymbol{\Sigma}_{\mathrm{sys}}\right)^{-\mathbf{1}}\mathrm{H}_{\mathrm{sys}} \qquad 2\text{-}22$$

If needed, the scattering matrix can be converted to impedance matrix assuming Z_0 is the characteristic impedance of all the ports

$$\mathrm{Z}_{\mathrm{tot}} = \boldsymbol{Z_0}(\mathrm{I} + \mathbf{S}_{\mathrm{tot}})(\mathrm{I} - \mathbf{S}_{\mathrm{tot}})^{-\mathbf{1}} \qquad 2\text{-}23$$

where $\mathbf{I}$ is the identity matrix of the same size as $\mathbf{S}_{\mathrm{tot}}$.

Since the proposed model uses plane waves to link the three communication participants, TX, RX, and RIS, together, the simulations can be performed in off-the-shelf commercial software for EM simulations of antennas, as they usually offer both the plane wave excitation and near-to-far-field transformation. For our implementation, we chose CST Microwave Studio as the simulation engine, and MATLAB for the wrapper function that performs the linking and the interface to the user. The syntax of the MATLAB function is

```
M = ris_matrix( type, filename, ...
                x_TX, y_TX, z_TX, ...
                x_RX, y_RX, z_RX, ...
                w_TR, w_TS, w_RS )
```

where `M` is the resulting matrix that can be the S- or Z-matrix of the entire model (denoted by red dashed rectangle in**Figure 2-20**) depending on the argument `type` being `'S'` or `'Z'`, respectively. Argument `filename` specifies the file in which the precomputed simulation data are stored, `x_TX, y_TX, z_TX` and `x_RX, y_RX, z_RX` are the spatial Cartesian coordinates of the TX and RX, respectively, and finally `w_TR, w_TS, w_RS` are the arbitrary complex weights w_{TR}, w_{TS}, w_{RS}, respectively.

The model has been validated against a full-wave simulation of the scenario described in [GR21] and [QR21] at frequency 28 GHz. The RIS is an $P \times P$ planar array centered at coordinates $(0,0,0)$ facing the x direction. The RIS elements are distributed in a rectangular grid with spacing λ/P, making the electrical size of the RIS approx. $\lambda \times \lambda$. The TX and RX, as well as all the elements of the RIS array, are z-oriented short dipoles with length $\lambda/32$ and radius $\lambda/500$. The TX is positioned at coordinates $(5,-5,3)$ and RX at $(5,5,1)$, measured in meters. The maximum error of the resulting impedance matrix is less than 1.4 % in magnitude (<0.12 dB) and less than 3° in phase.

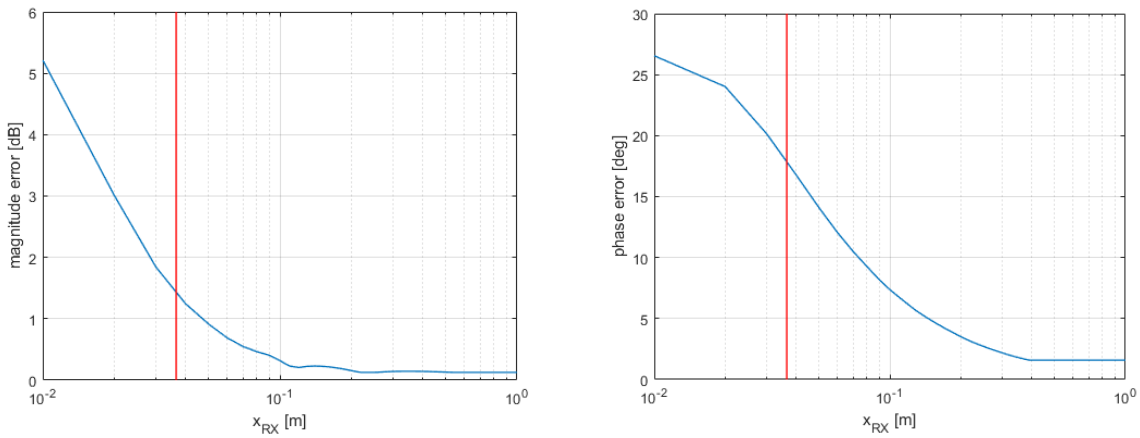

(a) (b)

Figure 2-21: Maximum magnitude (a) and phase (b) errors of the Z-matrix when the RX is placed at position $(\boldsymbol{x_{\mathrm{RX}}}, -\mathbf{0.01}, \mathbf{0.02})$ m. The red line denotes the far field approximation distance from the RIS.

Behavior of the Z-matrix close to the RIS is shown in **Figure 2-21**. Here, the RX is placed at position $(x_{\mathrm{RX}}, -0.01, 0.02)$ m, the x_{RX} coordinate is swept between 10 mm and 1 m, and the magnitude and phase errors of the Z-matrix elements between the proposed model and a full CST simulation are observed. As expected, the errors are dropping with distance, and in the far-field region, which in this case is approximately 4λ (43 mm) as defined by (1), the errors are below 1.5 dB in magnitude and 18° in phase. The latter figure agrees well with [B15], where the far field approximation condition (1) is defined for phase error not exceeding $\pi/8$ (22.5°).

2.3.2 Scattering matrix and power budget model

Previously a hybrid full wave methodology based on analytic expression and full-wave simulations was developed to synthetize and optimize Transmitting-RIS (transmitarray). It was validated with the measurement results up to 330 GHz. This tool has been extended to consider Reflecting-RIS and RA antenna arrays.

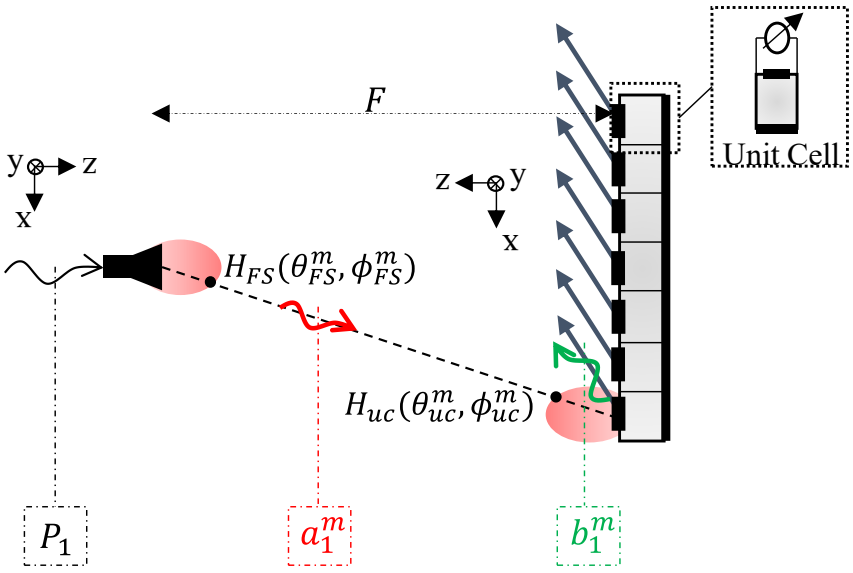

Figure 2-22 Operating principle of the RIS in reflecting mode.

In this section, the model will be presented briefly. The input data in the model are the following: the focal source radiation pattern, the UCs scattering matrix, and their radiation patterns. The data could be considered as ideal cases (ideal UC and ideal source) or could be extracted from full-wave simulations (such as HFSS simulation). The structure in **Figure 2-22** is considered with a RIS of M×M elements. The RA is illuminated by a focal source at a focal distance F. The input power on the focal source is P_1. The complex radiation pattern of the focal source is denoted as $H_{FS}(\theta,\phi)$. The radiation pattern in the m^{th} directions is $H_{FS}(\theta_{FS}^m,\phi_{FS}^m)$; the two components of the pattern in the m^{th} UC direction are $H_{FS}^{\theta^m}$ and $H_{FS}^{\phi^m}$. The complex radiation pattern of the UC is denoted as $H_{uc}(\theta,\phi)$. The radiation pattern in the direction of the focal source is $H_{uc}(\theta_{uc}^m,\phi_{uc}^m)$; the two components of the pattern of the m^{th} UC in the direction of the focal source are $H_{uc}^{\theta^m}$ and $H_{uc}^{\phi^m}$. Therefore, the incident wave received by the m^{th} UC is calculated by the following formula:

$$\boldsymbol{a_1^m} = \frac{\lambda e^{-\frac{j2\pi R_m}{\lambda}}}{4\pi R_m}\left(\boldsymbol{H_{FS}^{\theta^m} H_{uc}^{\theta^m}} + \boldsymbol{H_{FS}^{\phi^m} H_{uc}^{\phi^m}}\right)\sqrt{\boldsymbol{P_1}} \qquad 2\text{-}24$$

where R_m: is the distance between the focal source and the m^{th} UC, and λ : is the wavelength.

The reflected wave by the m^{th} UC is then calculated using the following formula:

$$\boldsymbol{b_1^m} = \boldsymbol{S_{11}^m}.\boldsymbol{a_1^m} \qquad 2\text{-}25$$

where S_{11}^m: is the reflection coefficient of the m^{th} UC.

Finally, the radiation pattern of the reflectarray (H_{RA}^{θ} and H_{RA}^{ϕ}) is computed by the summation of the contribution of each cell, taking into account the reflected wave calculated in Eq. (2-25) and the radiation pattern of the UC for a given pair of (θ,ϕ):

$$\boldsymbol{H_{RA}^{\theta/\phi}(\theta,\phi)} = \boldsymbol{H_{uc}^{\theta/\phi}(\theta,\phi)}\sum_{m=1}^{M}\boldsymbol{b_1^m e^{\frac{j2\pi}{\lambda}(sin\theta cos\phi X_m + sin\theta sin\phi Y_m)}} \qquad 2\text{-}26$$

where X_m and Y_m: are the Cartesian coordinates of the UC (in the plane z = 0, since the RA is placed in the place xoy (**Figure 2-22**).

The MATLAB tool can ensure a full analytical study. Several sweeps could be performed such as: frequency sweep, focal distance sweep, etc... These sweeps help in the optimization of the RA antenna. In **Figure 2-23** an example of 20×20 UCs RA is shown. The analytical results calculated in the developed tool are shown in **Figure 2-24**. The different phase distributions for the steering angles $[-60°:5°:60°]$ are calculated as well as the 2D radiation patterns in the plane $\phi = 0°$ at 29 GHz. The 3D radiation pattern for a reflection towards $30°$ is shown. There are other far-field results that could be extracted from the tool such as other cut planes, the gain vs the frequency, and the efficiency.

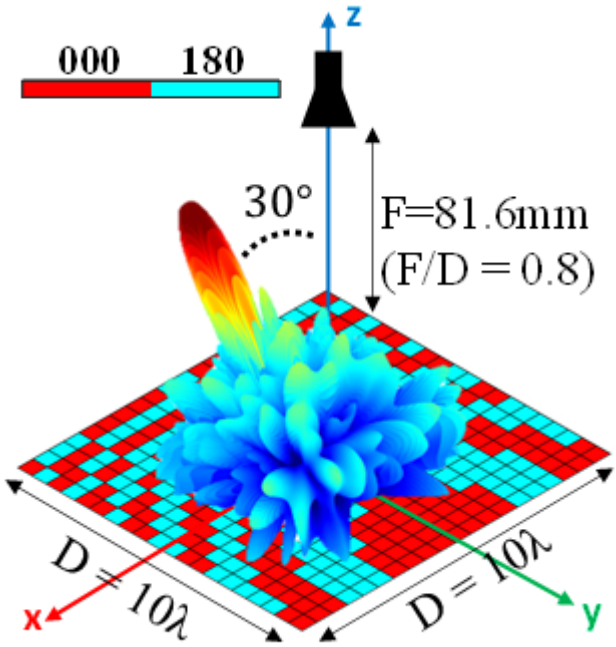

fiu

Figure 2-23 The adopted scenario in the MATLAB Simulation of a RA of 20x20 UCs and the 3D gain pattern in 30° direction.

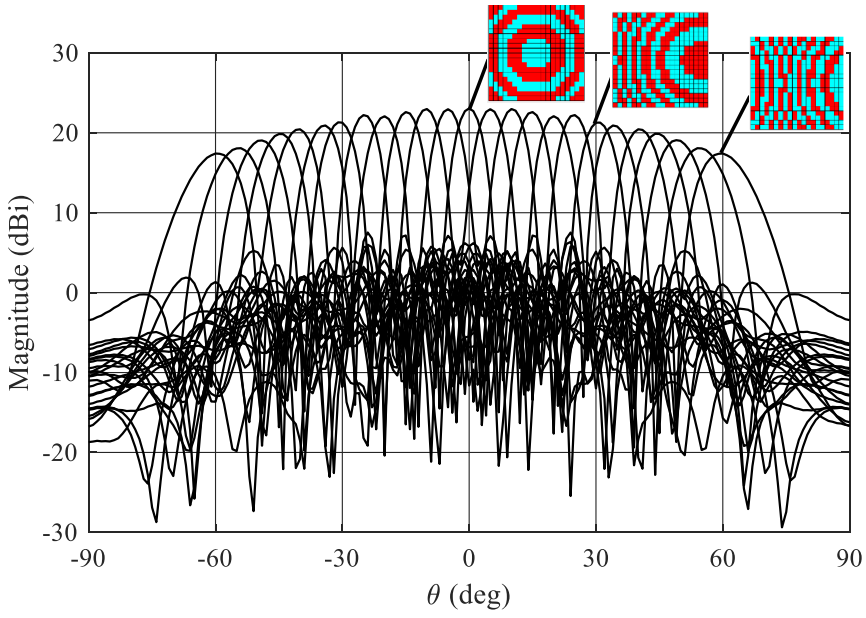

Figure 2-24 The gain patterns for different steering angles are calculated analytically in the Matlab tool for a RA of 20x20 unit cells.

2.3.3 Synthesis and Simulation of 4λ×4λ Reflecting RIS

In order validate the model of the proposed Matlab tool in one hand and to demonstrate the reliability of the designed reconfigurable UC in the other hand, a 8×8 UC ($4\lambda \times 4\lambda, 40.8 \times 40.8$

mm^2) RIS is considered. The RIS is illuminated using a standard 10-dBi horn placed at a focal distance $F = 32$ mm ($F/D = 0.8$). For the sake of simplicity, the horn is placed at the middle of the RA. Since the horn is covering an angle of the reflection plane (see the 3D sketch of the scenario in **Figure 2-25**) thus, the reflection in broadside is not considered in order to avoid the shadowing caused by the horn. The phase distributions for two steering angles are generated: i) Reflection towards $10°$, ii) Reflection towards $30°$. The full RA considering the two-phase distributions is then simulated in HFSS (**Figure 2-26**) with the Finite Element Boundary Integral (FE-BI) solver.

The simulation results are then compared to the MATLAB theoretical results. In **Figure 2-26**, the pattern for the two reflection cases ($10°$ and $30°$) are shown with the corresponding phase distribution. The plots show good agreement between the full-wave simulations and the theoretical results. For the case of the reflection towards $10°$, the maximum gain calculated in Matlab is of 15.71 dB, and of 14.92 dB the maximum gain exported from HFSS which leads to a small difference of 0.8 dB. Whereas in the case of the reflection towards $30°$, the gain value is almost the same with a small shift of $1.5°$ between the two patterns. The side lobes in both cases ($10°$ and $30°$) show differences between the analytical and simulation results. This could be explained by the small size of the considered RA. The simulation setup in HFSS (**Figure 2-25**) shows that the size of the horn compared to the size of the RA is too big and this may lead to some coupling effects.

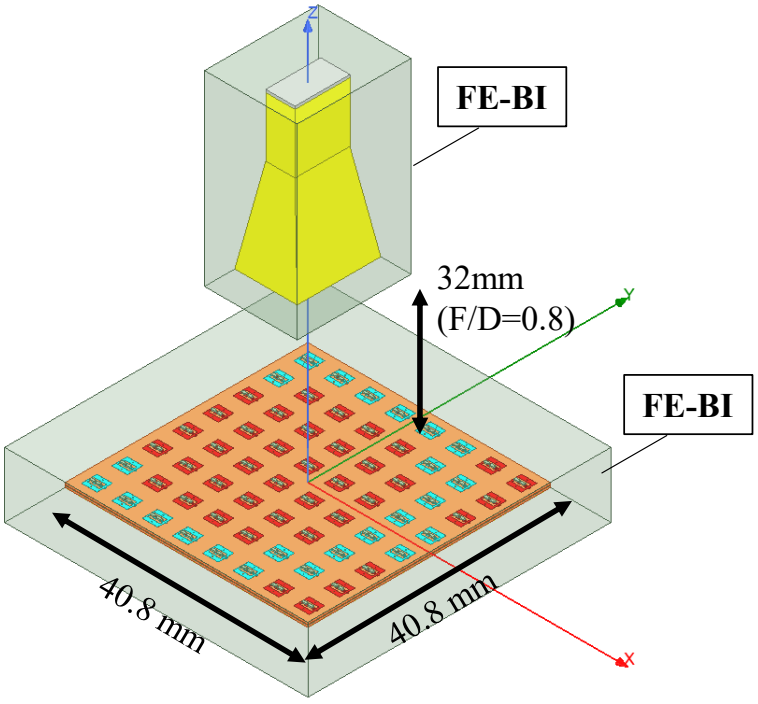

Figure 2-25 The HFSS simulation setup of a RIS of 8x8 unit cells illuminated in the middle by a standard 10dBi horn.

In general, the RIS sizes are much bigger than the one considered in this case. The small size was fixed in order to maintain the balance between the validation of the concept and the time consumption of the full-wave simulation. Finally, these patterns demonstrate the feasibility of reconfigurable RA using the developed UC.

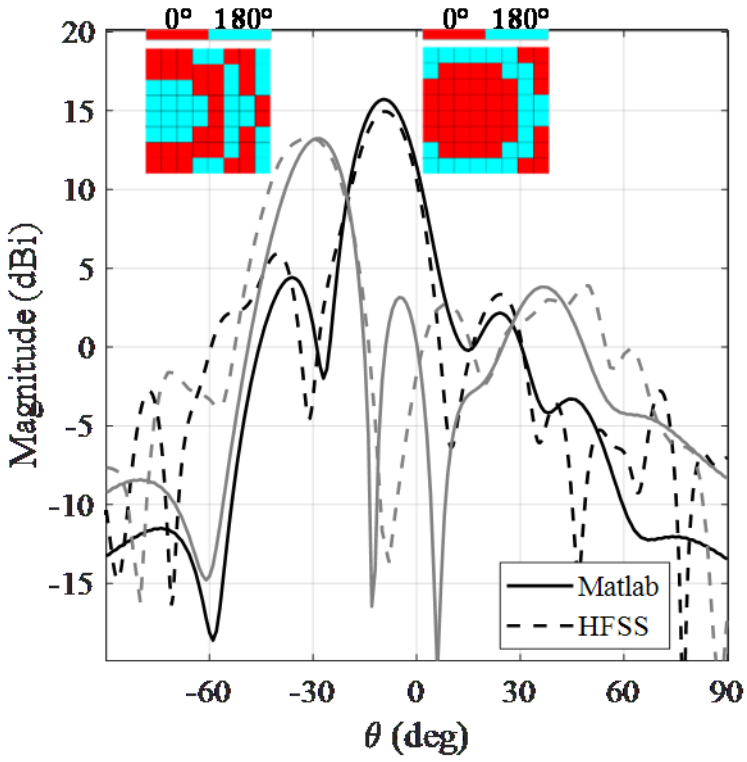

Figure 2-26 The 2D gain pattern of the RA of 8x8 UCs at 29GHz in the plane $\boldsymbol{\phi} = \mathbf{0}°$ for two steering angles $-\mathbf{30}°$ and $-\mathbf{10}°$.

2.3.4 RIS Element Reflection Coefficient – Transfer Function

We consider the wireless communication between a Transmitter (TX) equipped with N_t antenna elements and an N_R -antenna Receiver (RX), which is enabled by RIS having N_{RIS} UCs each with tunable response. The aim of this section is to propose an E2E wideband channel model, between one transmitting and one receiving antenna elements in presence of a RIS and approaching each tunable UC of the RIS such as Linear and Time-Invariant (LTI) system. It holds for the outputs of the involved LTI systems:

$$\boldsymbol{v}_{in}^{r}(\boldsymbol{f}) = \boldsymbol{h}(\boldsymbol{f})\boldsymbol{v}_{in}(\boldsymbol{f}) \quad \text{2-27}$$

$$\boldsymbol{v}_{out}^{r}(\boldsymbol{f}) = \boldsymbol{\gamma}(\boldsymbol{f})\boldsymbol{v}_{in}^{r}(\boldsymbol{f}) \quad \text{2-28}$$

$$\boldsymbol{v}_{out}(\boldsymbol{f}) = \boldsymbol{g}(\boldsymbol{f})\boldsymbol{v}_{out}^{r}(\boldsymbol{f}) \quad \text{2-29}$$

where $h(f), \gamma(f)$ and $g(f)$ represent the frequency responses (DTFT) of the systems that model the first-hop wireless channel, the reflection coefficient of the RIS element, and the second-hop wireless channel, respectively. In **Figure 2-27**, we depict the proposed E2E channel model between one TX and one RX antenna elements via a RIS UC. At this point we want to find the overall E2E response that links the output voltage to the input one, modelling it as the cascade of individual transfer functions. To do this, the first fundamental step is to characterize the response of an individual UC from an EM point of view on the base of its reflection coefficient.

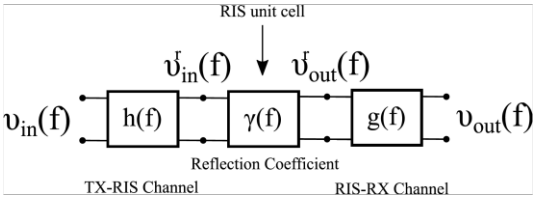

Figure 2-27 Transfer-function-based modeling of the E2E RIS-enabled channel between a TX and RX antenna.

2.3.5 RIS Element Reflection Coefficient – Resonant Model

One can model the RIS such as a reflect-array as shown in **Figure 2-28**, which constitutes a structure that is analytically solvable. In this context, it has been shown [KYE13] that the response of a single RIS element in a periodic surface has an inverse Lorentzian form

$$[\boldsymbol{\Gamma}(\boldsymbol{f})]_{n,n} = \frac{\frac{1}{Q_n^{rad}} - \frac{1}{Q_0} - \frac{2j(f-f_n^r)}{f_n^r}}{\frac{1}{Q_n^{rad}} + \frac{1}{Q_0} + \frac{2j(f-f_n^r)}{f_n^r}} \quad 2\text{-}30$$

Where $\boldsymbol{\Gamma}(\boldsymbol{f})$ is the $N_{RIS} \times N_{RIS}, n = 1,2,\ldots,N_{RIS}$ diagonal matrix with each RIS element response in its' diagonal, f_n^r is the resonance frequency of the UC, which depends critically on radiative Q_n^{rad} and loss Q_0 quality factor. In the presence of a tunable loading of the UC, the quality factors of the complex-valued reflection coefficient are perturbed, as well as the associated resonant frequency of the cell, viz.,

$$[\boldsymbol{\Gamma}(\boldsymbol{f})]_{n,n} = \frac{\frac{1}{Q_n^{rad}+\Delta Q_n^{rad}} - \frac{1}{Q_0+\Delta Q_{0,n}} - \frac{2j(f-f_n^r-\Delta f_n)}{f_n^r+\Delta f_n}}{\frac{1}{Q_n^{rad}+\Delta Q_n^{rad}} + \frac{1}{Q_0+\Delta Q_{0,n}} + \frac{2j(f-f_n^r-\Delta f_n)}{f_n^r+\Delta f_n}} \quad 2\text{-}31$$

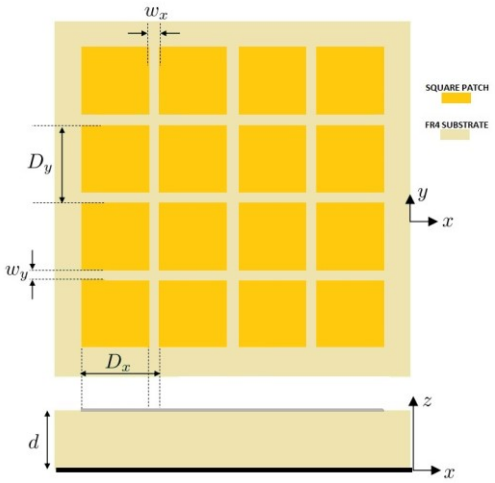

Figure 2-28 Patch-based reflect-array on a grounded substrate: The reflection response configures as an 'inverse-Lorentzian' function.

2.3.6 Full wave simulations

We now adopt and extend the model Eq. 2-30 to fit the magnitude and phase of the reflection coefficient obtained from full-wave simulations. We exploit the CST simulations to extract the quality factor and resonant frequency of the unloaded structure, as well as their perturbation in presence of loading. The fitting of the reflection coefficient, obtained through a PBC simulation (the so-called Floquet analysis) is done through the radiation quality factor Q_n^{rad}, and requires finding the loss quality factor of the reflect-array Q_0, which can be expressed in terms of substrate (Q_C) and metal (Q_d) quality factors such as: $\frac{Q_C\, Q_d}{Q_C + Q_d)}$. To evaluate the performance of the proposed approach, a set of full-wave simulations with SIMULIA CST Microwave Studio have been performed. The main interest of this analysis is to consider active elements, such as varactors, in the design of the reflect-array UC to achieve the reconfigurability of the reflection coefficient. The RIS consists of a periodic surface in which the single UC is a square metal patch loaded with varactor diodes. This meta-surface is placed on a thin dielectric FR4 substrate shielded by a metal ground. As mentioned, the EM simulations of the RIS have been carried out resorting to the Floquet theorem for periodic structures that allow for considering the mutual coupling effect among the UCs. The varactor capacitance values have been selected to obtain a quantization of the reflection coefficient phase, with $45°$ steps, over the entire phase range from $-180°$ to $+180°$ as shown in **Figure 2-29**. It is important to emphasise that all these simulations and comparisons with the Lorentzian model assume a normal incidence on the meta-surface.

In order to obtain a Lorentzian model of the reflection coefficient of the RIS, as expressed in Eq. 2-31, two successive stages have been performed. At first, the reflection phase of the unloaded structure, or without the varactor, is analysed at normal incidence by using CST simulator. From this simulated reflection coefficient, the resonance frequency f_r and the quality factor Q_{rad} can be estimated. f_r is calculated as the frequency where the reflection coefficient equals 0, while Q_{rad} by inverting the equation Eq. 2-30 being Q_0 and f_r now assigned. Q_0 is the parallel combination of dielectric loss Q_d and metallic loss Q_C of the square patch and can be evaluated analytically using the geometrical and electrical parameters of the design. Due to the inversion of the Eq. 2-30, Q_{rad} has a small imaginary part and a small peak at the resonance frequency f_r in its real part. It was therefore chosen to consider only the real part of Q_{rad} and perform a polynomial interpolation to avoid this peak, as shown in **Figure 2-30**. The comparison between the full-wave simulated reflection coefficient and the one obtained with Lorentzian model adopting f_r and Q_{rad} are shown in **Figure 2-31**. A small deviation with respect to the amplitude is present, and concerning the reflection phase the two curves are almost superimposed. At this point, in order to find a Lorentzian expression of the reflection coefficient for a RIS, we can use the parameters previously calculated within Eq. 2-31 by adopting a perturbative approach. These three terms, $\Delta Q_{rad}, \Delta Q_{rad}$ and Δf, are considered as fitting parameters for the model tuning and assumed as unknown but constant with respect to frequency. The CST simulations of the reflection coefficient, as the varactor diode capacitance varies, were compared to the Lorentzian model with the tuning parameters appropriately chosen to achieve this fitting. These results are showcased in **Figure 2-32** in which this comparison is reported for a particular value of the capacitance corresponding to the 3rd quantization level.

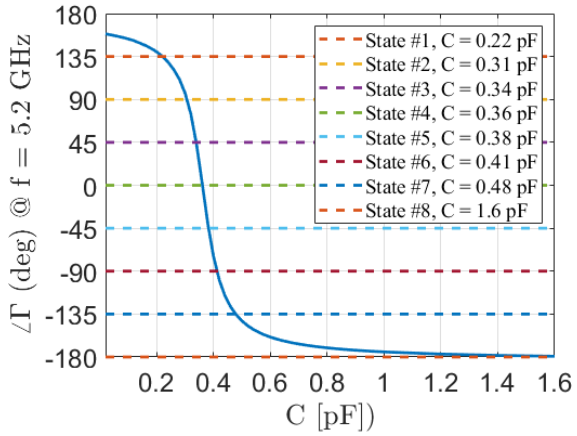

Figure 2-29 Phase of the reflection coefficient for a Varactor loaded RIS against capacitance $@\boldsymbol{f} = \mathbf{5.2}\ \boldsymbol{GHz}$.

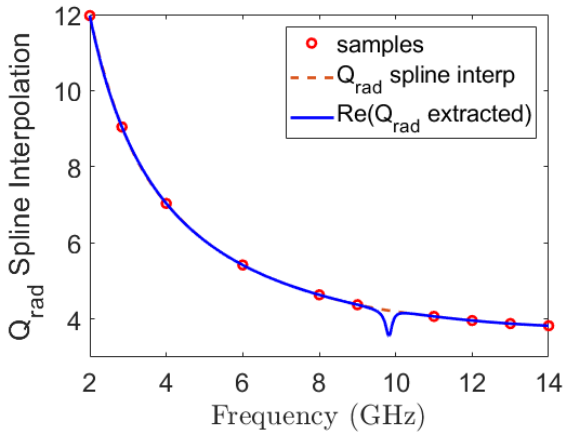

Figure 2-30 Real part of $\boldsymbol{Q_{RAD}}$ is represented with the continuous blue line. The red dashed line represents its interpolation from the samples shown in red circles.

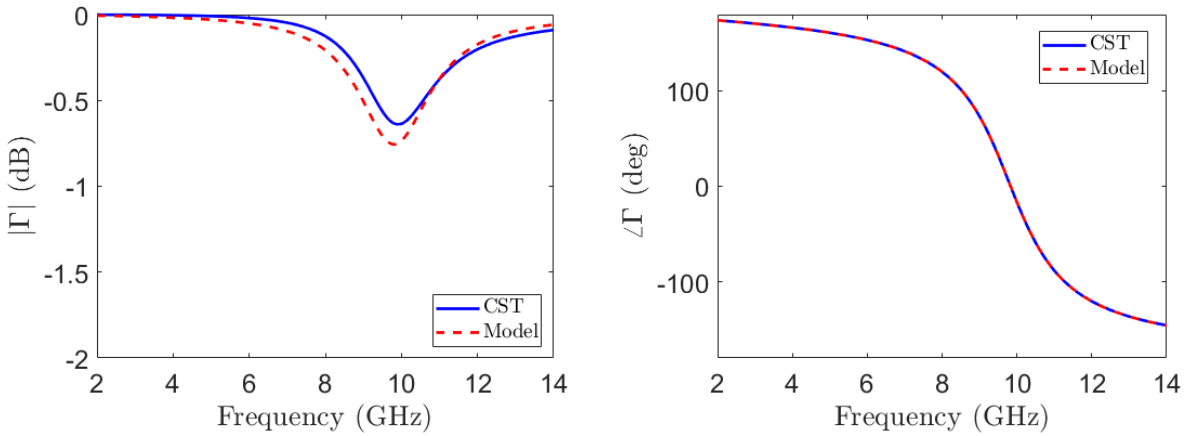

Figure 2-31 Amplitude (on the left) and phase (on the right) of the reflection coefficient at normal incidence for a RIS without Varactors. The results of the Lorentzian model are compared with CST full-wave simulations.

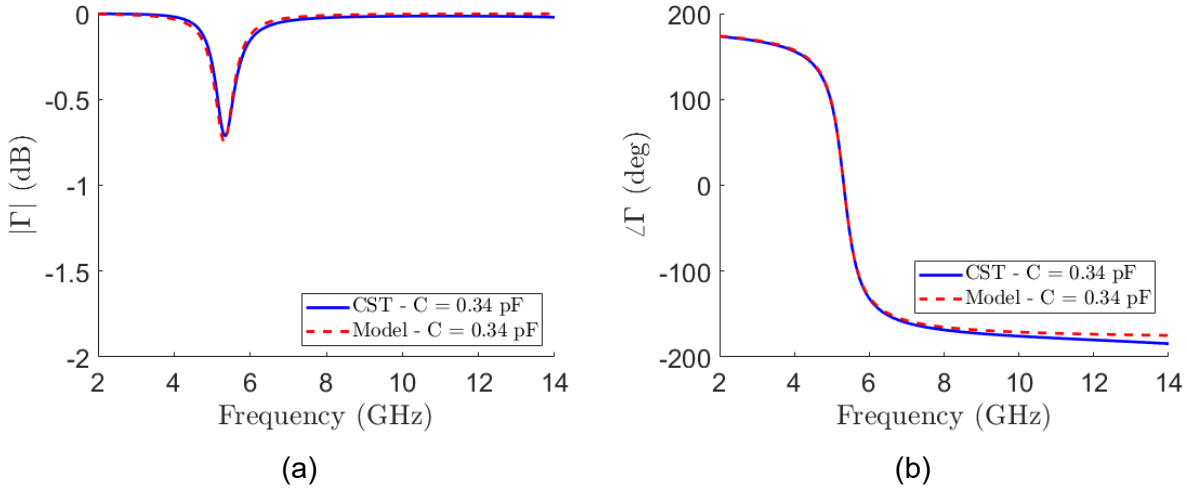

Figure 2-32 Amplitude (a) and phase (b) of the reflection coefficient at normal incidence for a RIS composed by a varactor with $\boldsymbol{C = 0.34pF}$. The results of the Lorentzian model are compared with CST full-wave simulations.

3 RIS channel modelling and sounding

3.1 RIS modelling under rich multipath fading

3.1.1 Random coupling model for impedance matrices

Progress has been achieved in i) The optimization of the RIS phase mask operating in presence of back-reflections from the propagation environment; ii) The inclusion of LOS channels and the understanding of their role in achieving CH; iii) The computation of mutual information statistics.

In D3.1 we have shown how to integrate multipath fading in the impedance-matrix based on wave chaos assumptions that lead to a physics-based statistical model, the RCM is used in both the uplink $\mathcal{Z}_{ST}$ and downlink $\mathcal{Z}_{RS}$ impedance matrices depicted in **Figure 3-1**.

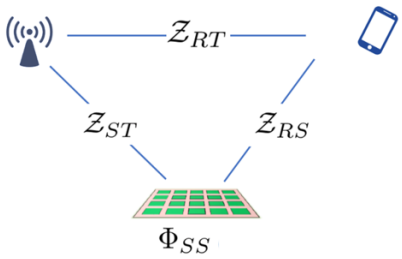

Figure 3-1 RIS assisted wireless link operating in free space: All the LOS channels between transmitter and receiver, and transmitter/receiver and RIS, are assumed to support multipath fading where both LOS and NLOS channels coexist and have prescribed statistics.

Let us remember that in the moderate loss regime, i.e., $\alpha > 1$, we assume that the active impedance of the RIS is not changed by back-reflected waves in the propagation environment, viz.,

$$\boldsymbol{Z_{ST}^{\mathrm{cav}} = \mathrm{Re}\left[Z_{SS}^{\mathrm{fs}}\right]^{1/2} \cdot \xi(\alpha) \cdot \mathrm{Re}\left[Z_{TT}^{\mathrm{fs}}\right]^{1/2}} \quad 3\text{-}1$$

for the mutual impedance between transmit array (TA) and RIS elements,

$$\boldsymbol{Z_{RS}^{\mathrm{cav}} = \mathrm{Re}\left[Z_{RR}^{\mathrm{fs}}\right]^{1/2} \cdot \xi(\alpha) \cdot \mathrm{Re}\left[Z_{SS}^{\mathrm{fs}}\right]^{1/2}} \quad 3\text{-}2$$

for the mutual impedance between RIS elements and receive array, and

$$\boldsymbol{\Phi_{SS}^{\mathrm{cav}} \approx \left(Z_{SS}^{\mathrm{fs}} + Z_{RIS}\right)^{-1}} \quad 3\text{-}3$$

for the RIS state matrix. In Eq. 3-1 and 3-2, a universal fluctuation matrix that configures as a random matrix from the GOE parameterized by the average modal overlap α, whose entries are expressed by a sum of ergodic eigenmodes supported by the propagation environment, hence

$$\boldsymbol{\xi_{ps}(\alpha) = -\frac{j}{\pi} \sum_{m=1}^{M} \frac{w_{pm} w_{sm}}{\frac{k_0^2 - k_m^2}{\langle \Delta k_m^2 \rangle} - j\alpha}} \quad 3\text{-}4$$

where the resonance eigen-spectrum k_m^2 has average mean spacing $\langle \Delta k_m^2 \rangle$ and associated random eigenfunction that is zero-mean Gaussian distributed. We have further developed this formalism to include the LOS channels in **Figure 3-1**. Neglecting the LOS between TA and receive array, where blockage is assumed in those use cases that benefit RIS technologies, yields

$$\boldsymbol{Z_{ST} = Z_{ST}^{\mathrm{fs}} + Z_{ST}^{\mathrm{cav}}} \quad 3\text{-}5$$

where the statistical fluctuation in the uplink is entirely captured by Z_{ST}^{cav}, and

$$\boldsymbol{Z_{RS} = Z_{RS}^{\mathrm{fs}} + Z_{RS}^{\mathrm{cav}}} \quad 3\text{-}6$$

where the statistical fluctuation in the downlink is entirely captured by Z_{RS}^{cav}. Upon normalization, we can write the random signal model for RIS assisted MIMO systems as [ADD21]

$$\boldsymbol{y = h_{RS}\, \Phi_{SS}\, h_{ST}\, x} \quad 3\text{-}7$$

where the normalized complex-valued channel gain matrices are defined as $h_{RS} = Y_{RR} Z_{RIS} Z_{RS} Y_0$, $\Phi_{SS} = Z_0 \Phi_{SS}^{\mathrm{cav}}$, $h_{ST} = Z_{ST} Y_{TT}$, with $Y_{RR} = \left(Z_{RR}^{\mathrm{fs}} + Z_{RIS}\right)^{-1}$, $Y_{TT} = \left(Z_{TT}^{\mathrm{fs}} + Z_G\right)^{-1}$, $Z_0 = (Y_0)^{-1}$ active impedance of TA and receive array, and (diagonal) free-space impedance matrix with entry η, respectively. For a SISO RIS-assisted wireless link, the optimization of the phase of the tuning impedance reads, in absence of mutual coupling between UCs of the RIS [QR21]

$$\boldsymbol{\Phi_{kk} = \eta \frac{1 + e^{-2j\theta_n}}{2|r_0 + x_{SS}|}} \quad 3\text{-}8$$

is obtained as an implicit equation

$$\boldsymbol{\theta_n = f(\mu_{ST}, \sigma_{ST}, \mu_{RS}, \sigma_{RS}; \theta_{m \neq n}) \qquad n = 1, \ldots, N} \quad 3\text{-}9$$

that can be computed numerically via Monte Carlo simulations. It is worth noting that (3-9) has the meaning of a fading aware RIS optimization through average and standard deviation vectors of the fading in both the uplink and downlink paths. The average SNR_h is depicted in Figure 3-2

for the increasing number of active UCs N within the RIS. Higher-order moments of SNR_h have been calculated analytically with the MGF method. The computation of the variance gives access to CH bounds. We show the numerical results obtained from Monte Carlo computation in **Figure 3-2**, in order to corroborate the theoretical models.

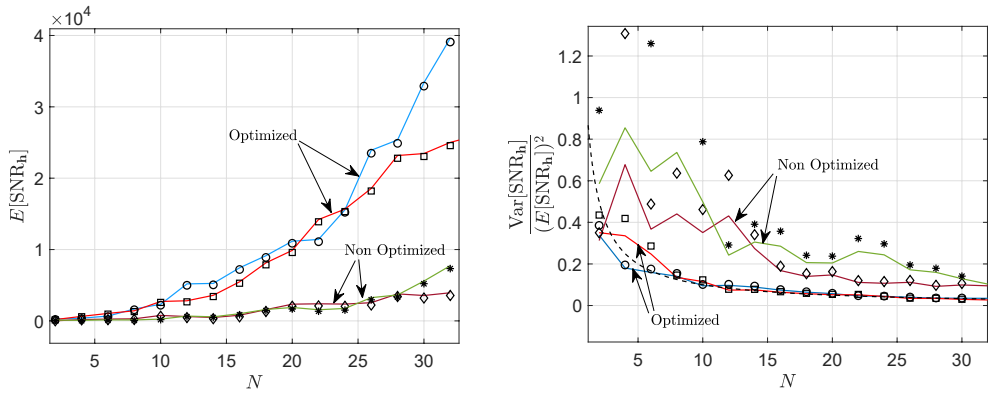

(a) (b)

Figure 3-2 Theoretical predictions (solid lines) of expectation (a) and CH (b) are reported and validated by Monte Carlo simulations (symbols) for both the optimal and non-optical scenarios. Colored lines represent two (uniform) LOS channels of different strength.

Figure 3-2 clearly shows an improvement of the wireless link performance through the RIS, in terms of reduction of the path loss, with the onset of CH. The optimal case is fitted by $1/N^2$ as expected in the asymptotic regime. However, it is found that this result critically depends on the existence of LOS channels. Also, the non-optimal case shows a (slower but significant) channel hardening effect, which remarks the benefit of adopting the RIS, even of relatively small dimension, in harsh environments. The emergence of CH in RIS-assisted wireless digital links has been demonstrated via a SDR-based transceiver operated in reverberation chamber (a controlled laboratory environment to emulate multipath fading) [GLL+21] and in a real-life open space to test cross-interference suppression in multi-user use cases.

Furthermore, using the MGF method one can obtain the statistics of the MI for a RIS-assisted SISO link, which fluctuates on account of the statistical behavior of SNR_h. Starting from the MI definition $\chi = \log_2(1 + \mathrm{SNR_h})$, we first derive the probability PDF of the $\mathrm{SNR_h}$, i.e., $P(\mathrm{SNR_h})$, then calculate the Laplace transform of the obtained PDF and use the Hubbard-Stratonovich transform to obtain the MGF of $\mathrm{SNR_h}$

$$\boldsymbol{E}\left[e^{-s(\mathbf{SNR_h})}\right] \propto \int \boldsymbol{dt_1} \int \boldsymbol{dt_2} \frac{e^{-\frac{1}{4s}\left(t_1^2+t_1^2\right)}}{s} \boldsymbol{E}\left[e^{-jt_1\mathbf{Re}[y]-jt_2\mathbf{Im}[y]}\right] \qquad 3\text{-}10$$

which finally yields, upon a logarithmic variate transform, the PDF of χ, i.e., $P(\chi)$. The numerical results, obtained from Monte Carlo simulations and reported in **Figure 3-3**, confirm the validity of predictions.

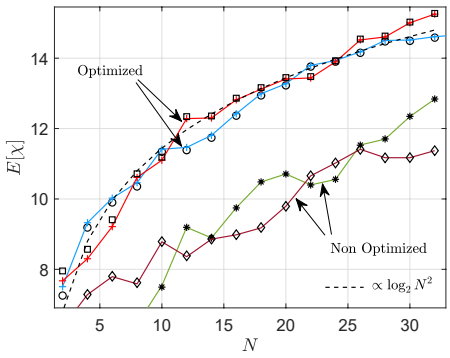

Figure 3-3 Expectation of the mutual information in RIS-assisted links with different (uniform) LOS channels and for both the optimal and non-optimal operation of the N-element RIS.

The mutual information statistics obtained through RCM show a performance increase from the RIS, thanks to the fading-aware optimization discussed in Eq. 3-9. The results obtained in this activity inform the performance analysis and enhancement in WP4. The impedance matrix model has been adopted in the edge-computing optimization methodology proposed in WP4, to provide a system-level simulator. Furthermore, the integration of the RCM in the impedance matrix model augments the geometric model in Section 4.1 to provide an integrated channel model in presence of obstacles and channel variability.

3.1.2 Random plane-wave superposition in FDTD

In WP3 we started to model the RIS by implementing the GSTCs in the FDTD scheme. The RIS is considered as homogeneous and continuous sheet, with a very small thickness compared to the wavelength, and allows us to simulate RISs in an easy manner by appropriately modifying the susceptibility function that characterize the RIS functionalities. The insertion of RIS via the GSTCs causes an update of the classic FDTD scheme based on the Yee's grid, introduced in D3.1, D6.2 and explained in detail in [VCA18], [VAC16] and [JYL20].

Full wave simulations allow us to study the EM response of RIS when operates at different states, such as reflective RIS, transmissive RIS, Reflectarray and Transmittarray structure. The RIS is illuminated by a single wave or waves, appropriately created. The single wave or a superposition of a finite number of plane waves are created by generating the angle of incidence, the distance *d* and the polarization as independent quantities. **Figure 3-4** shows the geometry for the generation of a random plane wave which illuminates the device under test, in our case the dotted box represents the RIS. In the plane wave generation, angles θ, α and ϑ are generated independently each other. Those values can be tuned if ones would reduce the angle of arrival of impinging waves. The versor $\hat{n}$ denotes the incidence and can come from any direction whereas E and H are the electric and magnetic field respectively.

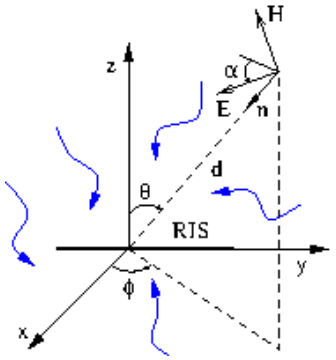

Figure 3-4 Geometry for the generation of an incident plane wave over the simulation domain.

The proposed setup in **Figure 3-4**, by considering a superposition of plane waves, allows us to reduce the overall computational burden with respect to simulate the whole environment such as the reverberation chamber (RC), including RISs. In fact, the EM environment attained within the RC can be reproduced and modelled as the superposition of a finite number of plane waves [DAH98], [MAP06].

Beside the model previously described in D3.1, based on the GSTCs, RIS can be also modelled as a periodic surface over a ground plane [FCB21], see **Figure 3-5**.

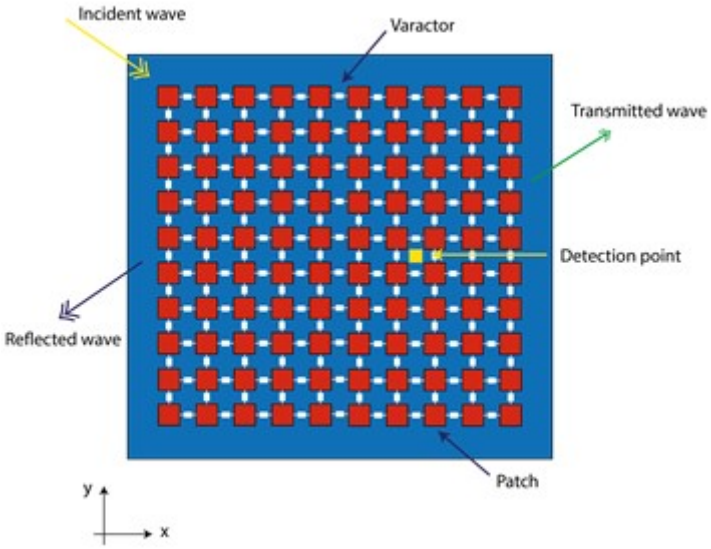

Figure 3-5 RIS simulated by diodes/capacitors.

In this case, the RIS is modelled by perfect electric conductor (PEC) squares patches along *x* and *y* directions. Varactors diodes are lumped elements that connect adjacent cells in both *x* and *y* directions. Dimensions of the simulated patch(s) are 10×10 mm, equispaced by 1 mm each other, the permittivity of dielectric support has value of $\varepsilon_r = 4.4$ and the conductivity is $\sigma = 0.0025\, S/m$. In the simulated case, RIS has 180 varactors, with values of capacitance $C = 0.1\, pF$ and/or 1 pF. RIS has 25 varactor diodes, with values of 0.1 pF and/or 1 pF. The RIS dimension should be considered large enough to guarantee an acceptable focusing on the target because the received power depends on the reflecting surface. Currently, the investigated band is from 1 to 8 GHz and the amplitude of the incident wave is 1 V/m. The small yellow square in Figure 3-5 highlights the detection point where the received signal were saved. The capacitor within the FDTD scheme is modelled by the equation [TAF95]:

$$E_z|_{i,j,k}^{n+1} = E_z|_{i,j,k}^{n} + \left(\frac{\frac{\Delta t}{\epsilon_0}}{1+\frac{C\Delta z}{\epsilon_0 \Delta x \Delta y}}\right) \nabla \times H_{i,j,k}^{n+1/2} \quad 3\text{-}11$$

Preliminary results of this geometry are following reported.

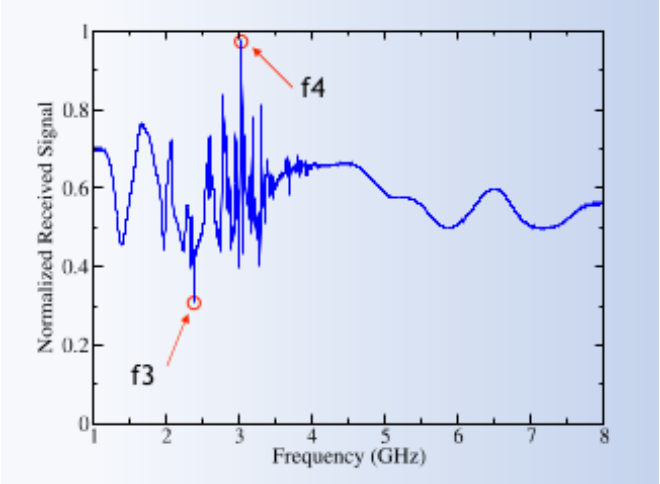

Figure 3-6 Normalized received signal at the detection point.

Figure 3-6 reports the normalized received signal where the points registered at f3 and f4 are pointed out. Figure 3-7 and Figure 3-8 show the distribution of the magnitude of the electric field on the RIS, referred to f3 and f4 respectively.

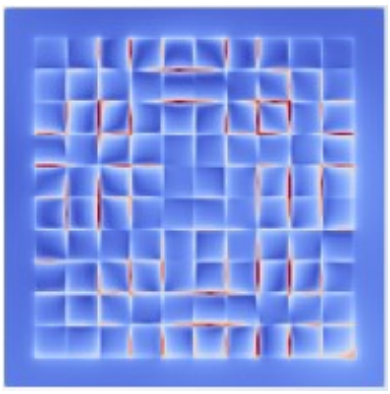

Figure 3-7 Electric field distribution at f3.

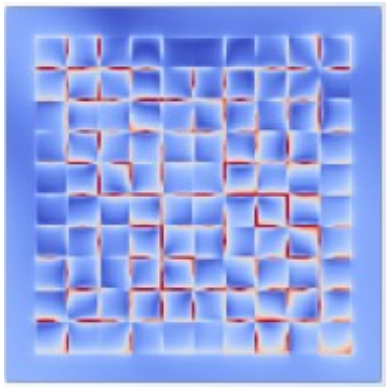

Figure 3-8 Electric field distribution at f4.

In particular, we can note that the maximum values of the electric field are distributed around the centre of the RIS at f3 as reported in Figure 3-7, whereas at f4 the electric field is irregularly distributed as shown in Figure 3-8. The variability of the field in space and frequency is due to the influence of varactors on the wave propagation. An optimization of varactors configuration will allow to get the desirable operation condition of the RIS.

3.2 RIS link with random (and moving) scatterers

3.2.1 Impedance-based model extension for scattering clusters

In this section, we generalize the RIS channel model proposed in [GD21] to the case of multiple scattering cluster objects present in the environment. In particular, as depicted in Figure 3-9, we consider a multi-user MIMO network with M-antennas at the transmitter and L single-antenna receivers.

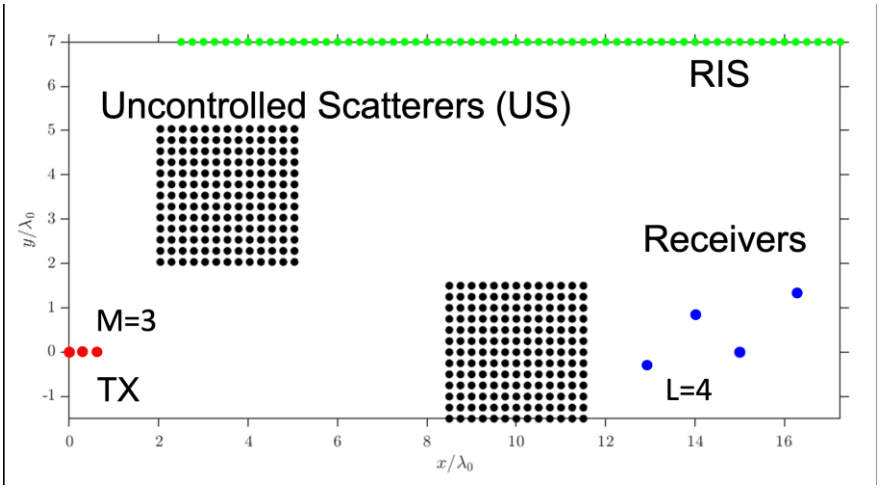

Figure 3-9 RIS-aided multi-user MIMO network in the presence of (uncontrolled) scattering clusters.

We mode the RIS elements as tunable impedances, whereas the uncontrolled scatterers are modelled as fictious dipoles, attached to fixed and fictious loads. The channel matrix is thus given by

$$\mathbf{H}_{E2E} = \left(\mathbf{I} + \mathbf{Z}_{RR}\mathbf{Z}_L^{-1}\right)^{-1}[\mathbf{Z}_{RT} - \mathbf{Z}_{RE}(\mathbf{Z}_{EE} + \mathbf{Z}_{SC})^{-1}\mathbf{Z}_{ET}](\mathbf{Z}_{TT} + \mathbf{Z}_G)^{-1} \in \mathbb{C}^{L\times M} \quad 3\text{-}12$$

where Z_{RR}, $\mathrm{Z}_{L}, \mathrm{Z}_{TT}, \mathrm{Z}_{G}$ are assumed to be known and are related to the internal impedances of the transmitter generator and receiver load. Whereas Z_{RT} represents the direct channel from the transmitter to the receivers, $\mathrm{Z}_{RE}, \mathrm{Z}_{ET}$ are the channel from the propagation environment, i.e., both the uncontrolled scatterers and the RIS to the receiver, and from the transmitter to the propagation environment. Z_{EE} is the self and mutual impedance of the propagation environment and Z_{SC} represents the (tunable) impedance of both the RIS elements and the uncontrolled scatters. We model the latter two matrices as

$$\mathbf{Z}_{EE} = \begin{bmatrix} \mathbf{Z}_{OO} & \mathbf{Z}_{OS} \\ \mathbf{Z}_{SO} & \mathbf{Z}_{SS} \end{bmatrix} \quad \text{3-13}$$

$$\mathbf{Z}_{SC} = \begin{bmatrix} \mathbf{Z}_{US} & \mathbf{0} \\ \mathbf{0} & \mathbf{Z}_{RIS} \end{bmatrix} \quad \text{3-14}$$

where *O* stands for the uncontrollable objects, while *S* stands for the RIS UCs. In this regard, the matrix Z_{SS} models the mutual coupling across the array, whereas Z_{US} describes the (fixed) reflection parameters of the uncontrollable objects, and lastly Z_{RIS} denotes the tunable RIS impedances (to be optimized).

Hence, the receive signal at user *l* is given by

$$\boldsymbol{y}_{\boldsymbol{l}} = \mathbf{h}_{\boldsymbol{E2E,d,l}}\mathbf{W}\mathbf{s} + \mathbf{h}_{\boldsymbol{E2E,l}}(\mathbf{Z}_{\boldsymbol{RIS}})\mathbf{W}\mathbf{s} + \mathbf{n}_{\boldsymbol{l}} \quad \text{3-15}$$

where $\mathrm{h}_{E2E,d,l}$ is the *l*-th row of the matrix $(\mathrm{I} + \mathrm{Z}_{RR}\mathrm{Z}_{L}^{-1})^{-1}\mathrm{Z}_{RT}(\mathrm{Z}_{TT} + \mathrm{Z}_{G})^{-1}$ containing the direct link from the transmitter to the receiver, $\mathrm{W} \in \mathbb{C}^{M \times L}$ is the BS precoder, $\mathrm{s} \in \mathbb{C}^{L \times 1}$ is the transmit signal vector, $\mathrm{h}_{E2E,l}(\mathrm{Z}_{RIS})$ is the *l*-th row of the matrix $-(\mathrm{I} + \mathrm{Z}_{RR}\mathrm{Z}_{L}^{-1})^{-1}\mathrm{Z}_{RE}(\mathrm{Z}_{EE} + \mathrm{Z}_{SC})^{-1}\mathrm{Z}_{ET}(\mathrm{Z}_{TT} + \mathrm{Z}_{G})^{-1}$ describing the channel matrix from the transmitter to the receiver, which is reflected upon the RIS, and n_{l} is the AWGN coefficient.

Our objective in this context is to find both the optimized BS and RIS configurations, i.e., Z_{RIS} and W, as a function of the uncontrollable scattering objects in the environment.

3.2.2 Field-based model extension for scattering clusters

This section presents the end-to-end frequency-selective channel model for RIS-parametrized wireless environments with adjustable fading, based on the coupled-dipole formalism, referred to as PhysFad [FSA22], while its' source code is being shared online in [P22]. PhysFad describes each of the three entities of the wireless channels, namely: *i*) the transmit and receive antennas; *ii*) the scattering environment, and *iii*) the RIS elements of responses, as a dipole or a collection of dipoles with specific properties.

The model utilizes 2D dipoles in the x-y axis, with their dipole moments oriented in the vertical z axis. By modelling the transceivers via the 2D coupled-dipole formalism, PhysFad has the ability to adopt non-scattering transceivers, in addition to the scattering ones. Their central operating frequency and bandwidth can be adjusted by the dipole parameters. Regarding the wireless environment, scattering objects are modelled as dense fences of dipoles, the fence density and losses of which control the amount of their absorption and reflection. Each RIS element is modelled as a dipole, being able to control its resonant frequency. The RIS design is being characterized by evaluating the RIS reflection coefficient for various RIS configurations, under normal incident. These components are combined into a channel model in terms of the end-to-end channel matrix, in which the fading can be adjusted.

For PhysFad, fading can be adjusted by tweaking the transparency of the environment via the resonance frequency of its' constitutive dipoles. If the resonant frequency is orders of magnitude

above the operating frequency, the environment essentially does not scatter the waves and is effectively transparent, such that we are effectively dealing with free space where only the LoS component exists. By sweeping across the different values of the resonant frequency, the K-factor of the Rician environment can be adjusted via only one parameter.

A demonstration of the derivation of the end-to-end channel matrix is as follows. Considering a general MIMO scenario involving N_T transmitters and N_R receivers, N_E dipoles that constitute the scattering environment, and N_{RIS} dipoles that constitute the RIS, the total number of dipoles in the system is $N \triangleq N_T + N_R + N_E + N_{RIS}$. Following the coupled-dipole formalism, the following can be derived:

$$\boldsymbol{W(f)p(f) = E_{ext}(f)} \quad \text{3-16}$$

where the $N \times N$ complex-valued matrix $W(f)$ contains the inverse polarizabilities $\alpha_i^{-1}, i = 1,2,\dots,N$ of the N dipoles in its diagonal and each (i,j)-th off-diagonal entry is $-G_{ij}(f)$, the negative of the 2D free-space Green's function between the locations of the i -th and j-th dipoles, $j = 1,2,\dots,N$. Vector $p(f)$ contains the dipole moments of the N dipoles at frequency f and $E_{ext}(f)$ comprises the corresponding external electric fields. The wave equation's linearity allows performing calculations independently at each desired frequency, and henceforth, the frequency dependence can be dropped. The goal is to compute p whose entries for the receiving dipoles must be multiplied by the corresponding inverse polarizabilities to obtain the received fields. Using standard matrix-inversion techniques, p can be evaluated by inverting W, yielding:

$$\boldsymbol{p = W^{-1}E_{ext}} \quad \text{3-17}$$

Next, a diagonal matrix containing the inverse polarizabilities is being multiplied on both sides of Eq. 3-17, resulting in the following expression:

$$\boldsymbol{diag([\alpha_1^{-1}\ \alpha_2^{-1}\dots\alpha_N^{-1}])p = VE_{ext}} \quad \text{3-18}$$

where $V = diag([\alpha_1^{-1}\alpha_2^{-1}\dots\alpha_N^{-1}])W^{-1}$. The end-to-end channel matrix is now simply the $N_R \times N_T$ portion of the $N \times N$ matrix V that links the N_T transmitting dipoles to the N_R receiving dipoles. Without loss of generality, it can be assumed that the dipole indices are in the following order: transmitters, receivers, scattering environment, and RIS. Then:

$$\boldsymbol{H = V[(N_T + 1):(N_T + N_R), 1:N_T]} \quad \text{3-19}$$

An illustrated description of the derivation of the channel matrix is found in Figure 3-10, where the 2×2 MIMO case is being depicted.

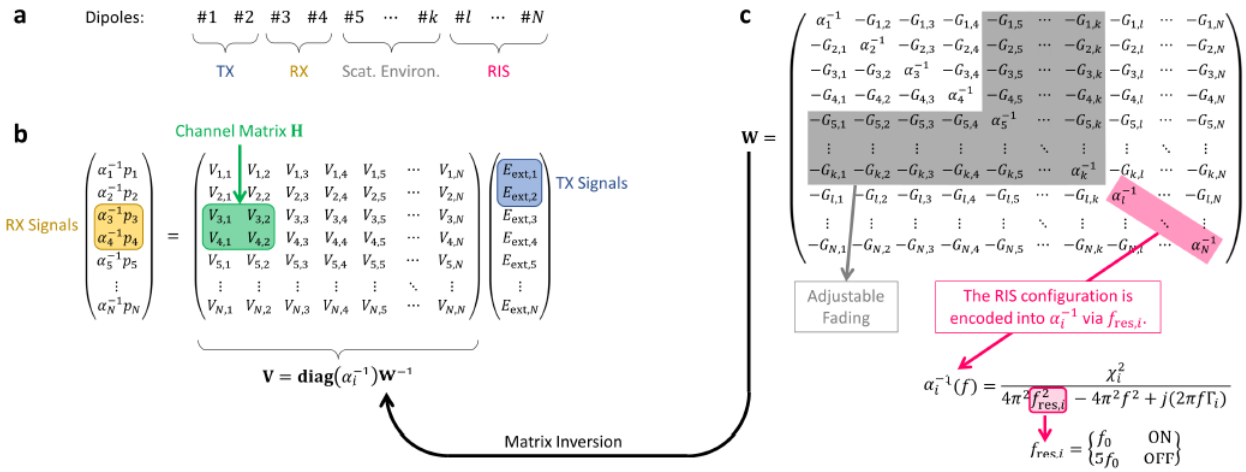

Figure 3-10 Illustration of the link between the coupled-dipole formalism and the RIS-parametrized end-to-end channel matrix for a $\mathbf{2} \times \mathbf{2}$ MIMO example [FSA22].

A case study on RIS-enabled over-the-air channel equalization has been conducted in order to unveil PhysFad's ability to capture the time-domain aspects of RIS-parametrized fading environments. Two different regimes were studied: i) imposing one dominant NLOS channel tap inside an irregularly shaped scattering enclosure with large amount of reverberation, ii) reduced amount of reverberation by adding loss to the dipoles constituting the scattering environment and explore the alternative strategy of cancelling all NLOS taps through destructive interference with lower amount of reverberation. Future directions include the extension to a dyadic 3D version, with detailed models of specific antennas and RISs, as well as serving as a valuable tool in backscatter communications, mesoscopic wave physics and wave scattering.

3.3 Deterministic RIS-assisted channel modelling

3.3.1 RIS model inclusion in ray tracing methods

The simulation of a RIS was started by using *TIMplan3D*, developed in-house based on the "Intelligent Ray Tracer" approach [LU20], [AFR10], [ACN10], [LBD10] to check opportunities and drawbacks of the RIS technology for radio planning purposes.

The ray tracer can simulate a full 3D scenario accounting for electromagnetic propagation and interactions with objects even considering inhomogeneities (see **Figure 3-11**). Each object is described with its real geometrical shape and to each part constituting the object can be assigned the electromagnetic properties of the material it is made of, as a function of the frequency. Ground and orography can be simulated too.

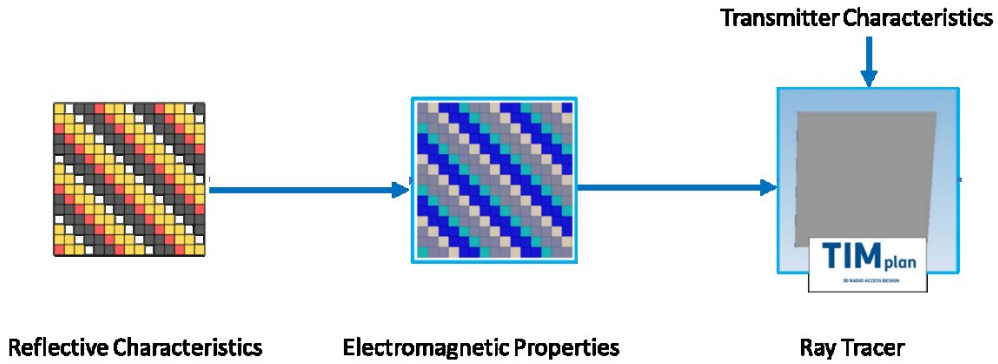

Figure 3-11 Steps to import a RIS in a ray tracer

The main problems to be approached and solved for representing a RIS in the ray tracer are:

1. the representation of the reflective characteristics of the RIS in terms of electromagnetic properties (permittivity, permeability) to be assigned to the RIS model;
2. how to consider the different scales of definition used to represent each element involved: the field in the scenario (typically few meters), the RIS (typically few cm) and the size of each element of the RIS (typically few mm);
3. how to consider the change over time of the reflective characteristics of the RIS.

We have started approaching the first point by analyzing the representation of a dummy RIS inside the ray tracer. For this first example the RIS doesn't have a realistic size, it is represented as a metallic sheet; each inter-element spacing is $\lambda/2$ with respect to the operating frequency. A transmitter, represented with its own antenna radiation pattern and configured transmitted power, was placed in front of the dummy RIS, at 7.5 m and 9.5 m height, at different distances (see **Figure 3-12**).

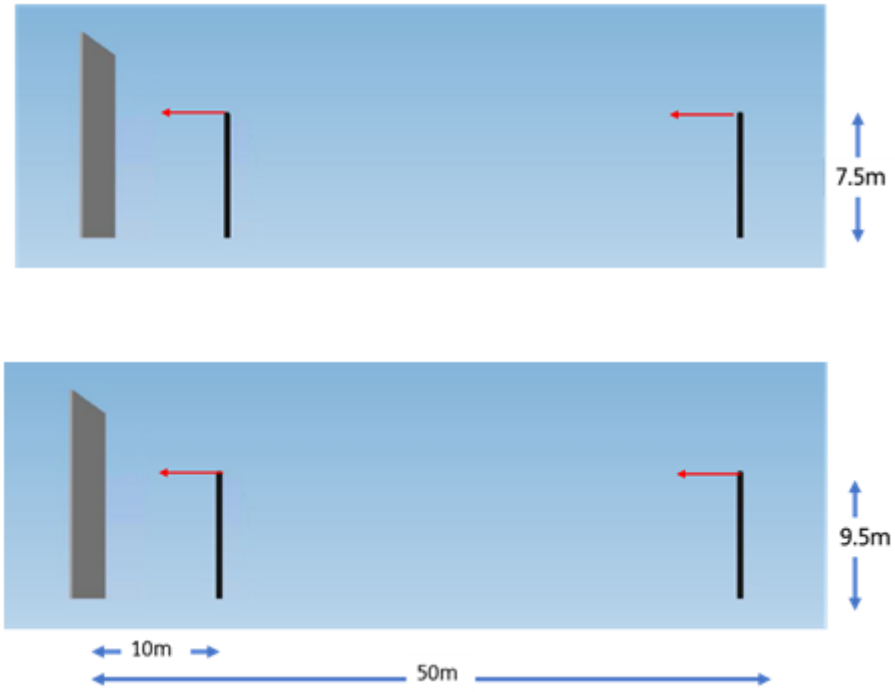

Figure 3-12 Geometries of the simulated scenario

Activities are proceeding in order to compute the field distribution reflected back by the dummy RIS on a set of calculation points arranged on a great circumference of a sphere, at different distance from the RIS (see **Figure 3-13**).

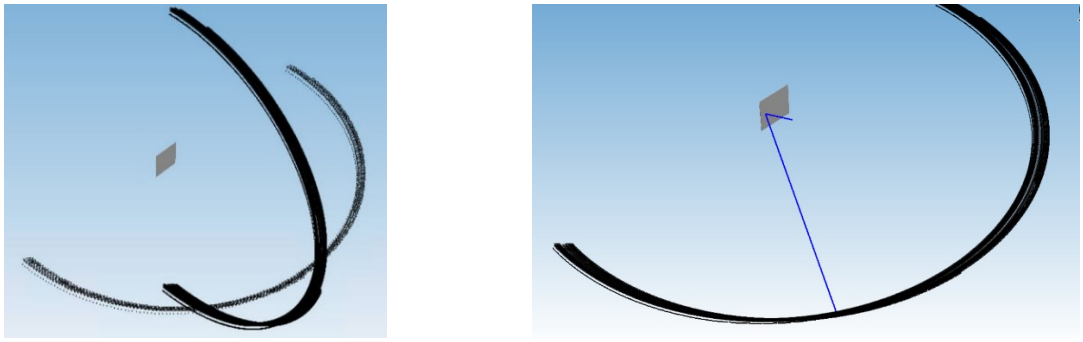

a) b)

Figure 3-13 a) Check points for field evaluation and b) A ray starting from the source to the evaluation point

Further work on RT simulation of RIS-assisted propagation environments has been carried out in [AES+22] for a scenario of interest in future field trials.

3.3.2 RIS model inclusion in Dynamical Energy Analysis

The physical optics model, derived for both the TE and the TM polarizations of the EM field scattered by the RIS, constitutes the starting point for the integration of the RIS response in RT algorithms. In RISE-6G, we will use the DEA method: an RT scheme based on energy flow equations that are computed on discrete meshes. Differently from conventional shoot and bounce RT methods, DEA is based on phase-space (joint spatial angular domain) representation of waves, and it propagates densities of rays through the numerical space by iterative application of a compact operator derived from the boundary integral equation of the confined space. It has been shown already in vibroacoustic that DEA is able to compute the energy flow in refined finite element methods (FEM) meshes [HGG16], also mitigating numerical dispersion via directional basis functions [CCR21]. Furthermore, the ability of DEA of capturing statistical inhomogeneity and anisotropy within complex multi-connected environments with high losses has been showed recently via comparison with power balance methods [FBP21].

In RISE-6G we have undertaken two lines of research to achieve a flexible and efficient coverage planning tool for multi RIS mobile networks beyond 5G:

1. Representation of the RIS scattered field in phase-space. This starts from the calculation of the Wigner function and produces the ray based, classical scattering function by frequency averaging. Upon incidence of a partially coherent field impinging onto the RIS, the spatial field-field correlation of the scattered field can be readily derived from the physical optics model of Sec. 3.3 of D3.1.
2. Generation of numerical meshes from CAD models. In order to enable the DEA compliant numerical domain construction of the two field trials offered by the Partners CRF and

SNCF, it is necessary to convert the CAD models typically used to model 3D environments, like Autodesk AutoCAD (.dwg files) and Autodesk Revit (.rvt files), into appropriate numerical 3D meshes based on tetrahedral elements. A diagram summarising the conversion procedure for generating DEA compliant meshes starting from AutoCAD and Revit CAD models is shown in Figure 3-14.

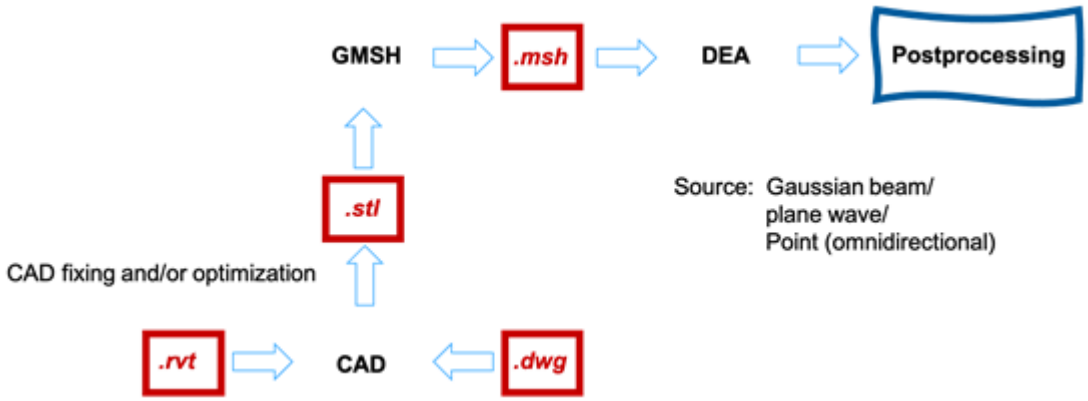

Figure 3-14 Procedure to generate DEA-compliant meshes from CAD models

The first step is then to generate an .stl file from models in Autocad or Revit format. This procedure can be performed directly by exporting the source files in.stl format from these CAD tools. An optimisation step may be necessary, for example to export only a portion of the model of interest, such as a single room within a large building. This output .stl file describes only the surface geometry of the three-dimensional objects without any representation of colour, texture or other common CAD model attributes.

The DEA ranks among RT and power balance methods. It is able to preserve the details of the environment typically obtained through RT, and at the same time aims relaxing the PWB assumptions. DEA can be viewed as a reformulation of RT in a joint space of direction of ray travel and position, referred to as phase-space, by recurring to the so-called Wigner function transformation. DEA manages bundle of rays instead of individual rays or in other words propagate these ray densities over the meshed environment.

Let us therefore briefly review the main steps of this approach in the following. As a preliminary step, we need to obtain a representation of wave fields in phase-space in terms of the Wigner function. Let us define the WDF of a scalar field $\Psi(x)$ as:

$$\boldsymbol{W(x,p) = \int \Psi\left(x+\frac{u}{2}\right)\Psi^{*}\left(x-\frac{u}{2}\right) exp(-ikpu)\, du} \qquad 3\text{-}20$$

where the variable x describes the position and p the local momentum.

in the same way, one can define the WDF for a scalar function in momentum terms $\hat{\Psi}(p)$ as:

$$\boldsymbol{W(x,p) = \left(\frac{k}{2\pi}\right)^{d} \int \hat{\Psi}\left(p+\frac{q}{2}\right)\hat{\Psi}^{*}\left(p-\frac{q}{2}\right) exp(-ikqx)\, dq} \qquad 3\text{-}21$$

with d representing the dimension of the problem space, e.g., if $d = 1$, $\hat{\Psi}(p)$ is given by:

$$\boldsymbol{\hat{\Psi}(p) = \int \Psi(x)\, exp(-ikpx)\, dx} \qquad 3\text{-}22$$

If we would now consider a generic EM source, such as the fields radiated by a large PCB a deterministic approach would be excessively cumbersome to adopt. Instead, by following a statistical approach, one can propagate statistically correlated wave field described by the field-field ACFs, and at the same time leverage the WDF techniques. Let us define the two-point field-field correlation function as an ensemble average over different wave fields:

$$\mathbf{\Gamma}(\mathbf{x_1}, \mathbf{x_2}) = < \mathbf{\Psi}(\mathbf{x_1})\mathbf{\Psi}^*(\mathbf{x_2}) > \quad 3\text{-}23$$

To describe such wave fields in phase-space, one has:

$$\mathbf{W}(\mathbf{x}, \mathbf{p}) = \int \mathbf{\Gamma}\left(\mathbf{x} + \frac{\mathbf{u}}{2}, \mathbf{x} - \frac{\mathbf{u}}{2}\right) \mathbf{exp}(-\mathbf{ikpu})\, \mathbf{du} \quad 3\text{-}24$$

where the coordinates are:

$$\mathbf{x} = \frac{\mathbf{x_1}+\mathbf{x_2}}{2}, \mathbf{u} = \mathbf{x_1} - \mathbf{x_2} \quad 3\text{-}25$$

$$\mathbf{x_1} = \mathbf{x} + \frac{\mathbf{u}}{2}, \mathbf{x_2} = \mathbf{x} - \frac{\mathbf{u}}{2} \quad 3\text{-}26$$

Let us consider now an example of a phase-space representation of a wave-field, with the propagation in a 2D domain defined by the x-z plane. If a scalar component of the electric and magnetic field at $z = 0$ is given by a double Gaussian pulse:

$$\boldsymbol{\Psi}(\boldsymbol{x}) = \frac{1}{\sqrt{2\pi\sigma_x^2}}\left[\boldsymbol{exp}\left(-\frac{(x-\mu_1)^2}{2\sigma_x^2}\right) + \boldsymbol{exp}\left(-\frac{(\boldsymbol{x}-\boldsymbol{\mu_2})^2}{\boldsymbol{2\sigma_x^2}}\right)\right] \quad 3\text{-}27$$

where σ_x defines the pulse width and μ_1, $\mu_2$the centers.

In **Figure 3-15** the phase-space representation of this field is showcased: (a) shows the correlation function and (b) the phase-space representation of such a wave-field.

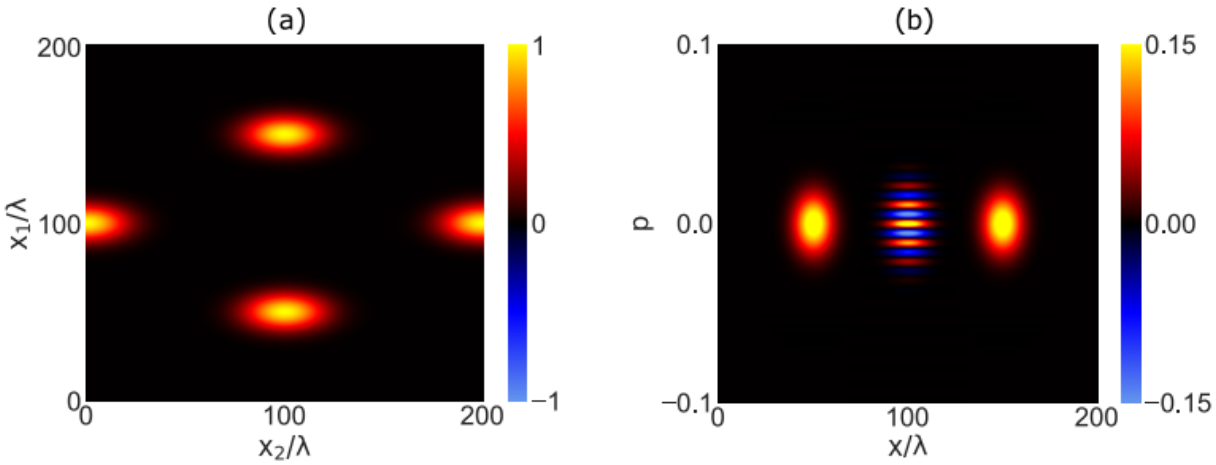

Figure 3-15 (a) correlation function and (b) phase-space representation of the double Gaussian pulse wave-field.

One can use this approach to represent the EM field scattered by a RIS, in particular by adopting a physical optics model and calculating the WDF of the scattered field upon a random plane wave incidence. The aim of this section is focused on the numerical integration of reflective surfaces generating anomalous reflections using DEA.

In this dynamical phase-space context, rays are represented in a joint space of direction cosine of the wave vector, or the ray travel direction, and the position. This technique con operate on 2D/3D meshes so it can estimate the wave propagation even in complex environments. As an example, DEA can adopt the meshes generated for FEM like in [HMT19]. The geometry for a first simple numerical example is shown in Figure 3-16 and represents a polygonal meshed shape including a RIS, represented by a red line. The EM source is defined by a localized beam as:

$$\rho_0(s,p) \approx cos^n\left(\frac{\pi}{2}(s-s_0)\right) cos^m\left(\frac{\pi}{2}(p-p_0)\right) \quad 3\text{-}28$$

Where $s \in (0, L)$ is the coordinate along the boundary (L is the total length of the billiard boundary) and p represents the momentum, in the phase-space system. The RIS represents the anomalous reflector and has been implemented by the so-called Generalized Snell Law of Reflection and Diffraction as in [YGK11]. Considering Φ as a continuous function of the position along the RIS interface, the progressive phase-shift applied to the reflected beam is obtained assuming a constant gradient of the phase discontinuity ($d\Phi/dt$) as imposed by the RIS. So, an additive term depending on the gradient of the phase along the RIS, in addition to Snell's Law, is present.

Figure 3-16 showcase the effect of the anomalous reflection by considering only one reflection of the incident beam at this RIS. The other segments of this polygonal shape example could consider the boundary conditions (totally reflecting or absorbing), in order to consider multiple reflection or in other words obtain an iterative computation to achieve an equilibrium distribution. This equilibrium solution will be illustrated in the second numerical example.

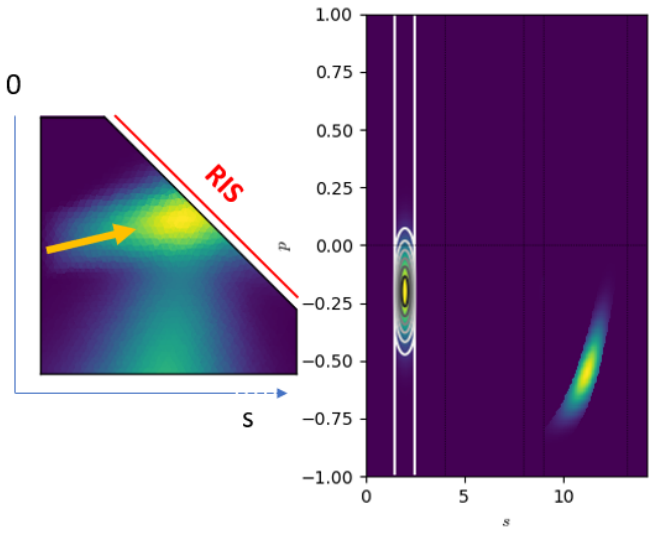

Figure 3-16 On the left the spatial density in position space is shown, with s-coordinate moving along the perimeter of the polygon. On the right side the Boundary-map's phase space in (s, p) is represented.

To highlight the angular tilt of the reflected beam controlled by the linear phase-shift, this behavior is showcased in **Figure 3-17**. It is worth noting that by varying this shift term, and assuming a linear phase gradient in accordance with the Generalized Snell Law, one can achieve this tilt.

In the second numerical example a similar polygonal geometry is adopted for the billiard, in this case a L-shape polygon, as shown in **Figure 3-18**. Let us now assume the phase gradient along the RIS constant and iterate the algorithm for several steps, i.e., consider consecutive reflections

of the incident beam along all the sides of the polygon under test. The incident beam emerges from the bottom edge and the anomalous predictable reflection sends most of the EM energy towards the region in the upper right where it is reflected. It is important to emphasize that after only 20 iterations the desired equilibrium solution has been achieved. At the same time the information related to the energy directionality is retained in the phase-space setting, because as shown in **Figure 3-18** the arrows indicate the average flow direction of the energy at different stages of the DEA run.

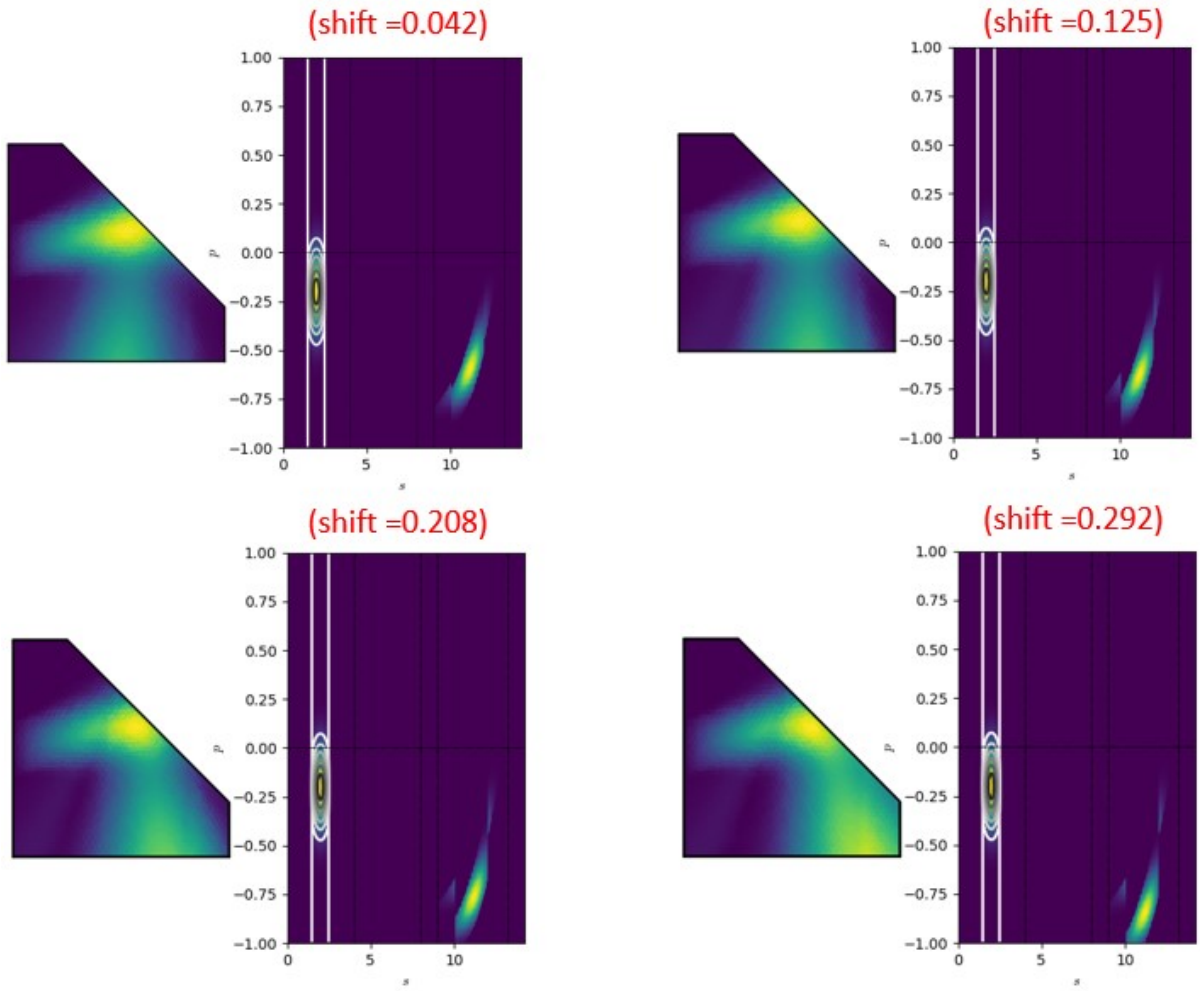

Figure 3-17 Representation of the beam in the phase-space (s,p) by varying linearly the phase gradient of the RIS, for increasing values of the shift.

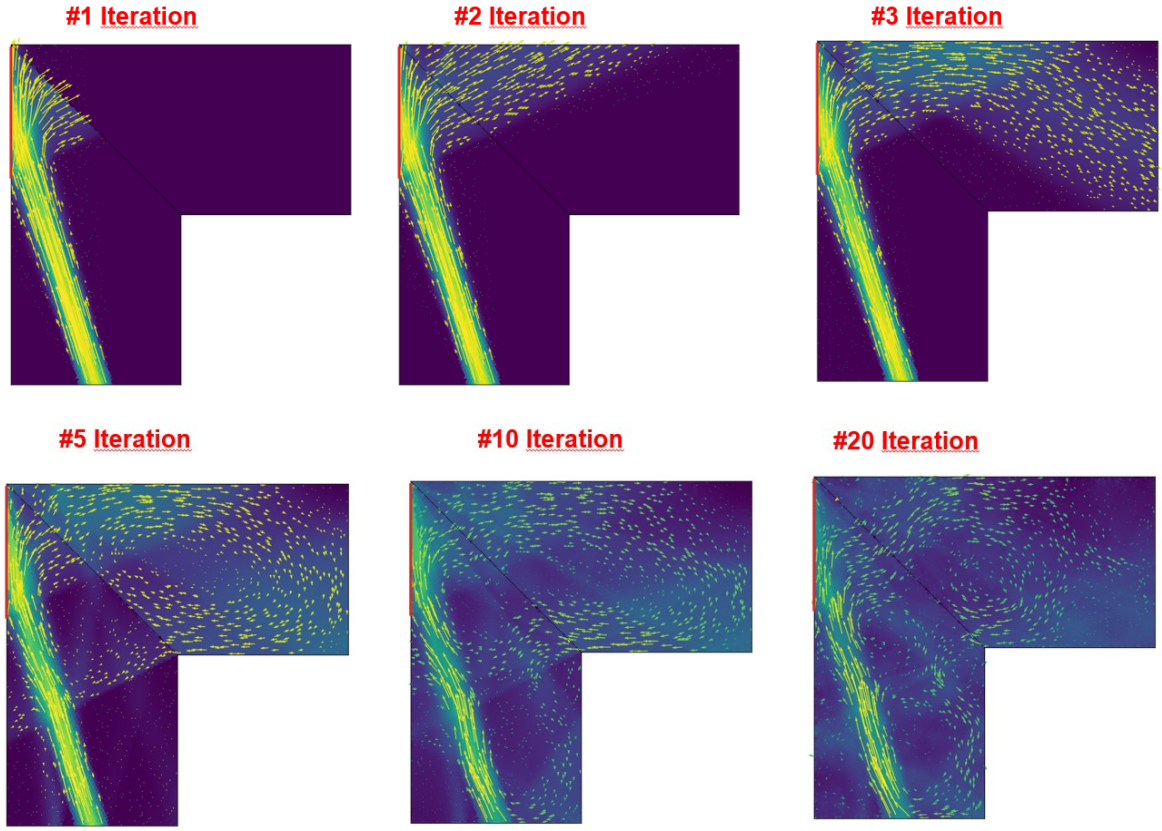

Figure 3-18 Representation of the EM fields in phase-space (s,p) by varying linearly the phase gradient of the RIS at different iterations of the algorithm. The incident beam comes from the bottom edge and the arrows indicate the average flow direction.

3.3.3 An example of inclusion of RIS in a ray-tracing based model

In this section, we briefly present the method that has been used to include a RIS in a ray-tracing based model used in the performance study [PBH22]. This study used an Orange internal ray-tracing tool called STARLIGHT®.

The following outdoor-to-indoor deployment scenario (illustrated in **Figure 3-19**) has been simulated: a BS with a massive MIMO antenna of $N = 32$ elements (4 columns and 8 elements per column) deployed on the roof top of a building is receiving data from a UE inside another building, at the ground floor. This floor has two rooms: a front room facing the BS, and a back room hidden to the BS, by the front room. The carrier frequency is $f = 3.7$ GHz. The UE has a single antenna. A RIS side of $M = 100 \times 100$ UCs is deployed on one wall inside the building (in the study, several locations are studied and compared). The uplink propagation channel between the UE and the BS, without RIS is modelled as follows.

For one position of the UE inside the building (on the ground floor), and for each antenna element n of the BS ($n = 1 \dots N$), K propagation rays are generated by STARLIGHT® between the UE and the BS (K varies depending on the UE location). For each propagation ray k, the ray amplitude α_k, the unitary vector $\vec{a}_k$ indicating the DoA at the BS, the unitary vector $\vec{d}_k$ indicating the direction of departure from the UE and the delay τ_k is generated by STARLIGHT®. The channel coefficient g_n between the UE and the BS antenna element n is then given by:

$$\mathbf{g_n} = \sum_{k=1}^{K} \boldsymbol{\alpha_k} \times \boldsymbol{e}^{-\mathrm{j}2\pi f \tau_k} \times \boldsymbol{\gamma}^{\boldsymbol{BS}}(\vec{\boldsymbol{a}}_k) \times \boldsymbol{\gamma}^{\boldsymbol{UE}}(\vec{\boldsymbol{d}}_k) \quad 3\text{-}29$$

where $\gamma^{BS}(.)$ is the BS element antenna gain as a function of the AoD, and $\gamma^{UE}(.)$ is the UE antenna gain as a function of the AoA, and $\mathrm{g} \in \mathbb{C}^{N\times 1}$.

The uplink propagation channel between the UE and the BS, with the RIS is modelled as follows.

For one position of the UE inside the building (on the ground floor), and for each UC p of the RIS ($p = 1 \dots P$), K' propagation rays are generated by STARLIGHT between the UE and the RIS (K' varies depending on the UE location). For each propagation ray k, the ray amplitude α'_k, the direction of arrival $\vec{a}'_k$, the direction of departure $\vec{d}'_k$ and the delay $\tau_{\prime k}$ is generated by STARLIGHT®. The channel coefficient q_m between the UE and the RIS UC m is then given by:

$$\mathbf{q_m} = \sum_{k=1}^{K'} \boldsymbol{\alpha'}_k \times \boldsymbol{e}^{-\mathrm{j}2\pi f \tau'_k} \times \boldsymbol{\gamma}^{\boldsymbol{RIS}}(\vec{\boldsymbol{a}}'_k) \times \boldsymbol{\gamma}^{\boldsymbol{UE}}(\vec{\boldsymbol{d}}'_k), \quad 3\text{-}30$$

where $\gamma^{RIS}(.)$ is the UC antenna gain as a function of the AoA, and $\mathrm{q} \in \mathbb{C}^{M\times 1}$.

For each UC m of the RIS and each antenna element m of the BS, STARLIGHT® generates K'' propagation rays between the UC and the antenna element. For each propagation ray k, the ray amplitude $\vec{a}''_k$, the direction of arrival AoA''_k, the angle of departure $\vec{d}''_k$ and the delay $\tau_{''k}$ is generated by STARLIGHT®. The channel coefficient w_m between the UE and the RIS UC m is then given by:

$$\mathbf{w_{n,m}} = \sum_{k=1}^{K''} \boldsymbol{\alpha''}_k \times \boldsymbol{e}^{-\mathrm{j}2\pi f \tau''_k} \times \boldsymbol{\gamma}^{\boldsymbol{RIS}}(-\vec{\boldsymbol{d}}''_k) \times \boldsymbol{\gamma}^{\boldsymbol{BS}}(\vec{\boldsymbol{a}}''_k), \quad 3\text{-}31$$

where $\mathrm{w} \in \mathbb{C}^{M\times N}$.

The RIS reflection is modelled with a diagonal matrix $\mathrm{b} \in \mathbb{C}^{N\times N}$, where $\mathrm{b}_{n,n}$ is the reflection coefficient of the UC n.

The uplink channel between the UE and the BS, with RIS is then deduced as follows:

$$\boldsymbol{g'} = \boldsymbol{g} + \boldsymbol{wbq} \quad 3\text{-}32$$

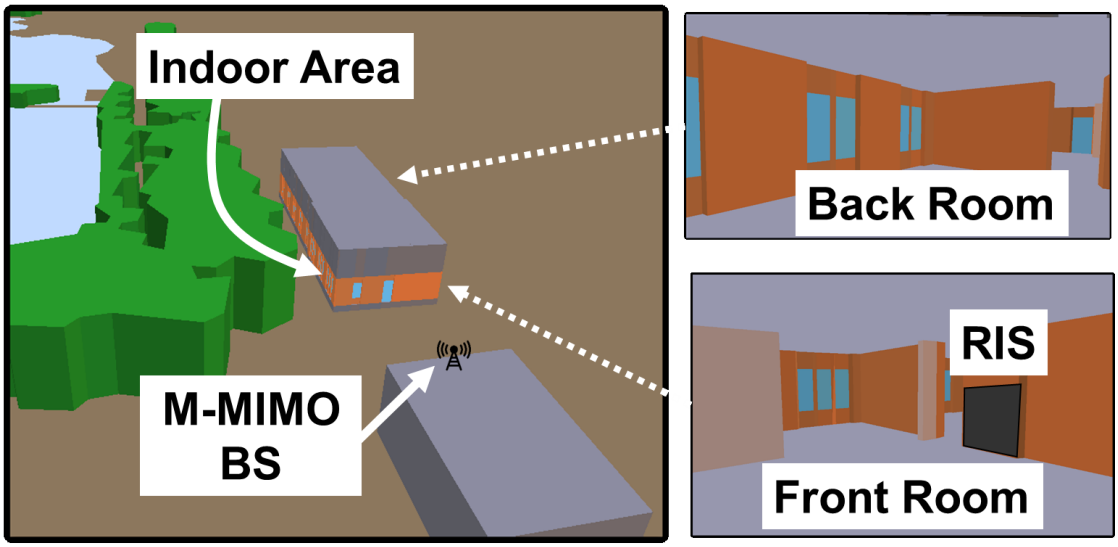

Figure 3-19 Outdoor-to-Indoor Deployment scenario

Figure 3-20 below illustrates the examples of rays generated by STARLIGHT between one position of the UE and the 1 element of the BS. Note that a ray is represented by a sort of transparent piple, with non-zero thickness.

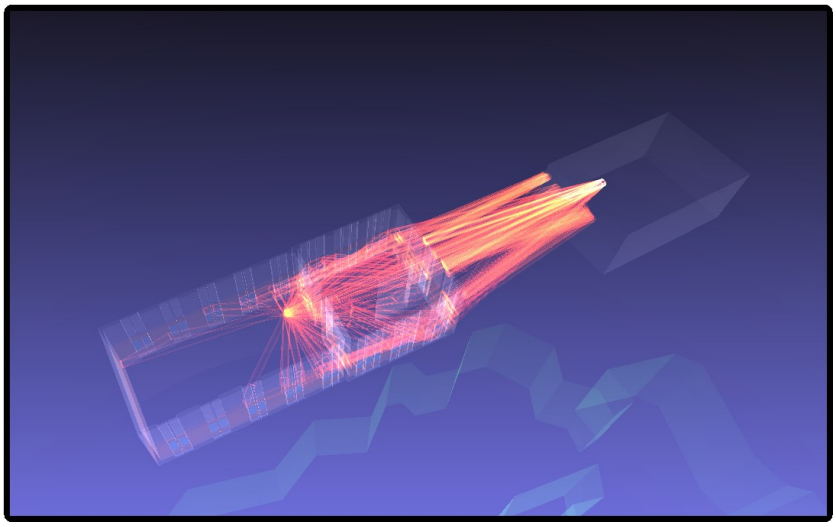

Figure 3-20 Example of rays between one position of the UE indoor and the 32 elements of the BS

Figure 3-21 below illustrates the examples of rays generated by STARLIGHT between the position of the center of the RIS and the 1 element of the BS. Note again, that a ray is represented by a sort of transparent piple, with non-zero thickness.

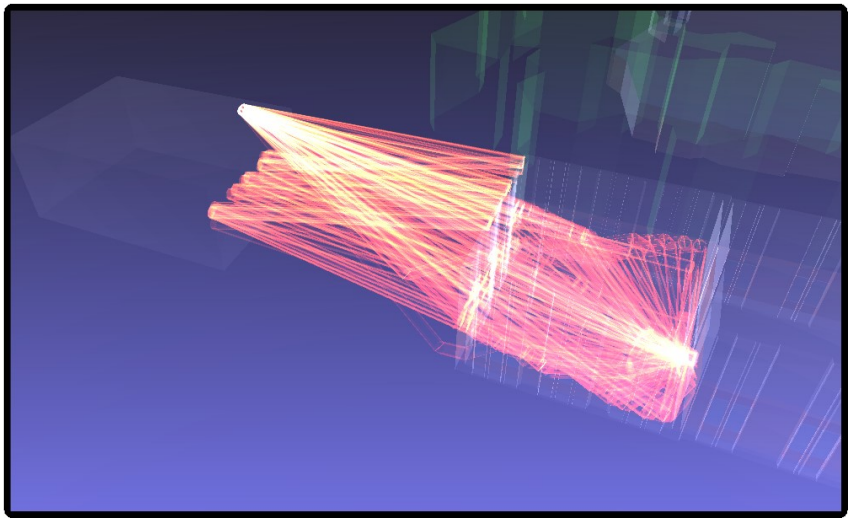

Figure 3-21 Example of rays between the position of the center of the RIS indoor and the 32 elements of the BS.

Figure 3-22 a) below illustrates the UE-to-BS channel power $\mathrm{g}^{\mathrm{H}}\,\mathrm{g}$ (where $.^{\mathrm{H}}$ is the Hermitian operator) without RIS. Figure 3-22b) below illustrates the gain in channel power due to the introduction of the RIS (i.e. $10log_{10}(\mathrm{g}'^{\mathrm{H}}\,\mathrm{g}'/\mathrm{g}^{\mathrm{H}}\,\mathrm{g})$). These results assume an optimisation of b that is explained in [PBH22].

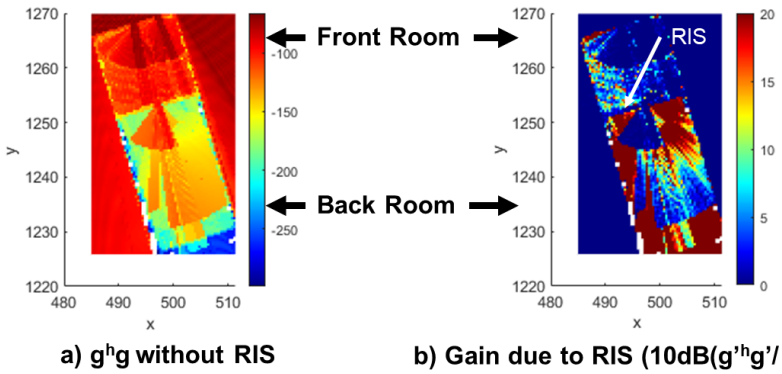

Figure 3-22 Example of rays between the position of the center of the RIS indoor and the 32 elements of the BS.

3.4 RIS enabled channel sounding and modelling

3.4.1 Transmissive RIS enabled channel sounding

The channel measurements were carried out in an InF environment considering two setups similar to the one illustrated in D3.1. In the first setup, a circularly polarized transmissive RIS was employed at the TX side. A vertically polarized monopole antenna (of measured gain 0 dBi) was considered at the RX side. Both the TX and RX antennas were at the same height of 1.54 m above the ground. Measurements were performed in the $26-30$ GHz frequency band, sweeping 801 frequency points. The transmissive RIS scans the environment from -60^o to 60^o following a step of 5^o. A second setup is based on VCA where the transmitarray is replaced by a wideband monopole antenna placed on a X-Y-Z scanner performing $5 \times 5 \times 5$ spatial grids of a half-wavelength grid step, i.e. 5 mm.

Three propagation conditions were investigated, namely LOS, OLOS and NLOS. To increase the dynamic range for both the OLOS and NLOS conditions, a low noise amplifier of 20 dB was used at the RX side in the second setup. The InF environment floor plan is shown in Figure 3-23 (a) and (b) presents an example of OLOS scenarios for the first setup, i.e. transmissive RIS and the Rx monopole antenna.

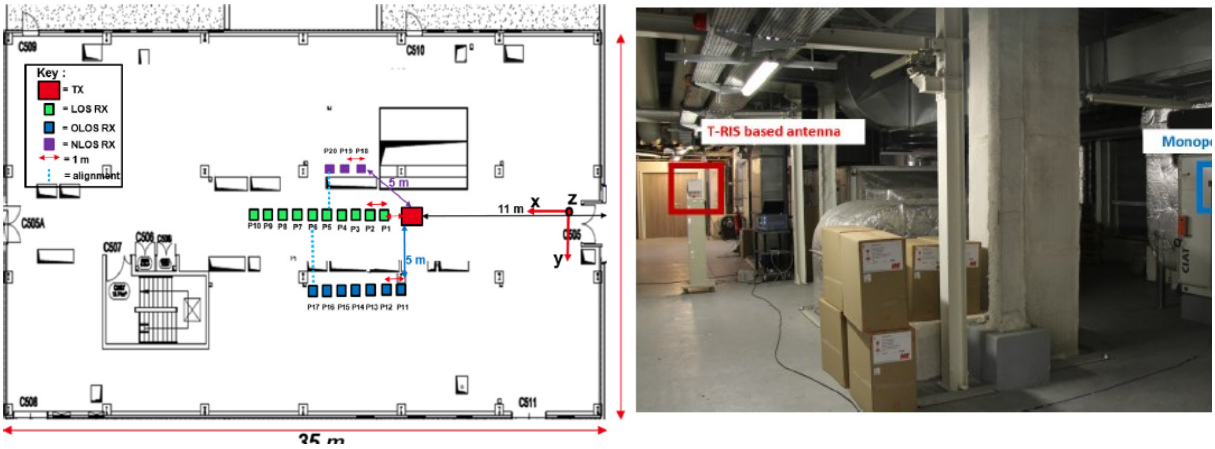

(a) (b)

Figure 3-23 Channel measurement campaign: floorplan (a), picture (b).

As first step, we analyse the impact of the beamforming transmissive RIS on CG and DS, according to the phase distribution on the transmissive RIS, i.e. the target steering angle. In Figure 3-24, we can see that for LOS positions (i.e. $P1-P10$), the highest CG (antenna embedded) is obtained in the direction $\phi_s = 0^o$. In OLOS, i.e. for positions $P11-17$, the highest CG is in the directions $\phi_s = 55^o$, $\phi_s = 30^o$, $\phi_s = 60^o$, $\phi_s = 50^o$, $\phi_s = 45^o$, and $\phi_s = 40^o$, respectively. At position $P12$ we notice that in the directions $\phi_s = 55^o$ and $\phi_s = 60^o$, which geometrically are expected to record maximum powers, the channel gain is almost the same with that observed at $\phi_s = 30^o$. For NLOS, positions $P18, P19, P20$, the highest CG is in the direction $\phi_s = -60^o$ for all the three positions. With regards to the DS, Figure 3-24 shows that the DSs appear to be inversely related to the CGs, but in NLOS where the maximum CG is achieved at $\phi_s = 20^o$ while the minimum DS is at $\phi_s = 5^o$. In general small delay spread values are observed in the directions of the highest CG for LOS and OLOS (where somehow a predominant path is observed).

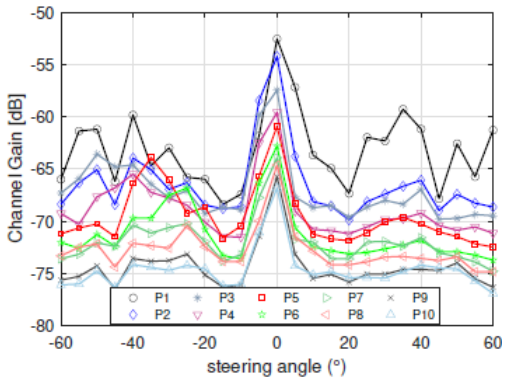

(a) $P1-P10$

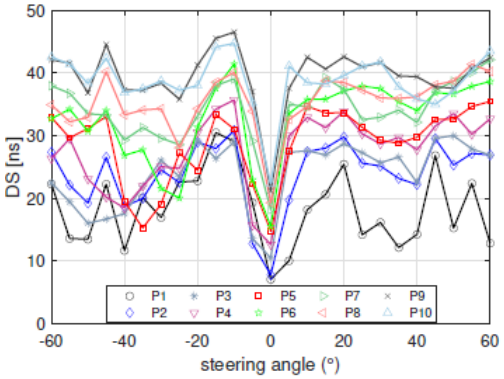

(b) $P1-P10$

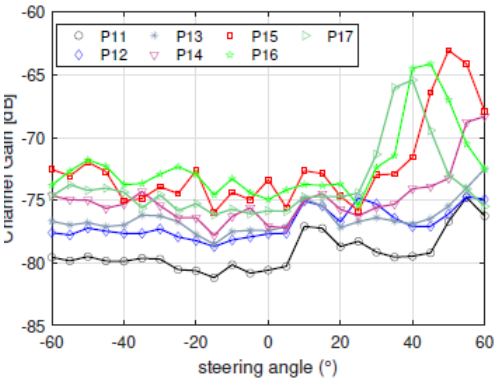

(c) $P11-P17$

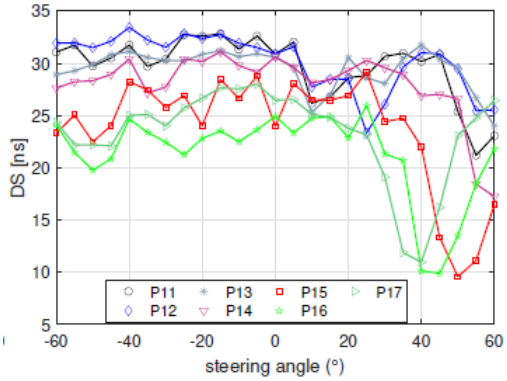

(d) $P11-P17$

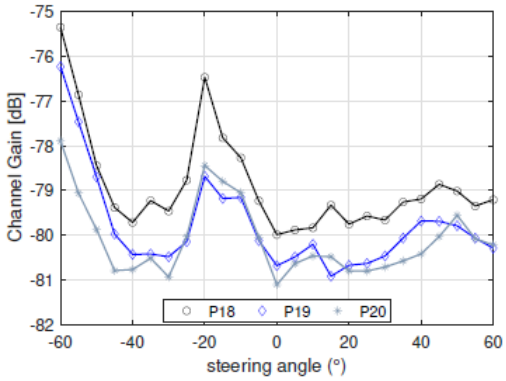

(e) $P18 - P20$

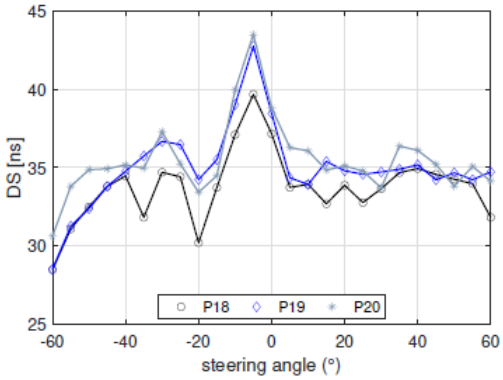

(f) $P18 - P20$

Figure 3-24 InF scenario CG and DS per steering angle for the different scenarios.

In the literature, channel modelling at mmWave is often based on mechanical steering of directive antennas. The measurements collected are then used to obtain the omnidirectional power delay profile in order to retrieve the channel characteristic. In our work, we synthesize the omnidirectional power delay profile from channel measurements involving the electronic steering of a transmissive RIS.

At this point, it is worth mentioning that the main difference with respect to the classical mechanical steering is the influence of the antenna gain pattern. When operating the mechanical steering, typically with directive horn antennas, the half power beam width, as well as the side lobe is constant regardless the steered angle. Here, because of the electronically steering the gain pattern change according to the steered angle. Hence an adaptive compensation of the gain and side lobe effect has been operated to compensate.

Figure 3-25 shows examples of the synthesized PDPs and scatter plots for different positions in the InF environments. Having synthesized the PDPs and identified the temporal and angular parameters of the MPC, we then proceed to apply the K-mean clustering algorithm in order to identify the clusters.

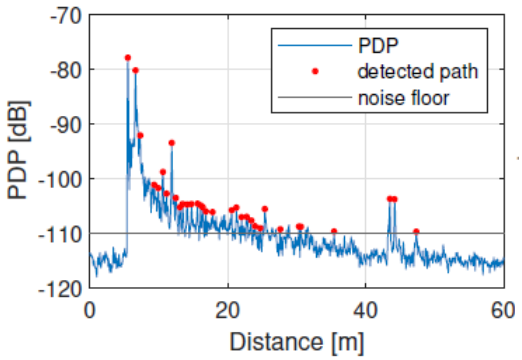

(a) LOS ($P5$)

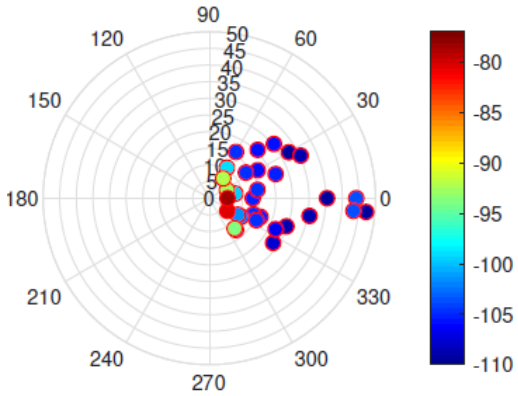

(b) LOS ($P5$)

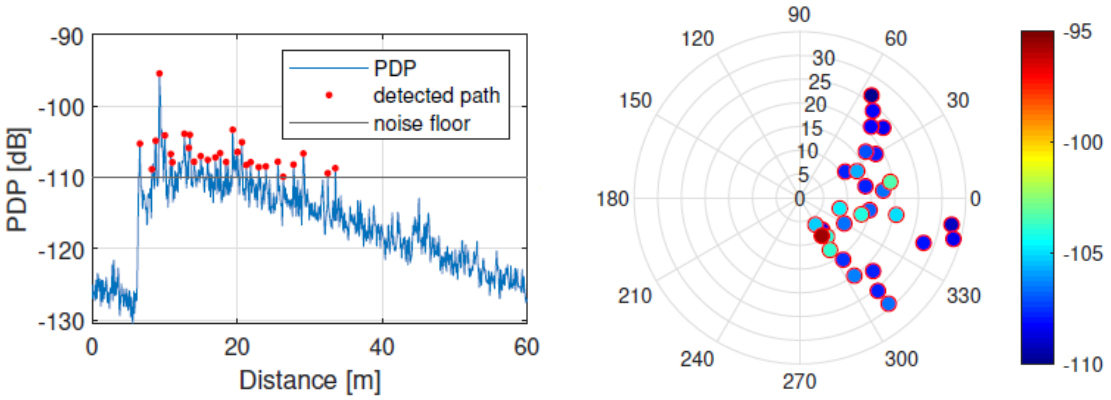

(c) NLOS $P19$ (d) NLOS $P19$

Figure 3-25 Example synthesized semi-directional PDPs and scatter plots for the InF environments.

The cluster characteristics are then compared to those obtained from the VCA channel measurements. In the second setup of measurements, the UWB-SAGE algorithm was used for the MPCs detection and channel parameters estimations. The spatial channel information can be then incorporated into the extended version of the Saleh-Valenzuela model.

Comparing the results between VCA and transmissive RIS based PDP syntheses (Table 3-1), we can see a good similarity on both Inter- and Intra- cluster decay, as well as the time of arrival rates. The main disagreement is on the Intra-cluster DS when considering all the scenarios (i.e. merging LOS, OLOS, NLOS). The inclusion of NLOS/OLOS in the statistic evaluation could indeed be affected by the reduced angle of vision provided by the transmissive RIS based measurements.

Table 3-1 DECAY RATE AND ARRIVAL RATE OF CLUSTERS AND RAYS.

Scenario InF	$\Gamma\ (ns)$	$\gamma\ (ns)$	$1/\Lambda\ (ns)$	$1/\lambda\ (ns)$
VCA omni $P1-P20$	29.9	48.4	9.5	13.4
VCA omni $P1-P10$	13.9	38.8	6.3	9.9
Transmissive RIS "Omni" $P1-P20$	29.8	39	9.1	9
Transmissive RIS "Omni" $P1-P10$	14.5	41.6	6.6	10.1

3.4.2 Reflective RIS enabled channel sounding and modelling

The reflective RIS assisted wireless communication channel has been measured and characterized in the laboratory of CEA, with cooperation with GNW. Four different setups were considered, as shown in Figure 3-26:

- Setup 1: Reflect array (RA) mode with a far-away horn antenna
- Setup 2: Reflective RIS (extender mode) with two far-away horn antennas
- Setup 3: Reflective RIS (extender mode) with one horn antenna and one monopole antenna
- Setup 4: Reflective RIS (extender mode) with one TA and one monopole antenna

The heights of the reflective RIS, the horn antenna and the monopole antenna are respectively about 1.65 m, 1.64 m and 1.6 m. For a given location of the pair TX-RX, the reflective RIS involves an optimization algorithm in order to steer the beam toward the RX. The aforementioned algorithm requires as input i) the X, Y, Z coordinates of the TX and ii) the expected azimuth and elevation angles of the RX. After a fixed number of iterations, the algorithm will give the X, Y, Z of TX and the azimuth and the elevation of the RX that maximize the CFR at the RX side (through considering as a feedback the S_{21} parameter measured by the vector network analyser (VNA)). For each setup, the optimization algorithm is launched to find the optimal beam at the operating frequency of the RIS, i.e., 28 GHz with a narrow bandwidth of 1 GHz. Nonetheless, the propagation channel is measured over a larger bandwidth (i.e., 25 GHz - 35 GHz), in order to be able to characterize the channel response.

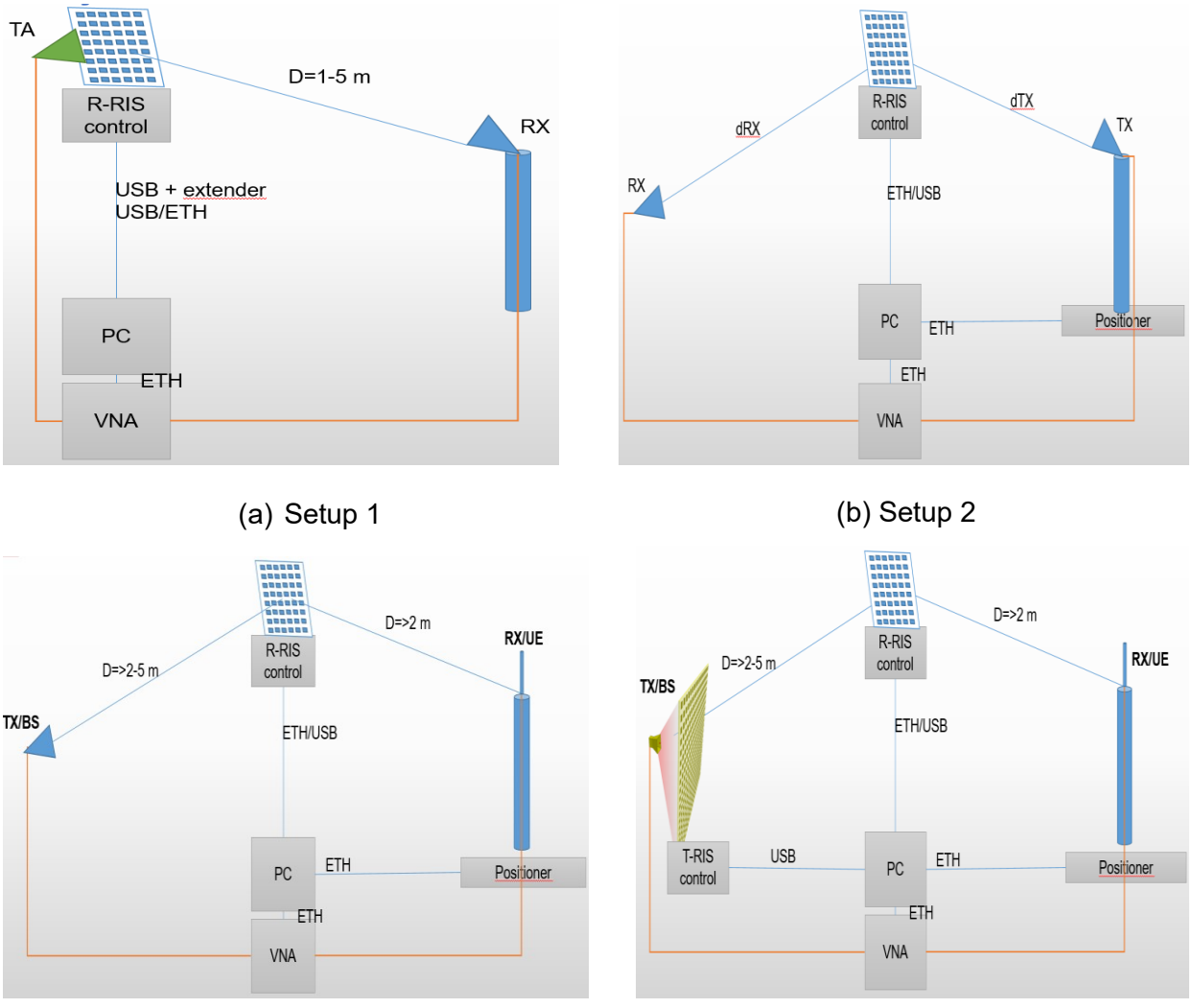

(a) Setup 1

(b) Setup 2

(c) Setup 3

(d) Setup 4

Figure 3-26 Reflective RIS channel measurement setups.

Setup 1: RA mode

As shown in Figure 3-27 (a), a RA is used with a small TX horn antenna mounted on the reflective RIS, with an approximate position of ($X = 0$, $Y = 100$ mm, $Z = 173$ mm). The measurement

plan and environment are shown in Figure 3-27 (b). The RX horn antenna was placed at different distances with respect to the RA antenna (i.e., 50 cm, 2.6 m, 3m, 4m, and 5m) as well as at different incidence angles (both $-45°$ and $0°$ as azimuth and $0°$ as elevation). For each configuration, the TX-RX channel has been measured in the frequency domain. We show the results here for an RX at a distance of 2.6 m, while considering i) the optimal beam resulting by applying the optimization algorithm (opt. steering: RX($\phi = -46°$, $\theta = -5°$) and TX($\phi = -3.8°$, $\theta = 27.1°, X = -12, Y = 93,\ Z = 181$)), ii) a fixed beam resulting from an optimization for an RX at 0.5 m (fixed steering: RX($\phi = -31°, \theta = -24°$) and TX ($\phi = 3.16°, \theta = 35.4°\ X = 9, Y = 116,\ Z = 163$)), and finally iii) with the RIS turned off (RIS off). We note that the expected values are: RX ($\phi = -45°, \theta = 0°$) and TX ($\phi = 0°, \theta = 30°, X = 0, Y = 100, Z = 173$).

(a) (b)

Figure 3-27 Measurement plan (left) and environment (right) for setup 1.

The phases profiles are shown in Figure 3-28 and the CFR is shown in Figure 3-29. In the three cases, the principal and single path (reflected by the RIS) is well-resolved at the same distance but obviously with different powers. The highest power corresponds to the case of optimal steering and the lowest one corresponds to the RIS off.

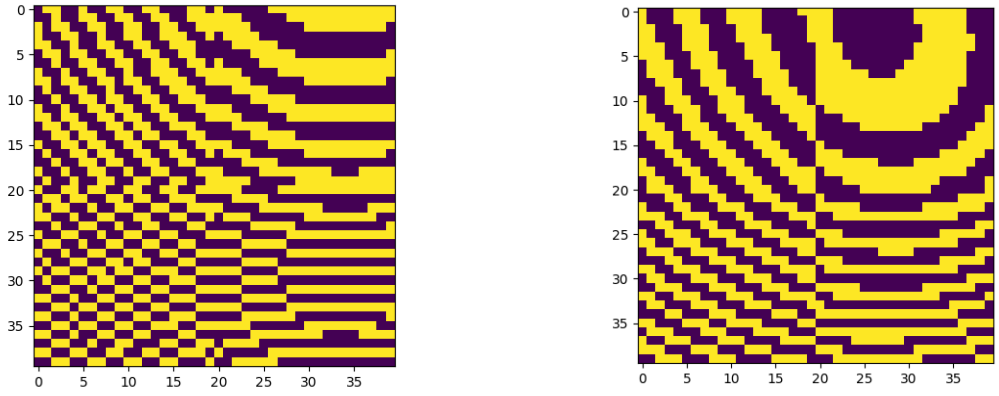

(a) (b)

Figure 3-28 The phases profile of the RIS resulting from (a) the optimization algorithm and (b) a fixed beam with expected TX and RX locations.

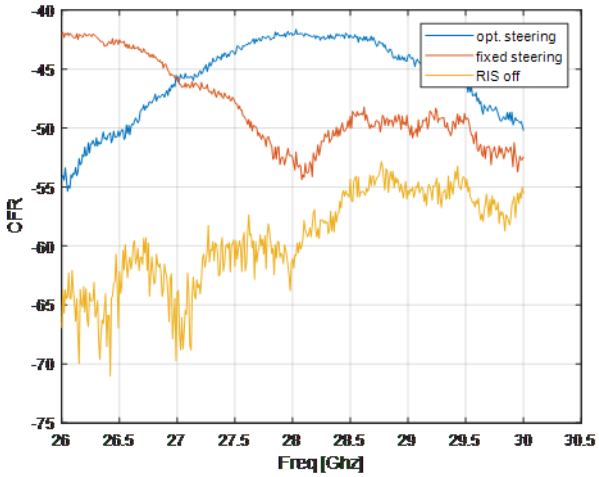

Figure 3-29 Setup 1: CFR and PDP for an RX at 2.6 m.

Setup 2: Extender mode with two far-away horn antennas

As shown in Figure 3-30, the setup 2 corresponds to the extender mode where both TX and RX are far-away horn antennas of a gain of 17 dBi each. While the position of TX is fixed ($\phi = 45°, \theta = 0°$ with a distance to RIS of about 2 m), the RX is placed at 3 different distances (i.e., 1 m, 3 m and 4 m with approximately $\phi = -15°, \theta = 0°$). For each RX location, the optimization algorithm is launched to find the optimal steering vector. For an RX at 1 m, the optimization algorithm estimates that RX ($\phi = -12°, \theta = -5°$) and TX ($\phi = 42°, \theta = 1{,}6°, X = 612, Y = 26, Z = 680$). The corresponding estimations for an RX at 3 m are RX($\phi = -15°, \theta = 0°$) and TX ($\phi = 48°, \theta = -3°, X = 1634, Y = -118, Z = 1474$). The case of an RX at 4 m corresponds to an optimal steering vector at RX ($\phi = -12°, \theta = 1°$) and TX ($\phi = 42.4°, \theta = -4.6°, X = 1150, Y = -136, Z = 1258$). The results in Figure 3-31 obviously show that the CFR increases when the RX is closer to the RIS.

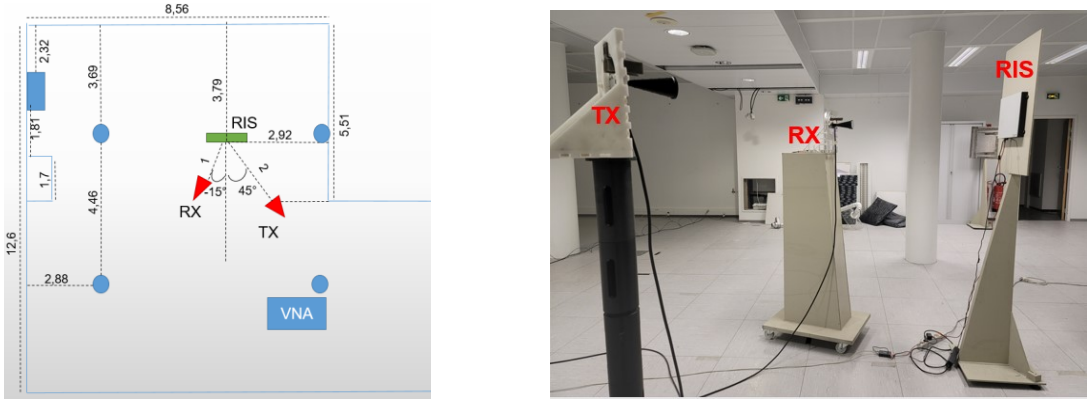

(a) (b)

Figure 3-30 Setup 2: Measurement plan (a) and environment (b).

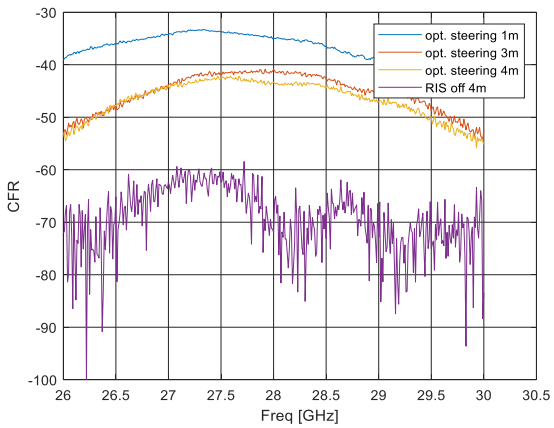

Figure 3-31 Setup 2: CFR and PDP for an RX horn antenna at different distances.

Setup 3: Extender mode with one horn antenna and one monopole antenna

Setup 3 concerns the usage of a monopole antenna as an RX at a distance of 2 m to the RIS and angles ($\phi = 45°, \theta = 0°$). A virtual network is performed by moving the monopole antenna over a 3×3 square grid with a step of 4.3 mm. The TX is a horn antenna positioned at a distance of 4 m to the RIS with expected parameters ($\phi = -15°, \theta = 0°, X = -850, Y = 0, Z = 3850$). The optimal steering vector is found by replacing the monopole by a horn antenna (RX ($\phi = 41°, \theta = -3°$) and TX ($\phi = -8{,}6°, \theta = -0.8°, X = -654, Y = -61, Z = 4313$)). Accordingly, the CFRs for a horn-to-horn channel and horn-to-monopole channel are shown in Figure 3-32. Given that the gain of the horn is higher than that of a monopole, the horn's CFR is higher than that of a monopole. In the time domain, the results show that both horn and monopole can resolve the path reflected by the RIS with approximately the same distance. The difference in power corresponds to the gain of the horn antenna (17 dB). Because of the omnidirectivity of the monopole, it can resolve much more paths than the directive horn antenna.

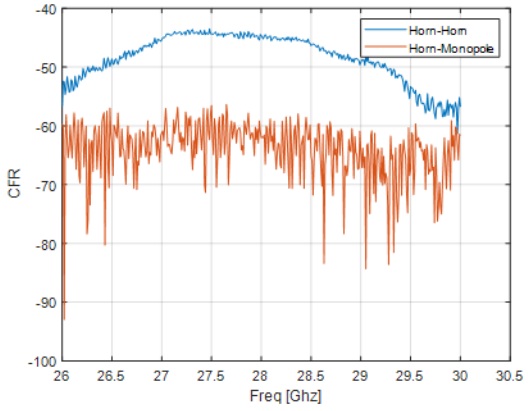

Figure 3-32 CFR and PDP for a horn-to-horn channel and horn-to-monopole channel.

The measurement plan and environment are shown in Figure 3-33 for the case of an obstructed LOS between TX/BS and RX/UE (user). Figure 3-34 shows the results comparing the case of RIS on vs. off for the case of a LOS between TX-RX as well as those comparing the case of LOS vs. OLOS with a RIS on. Considering RIS on vs. off (Figure 3-34(a)), almost the same structures of MPCs are present except for the very attenuated path reflected by the RIS off. Similarly for the case of LOS vs. OLOS (Figure 3-34(b)), almost the same structures of MPCs are present except the absence of the LOS path for the OLOS case.

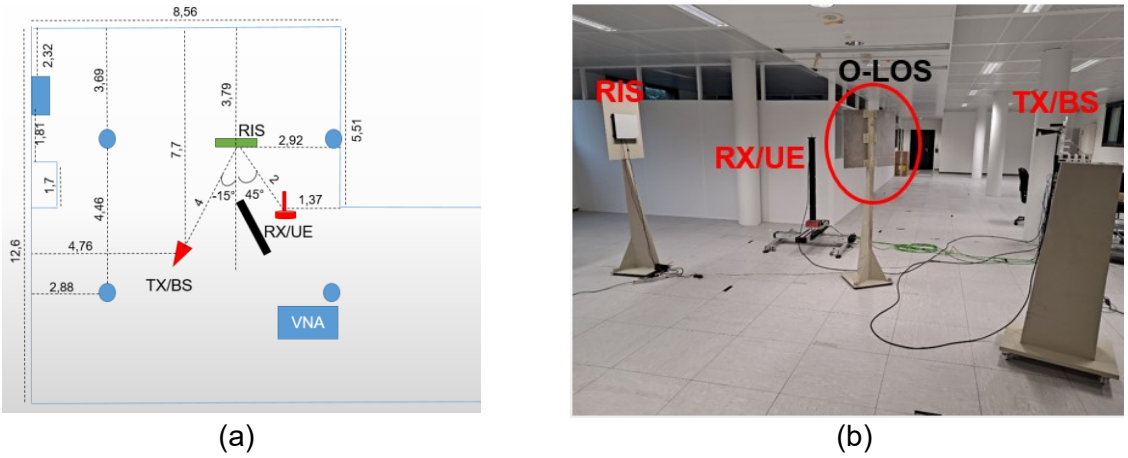

(a) (b)

Figure 3-33 Setup 3: Measurement plan (a) and environment (b) for an OLOS.

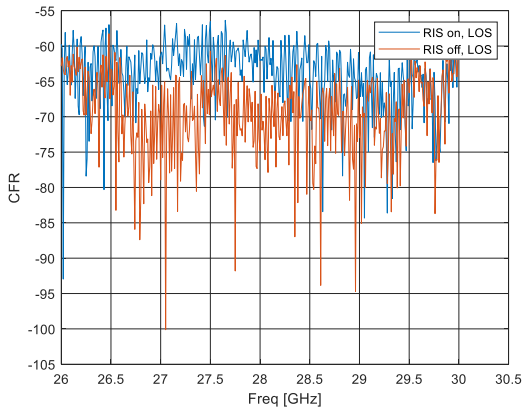

(a) RIS on vs. RIS off, LOS case

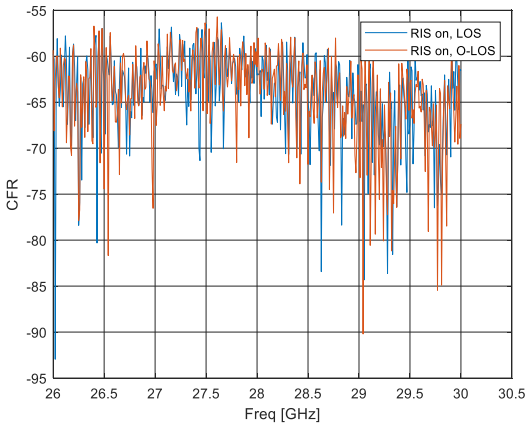

(b) LOS vs. OLOS, RIS on case

Figure 3-34 CFRs and PDPs for (a) RIS on vs. off and (b) LOS vs. OLOS.

Setup 4: Extender mode with one transmit-array (TA) and one monopole antenna

In the setup 4 (see Figure 3-35), we replace the TX horn antenna by a TA for which we are able to control the direction of the steering beam ($\phi_{S,BS}$). For a beam directed toward the RIS, the angle is $\phi_{S,BS} = 0°$, while it is equal to $\phi_{S,BS} = -30°$ for a steering toward the RX/UE.

(a) (b)

Figure 3-35 Setup 4: Measurement plan (a) and environment (b).

In Figure 3-36(a), we compare the channel when the RIS is off for two different TX antennas: the horn (directed toward the RIS) or the TA with a steering angle toward the RIS ($\phi_{S,BS} = 0°$). The two channels almost share the main paths (i.e., the LOS path and another one reflected by the window behind), with a higher power corresponding to using the TA as a TX. More MPCs are present in the channel measured with a horn TX antenna because of its higher aperture of its radiation pattern, compared to that of a TA. Figure 3-36(b) compares between whether steering the TA/BS toward the RIS ($\phi_{S,BS} = 0°$) or the RX/UE ($\phi_{S,BS} = -30°$), while the RIS is off in both cases. The latter case will imply a higher LOS path between the TA and the UE, with a power of −43.55 dB.

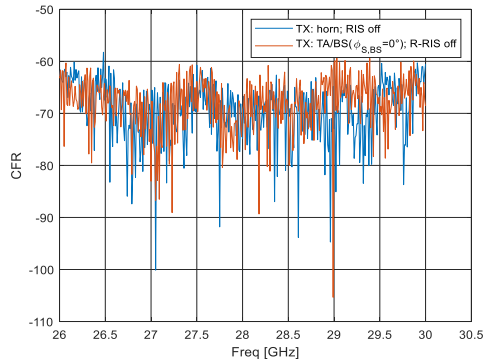

(a) TX : horn vs. TX : TA/BS($\phi_{S,BS} = 0°$)

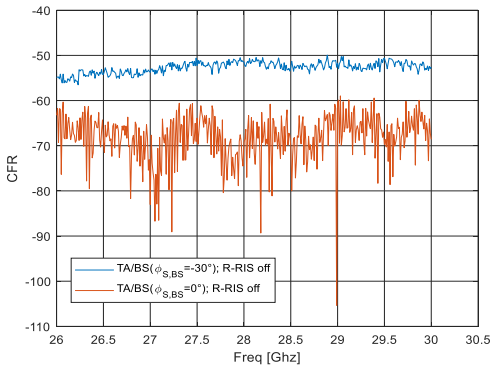

(b) $\phi_{S,BS} = -30°$ vs. $\phi_{S,BS} = 0°$

Figure 3-36 CFRs and PDPs for RIS off, while TX is either the horn or the TA/BS with $\boldsymbol{\phi_{S,BS} = 0°}$ or $\boldsymbol{\phi_{S,BS} = -30°}$.

Figure 3-37 presents the results of CFRs when the TA is steering toward the RIS. We consider for comparison different cases: Reflective RIS on vs off for the LOS case, and LOS vs. OLOS for the RIS on case. Eventually, turning on the RIS with an optimized configuration will imply much higher reflected path (Figure 3-37 (a)). Moreover, putting an obstacle between the TA and the UE will imply a disappearing of the LOS path (Figure 3-37 (b)).

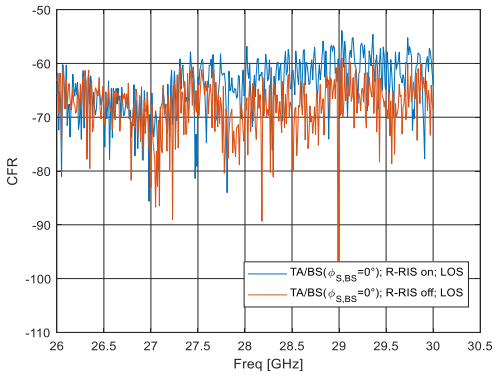

(a) Reflective RIS on vs. Reflective RIS off, LOS case

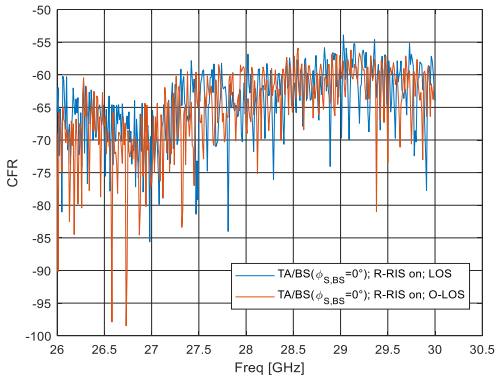

(b) LOS vs. OLOS, Reflective RIS on case

Figure 3-37 CFRs and PDPs for (a) Reflective RIS on vs. Reflective RIS off, LOS case, and (b) LOS vs. OLOS, Reflective RIS on case.

4 Conclusions and outlook

4.1 Towards a generalized RISE-6G modelling framework

In order to support RIS deployment of real-life scenarios we need to understand their statistical propagation characteristics. The methodology employed to generalize the impedance model for scattering clusters in section 3.2.1 can be further augmented to include both US and link variability. In particular, the results in section 3.2.1 have been obtained by placing scattering clusters in specific configurations that have been selected to create partial or total blockage of some LOS channels. While these conditions are significative to formulate a joint beamforming between BS and RIS [MSG+21], a better understanding of the transmission statistics in the realm of dynamic RIS-assisted propagation would benefit from considering i) random spatial collocation of clusters, and of dipoles within individual clusters; ii) multipath fading coexisting with LOS channels among transmit/receive array, RIS, and US. This is depicted in Figure 4-1 with an example of interaction between scattering clusters and RIS.

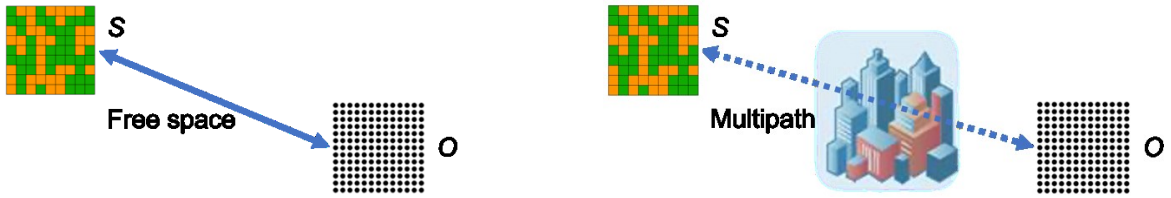

(a) (b)

Figure 4-1 Interaction between RIS and dipole-based US in free space (a) and under multipath fading (b), where LOS and NLOS contribution coexist and are modelled by the random coupling model.

The former aspect has been addressed by the dipole-based strategy described in [FSA22, MSG+21], and a solution for the latter aspect is provided by the RCM discussed in section 3.1.1 and [GYX14], where the effect of multipath fading was restrained to uplink and downlink impedance matrices. Starting from the impedance-based channel model [GB21], the fusion of the RCM with the partitioned mutual impedances in Eq. 3-12 and 3-13 is expressed as

$$\boldsymbol{Z}_{EE} = \begin{bmatrix} \boldsymbol{Z}_{oo} & \boldsymbol{Z}_{os} \\ \boldsymbol{Z}_{so} & \boldsymbol{Z}_{ss} \end{bmatrix} + \begin{bmatrix} \boldsymbol{0} & \boldsymbol{Z}_{os} \\ \boldsymbol{Z}_{so} & \boldsymbol{0} \end{bmatrix}^{1/2} \begin{bmatrix} \boldsymbol{0} & \boldsymbol{\xi}_{so} \\ \boldsymbol{\xi}_{os} & \boldsymbol{0} \end{bmatrix} \begin{bmatrix} \boldsymbol{0} & \boldsymbol{Z}_{os} \\ \boldsymbol{Z}_{so} & \boldsymbol{0} \end{bmatrix}^{1/2}, \tag{4-1}$$

for the environment impedance matrix, while the active impedances and the load impedances in Eq. 3-11 are left unchanged. In Eq. 4-1, the entries $\xi_{.,ij}$ of the normalized $\xi_{.}$ matrices have universal fluctuation controlled by a scalar parameter $\alpha_{.,ij}$ describing the fading magnitude in the channel between the elements i and j, and the superscript 'fs' has been omitted in all the impedance matrices. It is worth remarking that Z_{EE} enters non-linearly in the matrix Φ_{SS}. Furthermore, the mutual impedances between transmit/receive array and environment assume a similar formal structure of the partition matrix Eq. 4-1.

Importantly, not all the partitioned free space impedance matrices are system specific: The dipole-based US can be computed efficiently using the closed-form expressions obtained in Section 2.2.3 for the mutual coupling impedances. A classification of the interactions between elements of the environment is reported in Figure 4-2, with the caveat that the propagation channels (blue dashed line arrows) support both LOS and NLOS channels from the environment variability. All the active impedances, including Z_{OO}that captures distributed groups of dipoles configuring US, can be calculated by relatively fast full wave simulations in CST and HFSS, including Z_{SS} in case of multiple RISs of different type, as well as Z_{RT} for different transmit and receive antenna array. In use case relevant to RISE-6G where transmit/receive arrays and RISs are static and objects are dynamic, an approximated mathematical expression is needed for Z_{RO}, Z_{OT}, Z_{OS}, so that to capture the distance fluctuation (only for random cluster collocation), while a semi-analytical model of Z_{RS}, Z_{ST} can be constructed based on antenna steering vectors. An analysis presented in [IN10] reveals that, starting from the field received by an array element m excited by an element n that is driven by a current i_n, and is far apart of $\Delta r_{m,n}$ with respect to the reference element,

$$\boldsymbol{E}_m = \boldsymbol{e}_0 \frac{e^{-jkr}}{r} \boldsymbol{g}_T(\boldsymbol{\theta}_T)\, e^{-jk\Delta r_{m,n}}\, \boldsymbol{i}_n, \tag{4-2}$$

the mutual impedance between minimal scattering dipoles (in absence of mutual coupling between array elements) is related, up to a complex-valued constant γ, to the associated antenna array steering vectors a_T and a_R, viz.,

$$\boldsymbol{Z_{TR}} = \boldsymbol{\gamma}\frac{e^{-jkr}}{r}\,\boldsymbol{a_R(\theta_R)}\cdot\boldsymbol{a_T^t(\theta_T)}, \qquad 4\text{-}3$$

for isotropic antenna array elements. This gives an approximation to the mutual impedance matrix if the antenna element radiation patterns g_T and g_R are obtained from full wave simulations, viz.,

$$\boldsymbol{Z_{TR}} = \boldsymbol{\gamma}\frac{e^{-jkr}}{r}\boldsymbol{g_T(\theta_T)}\,\boldsymbol{g_R(\theta_R)}\,\boldsymbol{a_R(\theta_R)}\cdot\boldsymbol{a_T^t(\theta_T)}, \qquad 4\text{-}4$$

where γ is now a normalization factor that needs to be estimated by full-wave simulations.

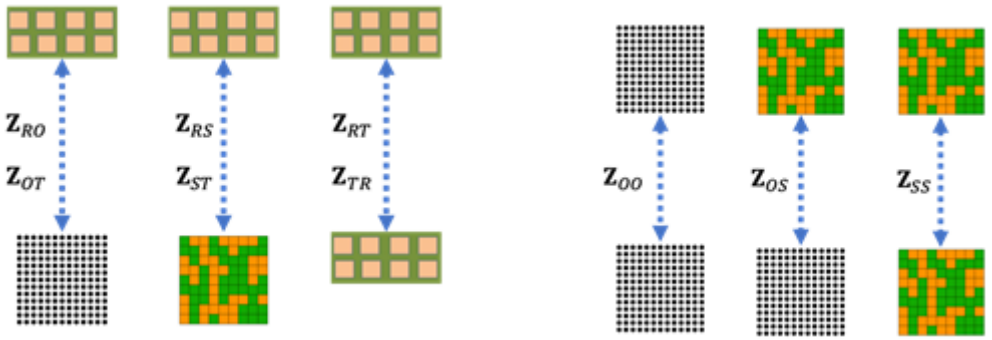

Figure 4-2 Classification of interactions between Tx/Rx array, US, and RIS elements

In summary, the RISE-6G advanced EM modelling activity has devoted special attention to the impedance matrix formalism and has understand the inherent behavior of RIS assisted MIMO systems at their multiple ports, establishing a generalized hybrid geometric-statistical model that integrates the mutual impedance channel model, informed by full wave simulations of active- and trans-impedance matrices, with dipoles scattering clusters under deterministic/statistical collocation, also augmenting the transimpedances with the random coupling model between cluster and RIS/antenna arrays to capture multipath fading.

4.2 Next steps for modelling extension and validation

We have assessed and enhanced the advanced EM models developed within RISE-6G. The research activity undertaken in D3.1 has: i) Achieved preliminary E2E model verifications of the RIS operating in free space; ii) Led to the creation of a general modelling framework that includes multi-path fading; iii) Consolidated the basic mathematical theories that reduce EM models to system models; iv) Devised the integration of RIS models within different RT algorithms. The effort covered so far spanning through D3.1 and D3.1., has successfully employed WP3 models fruitfully in performance analysis (WP4) and EM field enhancement (WP6) in idealized conditions such as free-space and rich multipath fading. Further work will be conducted to bring the modelling activity to conclusion, especially considering RIS prototype design and intelligent propagation environments analysis under real-life, i.e., non-idealized, conditions, which will require:

1. Finalise the assessment of the impedance-based E2E channel model in D3.4.
2. Consolidate the link between impedance-based model with abstract system-level models of the received signal.
3. Extend impedance-based beyond the minimal scattering approximations through the method of moments.
4. Harmonize the impedance-based models for arbitrary (heterogeneous) wireless channels with frequency selectivity, geometric scattering clusters, and multipath fading.
5. Finalise the integration of RIS scattering models within spatial-angular (phase-space) RT algorithms such as DEA and produce results for selected 2D environments.
6. Formulate and assess an extension of RIS path loss models and their inclusion in power balance methods for link budget calculations (WP6).
7. Extend geometric channel models and their integration with channel sounding/measurements
8. Finalize the FDTD algorithms for transmissive RIS and reflective RIS structures, which requires understanding the numerical stability and dispersion introduced by discretized GSTC boundary conditions.
9. Finalize the random plane wave superposition excitation of FDTD algorithms to assess the emulation of reverberation chambers.

By the time of D3.4 delivery, the RISE-6G models will have addressed open scientific problems of importance in the wireless communication community, including mutual coupling, roughness, reradiation, resonant UC behaviour, wider role of impedance matrices in design, as well as the integration of advanced EM models within commercial full-wave simulation tools (with particular emphasis on MoM and RT). The focus of the activities will be devoted to address the operation of the RIS in non-idealised environments, i.e., few multipath components and non-uniform field diffusion. All the models will have provided a substantial advancement in the theoretical suite of tools available for RIS design and coverage planning of beyond 5G/6G mobile communication networks.

The models and assessment that we carried put within RISE-6G have been disseminated and will inform the ETSI SIG on RIS within the duration of the project, e.g., BOI in the Annex. This is the result of intense collaborative work across different tasks in multiple WPs.

Annex

Band of Influence (BOI) characterization of analysed prototypes

In RISE-6G deliverable D2.4 [D2.4], the concept of BOI has been introduced. A RIS has an influence on impinging waves with a carrier frequency that is limited in the BoI. It is expected that the BoI of a RIS may not perfectly match the spectrum bandwidth of the wireless network for which it is used. In some cases, a RIS operated by one operator for a given spectrum bandwidth, may have an impact on another operator using a neighbour spectrum bandwidth. This may happen when the RIS's BoI overlaps the two spectrums.

It is therefore important to characterize the BoI of a RIS. It is expected that the BoI of a RIS may not exceed the BoI of one single UC. Therefore, characterizing the UC behaviour in the frequency domain is sufficient. In this section, we propose a first attempt to characterise the BoI of several UCs of RISs developed in the RISE-6G project:

- A Varactor based RIS UC
- A One-bit Transmissive RIS UC
- A Two-bit Transmissive RIS UC

For all UCs, the following information is provided:

- the principle;
- the S-parameters as a function of the frequency.

Varactor based RIS (V_RIS) UC

Principle

The UC is controllable via varactors (which themselves control the impedance loading the UC). The details on the UC design are available in [FRP+22] and [RBF+13].

It has the following main characteristics: the target frequency band is 5.15-5.35 GHz; the UC reradiates an impinging wave with a phase and amplitude; depending on the voltage that is applied to the varactors, the phase and the amplitude will vary; the UC ensures a continuous control of the phase and amplitude.

S-Parameters as a function of the frequency

Figure a illustrates the simulated UC.

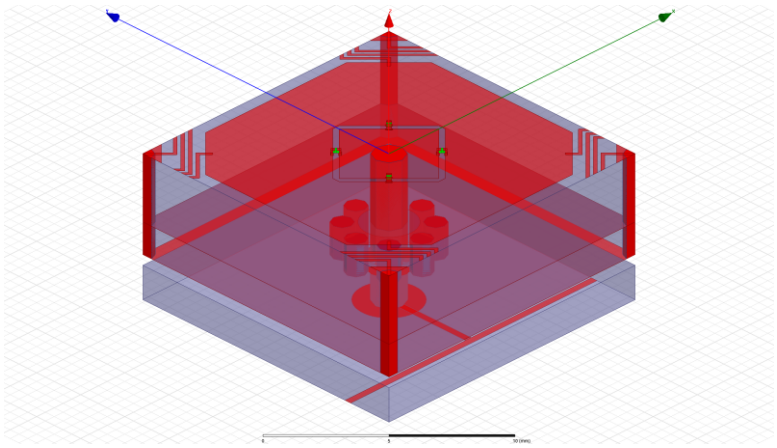

Figure a Simulated UC

Figure b illustrates the simulated UC reflection coefficient (S11) phase using High Frequency Simulation Software (HFSS) tool, under normal incidence.

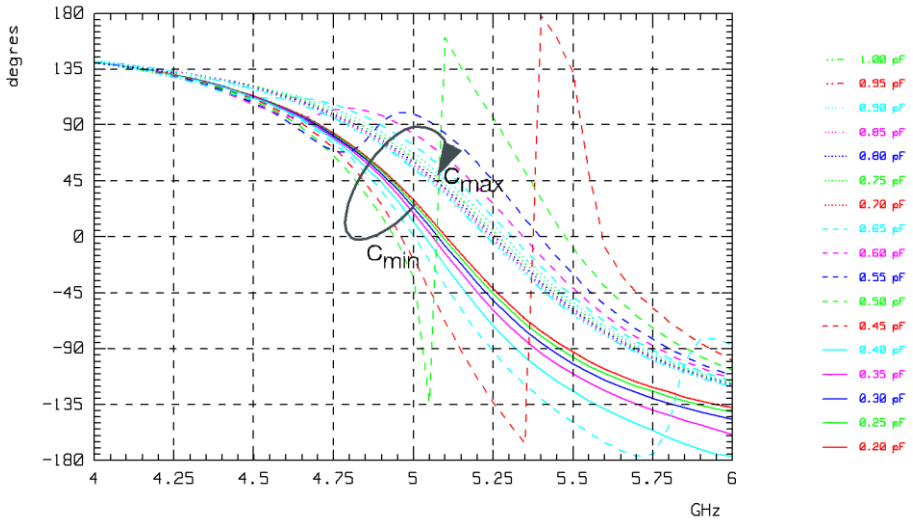

Figure b Simulated phase (in degrees) of the reflection coefficient (S11) for the normal incidence, for various voltages (in volts), as a function of the frequency (in GHz)

Figure c illustrates the simulated UC reflection coefficient (S11) amplitude using HFSS tool, under normal incidence.

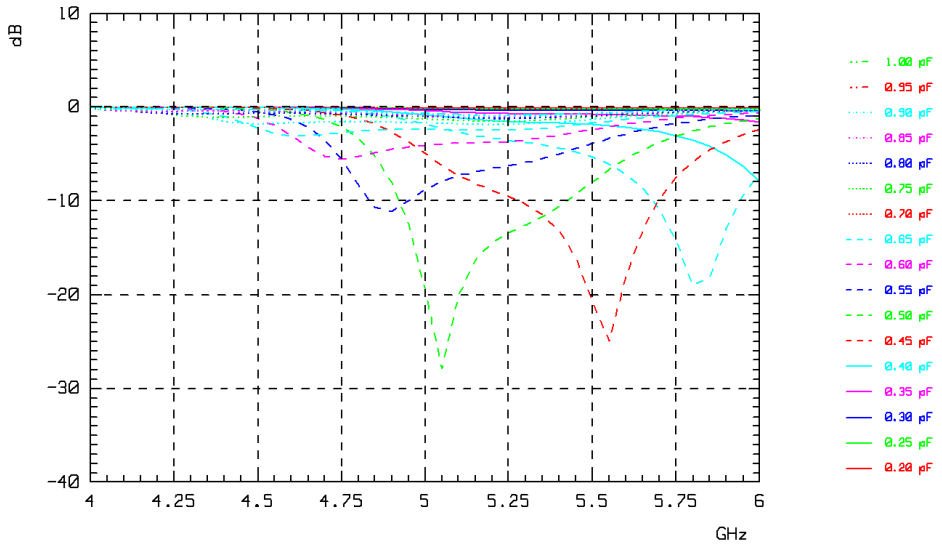

Figure c Simulated amplitude (in dB) of reflection coefficient (S11) for the normal incidence (HFSS), and for various loading capacity values (in pF), as a function of the frequency (in GHz)

Figure d illustrates the prototype RIS which is used for test and validation measurements.

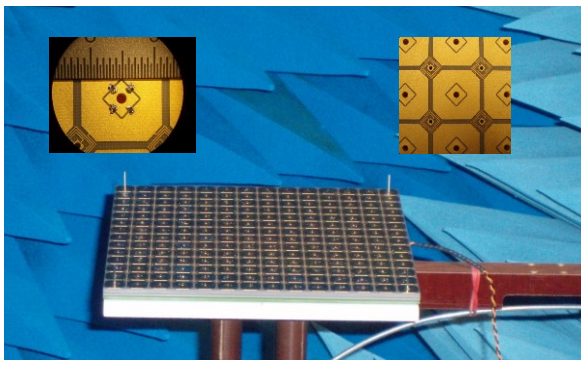

Figure d Measured RIS and UC Prototype

Figure e illustrates the measured reflection coefficient (S11) amplitude.

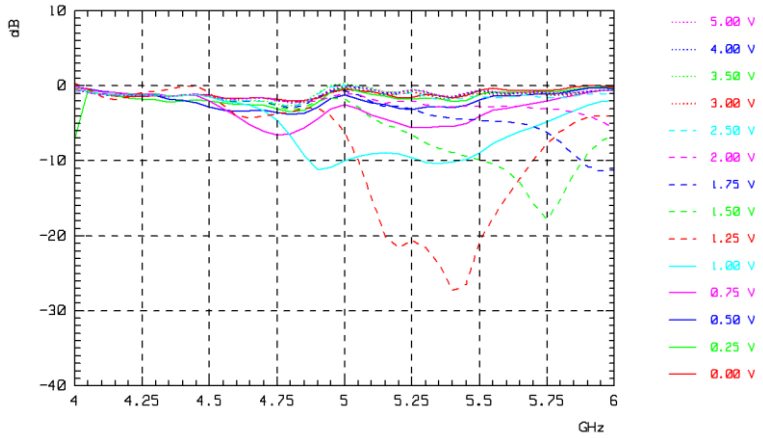

Figure e Measured amplitude (in dB) of reflection coefficient (S11) for the normal incidence (HFSS), and for various loading capacity values (in pF), as a function of the frequency (in GHz)

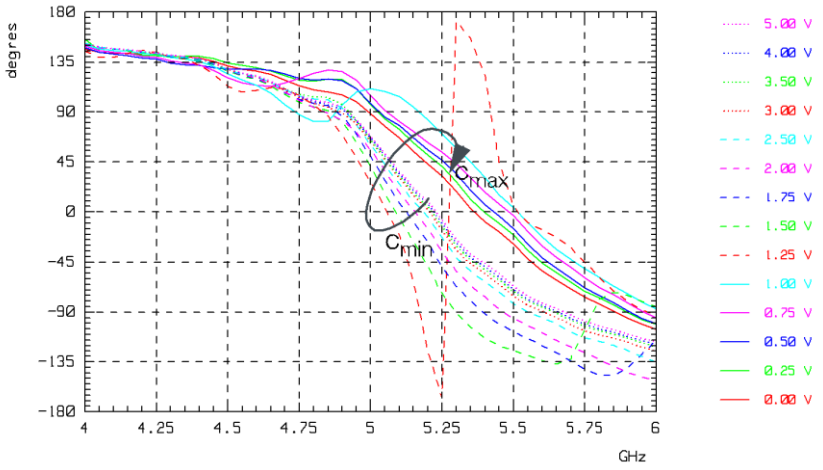

Figure f Measured phase (in degrees) of the reflection coefficient (S11) for the normal incidence, for various voltages (in volts), as a function of the frequency (in GHz)

Figure f illustrates the measured reflection coefficient (S11) phase.

One-bit Transmissive RIS (T_RIS_1bit) UC

This section provides models of a One-bit Transmissive RIS hardware implementations based on PIN-Diodes, designed by CEA-LETI in the framework of the H2020 RISE-6G Project.

Principle

Figure g below depicts the UC, which has the following characteristics:

- Frequency band: 21-35GHz.

- Four metal layers : Receiving and Transmitting Patches, Biasing Lines (Tx sides), and Ground Plane.
- The RIS is illuminated from the receiving patch side.
- On the Tx patch, the alternation of the diodes state will produce a 180° phase difference.
- The UC ensures a 1bit phase quantization in transmission.

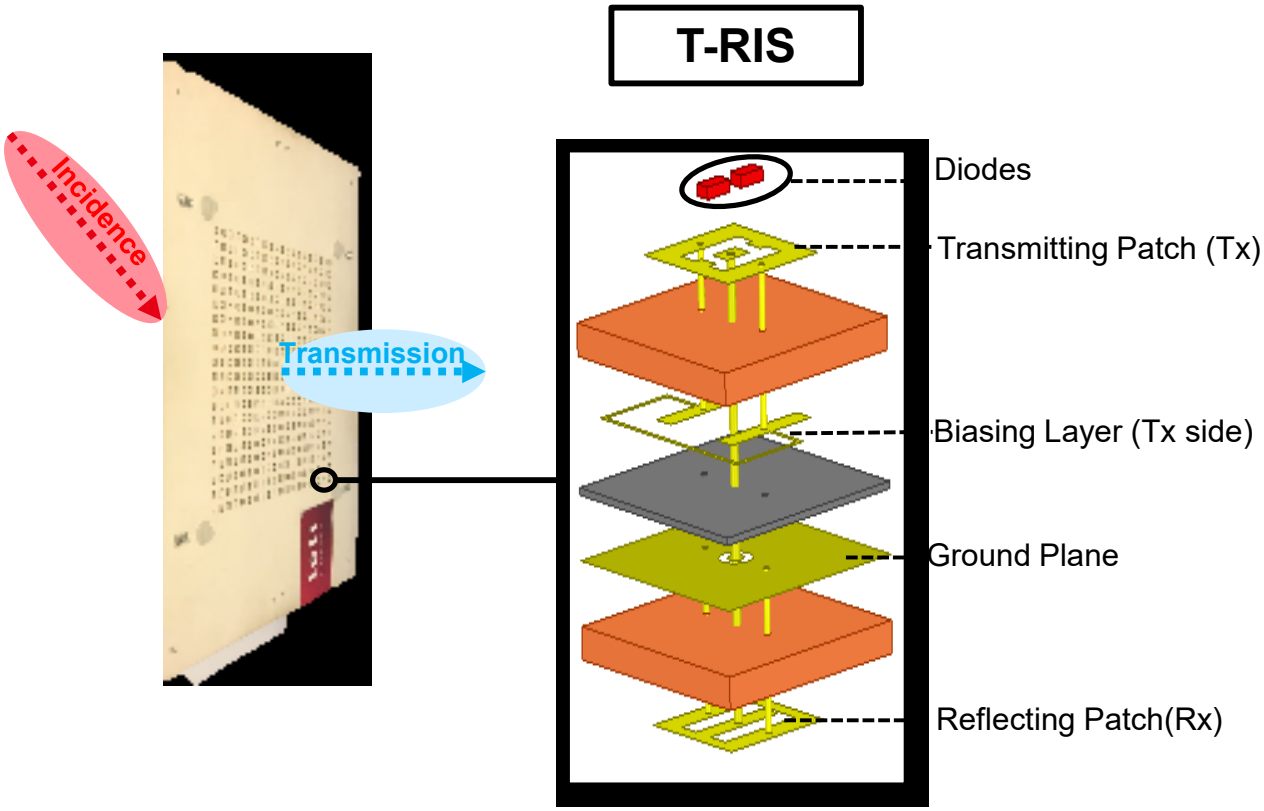

Figure g UC Principle

S-Parameters

Figure h and Figure i illustrate the simulation Setup:

1. Periodic Boundary Conditions
2. Two Floquet Ports

In this simulation the transmissive RIS is studied to check the capability of scanning the beam in transmission.

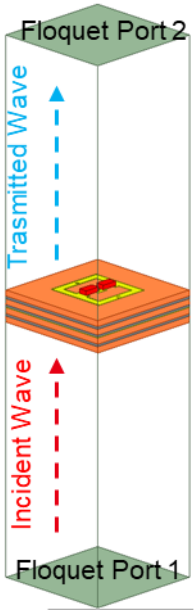

Figure h Simulated Ports of the UC

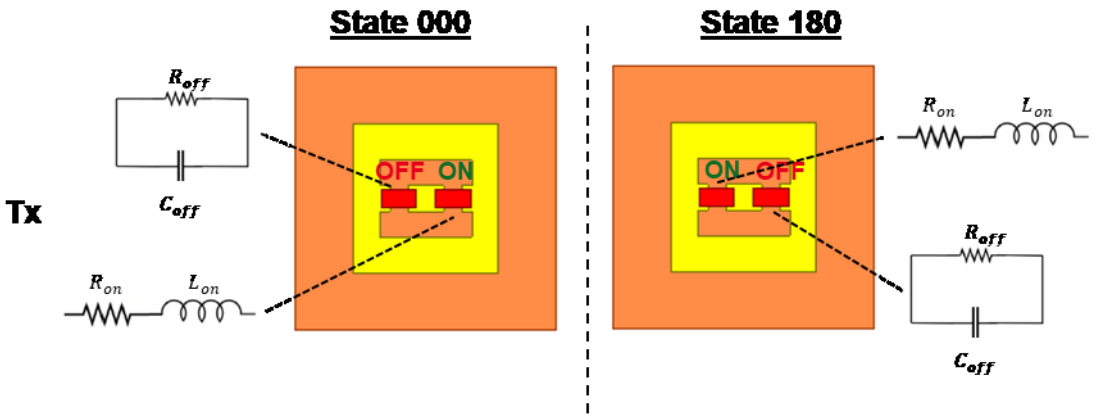

Active elements values:

$$R_{on} = 4{,}2ohm;\ L_{on} = 0{,}05\text{nH};\ R_{off} = 300Kohm;\ C_{off} = 0{,}042pf$$

Figure i Simulation States of the UC

Figure j illustrates the magnitude and phase of S-parameters as a function of frequency, obtained by simulation.

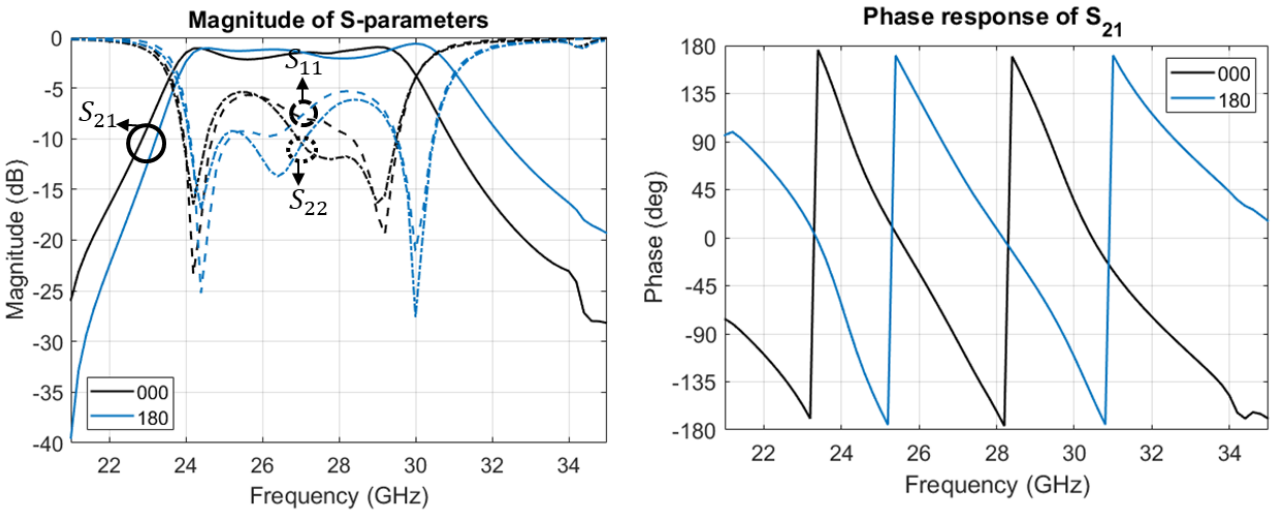

Figure j Magnitude and Phase of S-Parameters as a function of frequency

Two-bit Transmissive RIS (T_RIS_2bit) UC

This section provides models of a two-bit transmissive RIS hardware implementation based on PIN-Diodes, designed by CEA-LETI in the framework of the H2020 RISE-6G Project.

Principle

Figure k below depicts the UC, which has the following characteristics:

- Frequency band: 27-31GHz
- Six metal layers: Reflecting and Transmitting Patches, Two Biasing Lines (Tx and Rx sides),DC connection and Ground Plane
- Same analogy for the Rx patch but when it is operating in transmission mode thus 90° phase difference is produced
- For the Tx patch, the alternation of the diodes state will produce a 180° phase difference
- The UC can have a 2-bit phase quantization in transmission

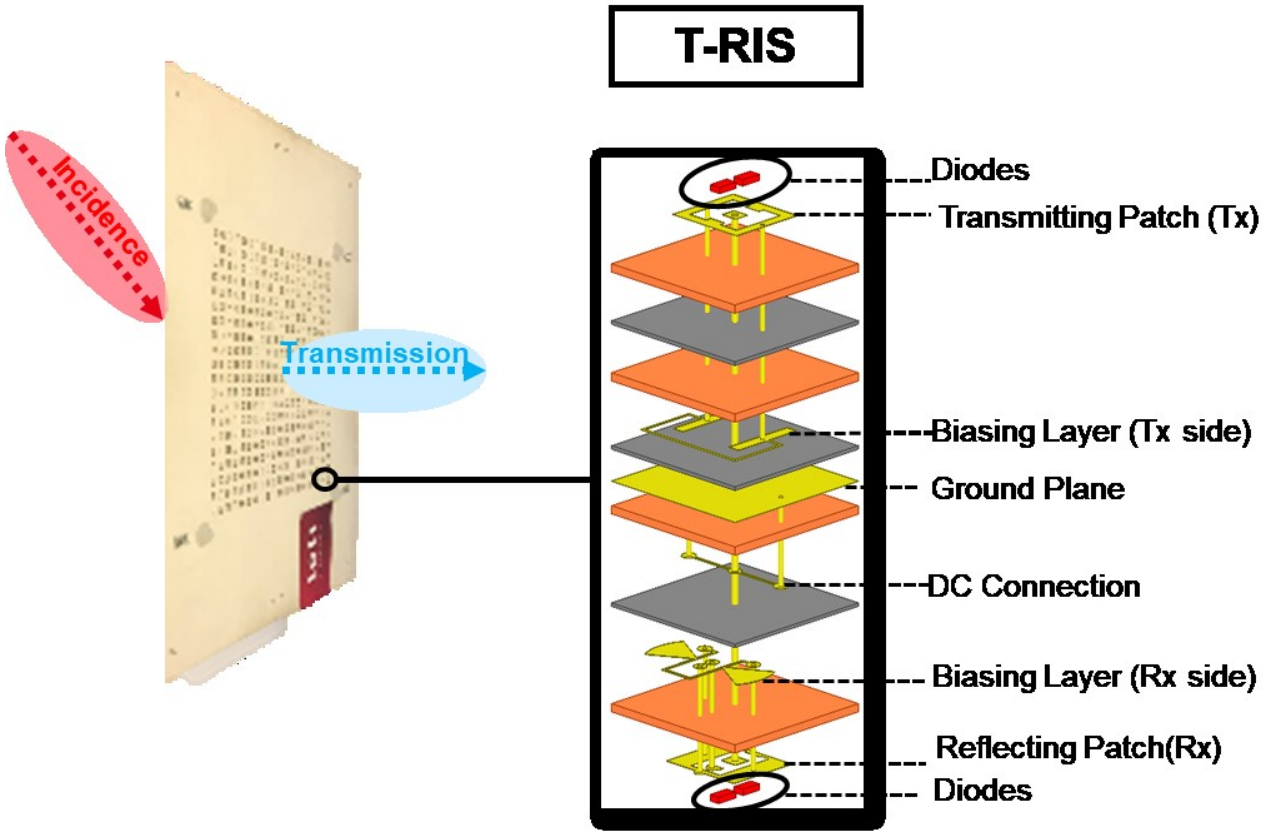

Figure k UC Principle

S-Parameters

Figure l and **Figure m** illustrate the simulation Setup:

1. Periodic Boundary Conditions
2. Two Floquet Ports

In this simulation the transmissive RIS is studied to check the capability of scanning the beam in transmission.

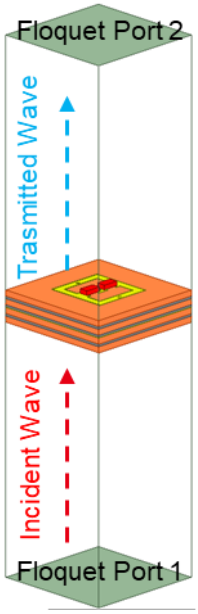

Figure l Simulation Assumptions

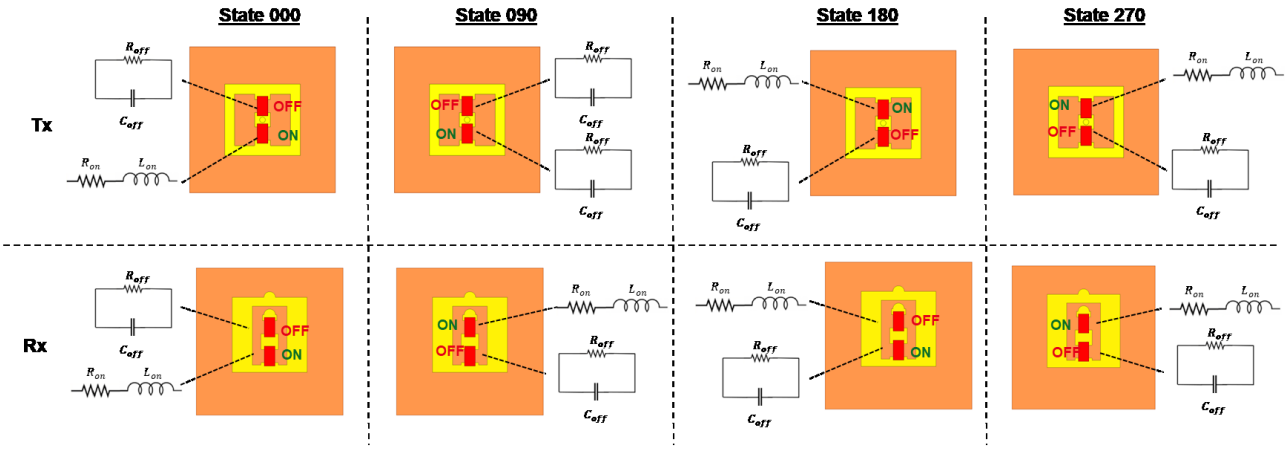

Figure m Simulation Assumptions

Figure n illustrates the magnitude and phase of S-parameters as a function of frequency, obtained by simulation.

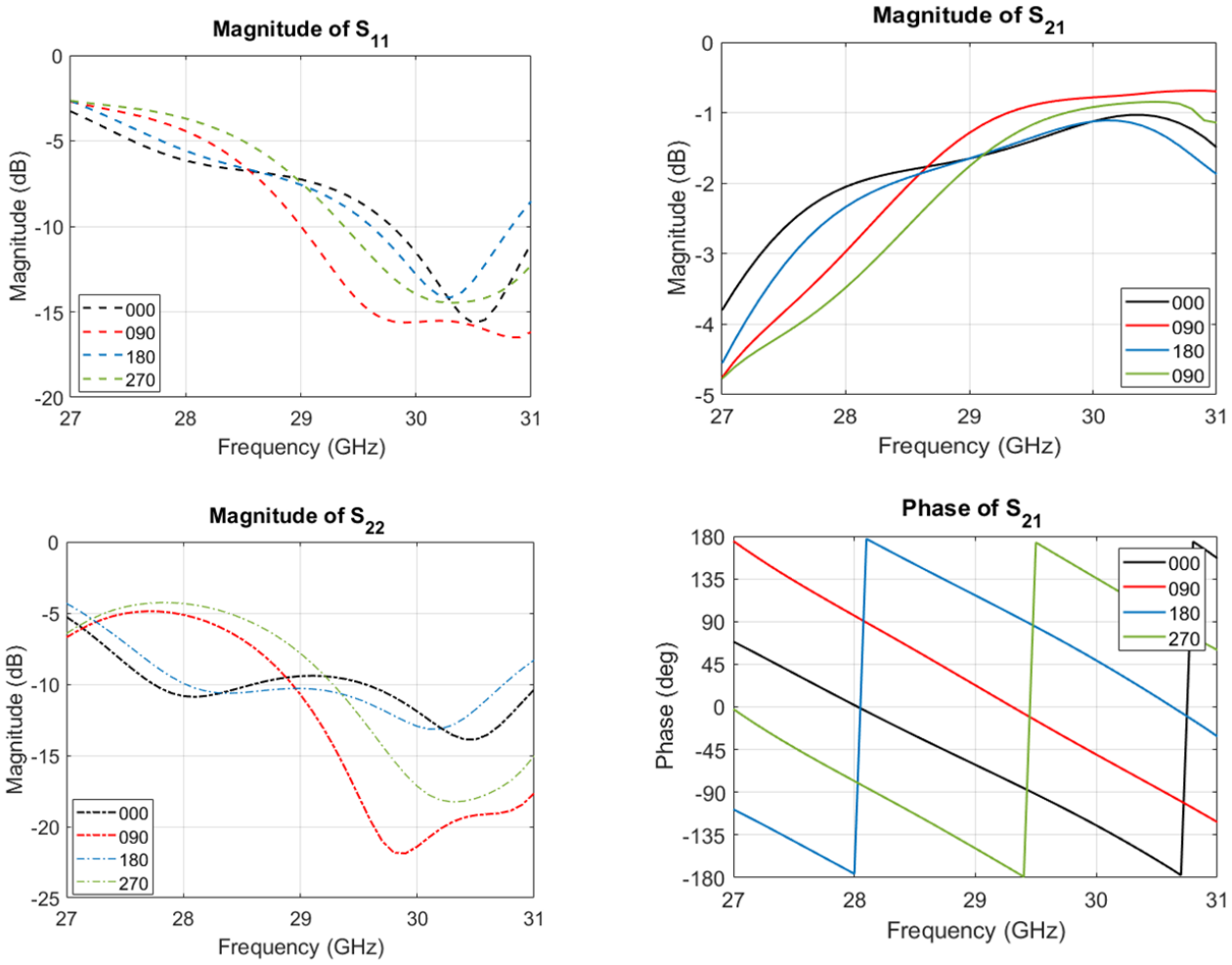

Figure n Magnitude and Phase of S-Parameters as a function of frequency

5 References

[AAS14]	L. R. Arnaut, M. I. Andries, J. Sol and P. Besnier, "Evaluation Method for the Probability Distribution of the Quality Factor of Mode-Stirred Reverberation Chambers," in IEEE Transactions on Antennas and Propagation, vol. 62, no. 8, pp. 4199-4208, Aug. 2014, doi: 10.1109/TAP.2014.2327642.
[AAS21]	I. Alamzadeh, G. C. Alexandropoulos, N. Shlezinger, and M. F. Imani, "A reconfigura-ble intelligent surface with integrated sensing capabilities," Springer Nature Scientific Re-ports, to appear, 2021.
[AAT16]	V. S. Asadchy, M. Albooyeh, S. N. Tcvetkova, A. Dıaz-Rubio, Y. Ra'di, and S. A. Tretyakov, "Perfect control of re-flection and refraction using spatially dispersive metasurfaces," Phys. Rev. B 94, 075142 - 19 August 2016.
[ACN10]	Allegretti M., Colaneri M., Notarpietro R., Gabella M., Perona G.E., “Simulation in urban environment of a 3d ray tracing propagation model based on building database preprocessing”, XXVIII General Assembly of International Union of Radio Science, New Delhi, India, October 2005.
[ADD21]	A. Abrardo, D. Dardari, M. Di Renzo and X. Qian, "MIMO Interference Channels Assisted by Reconfigurable Intelligent Surfaces: Mutual Coupling Aware Sum-Rate Optimization Based on a Mutual Impedance Channel Model," in IEEE Wireless Communications Letters, vol. 10, no. 12, pp. 2624-2628, Dec. 2021.
[ADR21]	A. Abrardo, D. Dardari, M. Di Renzo, and X. Qian, “MIMO interference channels assisted by reconfigurable intelligent surfaces: Mutual coupling aware sum-rate optimization based on a mutual impedance channel model”, IEEE Wireless Commun. Lett., vol. 10, no. 12, pp. 2624-2628, 2021.
[AFR10]	F. Aguado Agelet, A. Formella, J. M. Hernando Rabanos, F. Isasi de Vicente and F. Perez Fontan, "Efficient ray-tracing acceleration techniques for radio propagation modeling", IEEE Transactions on Vehicular Technology, vol. 49, no. 6, pp. 2089-2104, Nov. 2000, doi: 10.1109/25.901880.
[AES+22]	A. Albanese, G. Encinas-Lago, V. Sciancalepore, X. Costa-Pérez, D. -T. Phan-Huy and S. Ros, "RIS-Aware Indoor Network Planning: The Rennes Railway Station Case," ICC 2022 - IEEE International Conference on Communications, 2022, pp. 2028-2034, doi: 10.1109/ICC45855.2022.9838688.
[AG12]	L. R. Arnaut and G. Gradoni, "Probability Distribution of the Quality Factor of a Mode-Stirred Reverberation Chamber," in IEEE Transactions on Electromagnetic Compatibility, vol. 55, no. 1, pp. 35-44, Feb. 2013.
[AG15]	L. R. Arnaut and G. Gradoni, "Probability Distribution of the Coherence Bandwidth of a Reverberation Chamber," in IEEE Transactions on Antennas and Propagation, vol. 63, no. 5, pp. 2286-2290, May 2015.
[AKG15]	K. Achouri, B. A. Khan, S. Gupta, G. Lavigne, M. A. Salem, and C. Caloz, "Synthesis of electromagnetic metasurfaces: principles and illustrations", EPJ Applied Metamaterials, vol. 2, p. 12, 2015.
[ARA19]	B. Addissie,J. Rodgers, T. Antonsen, “Extraction of the coupling impedance in overmoded cavities,” Wave motion, Apr 1;87:123-31, 2019.
[ASA21]	G. C. Alexandropoulos, N. Shlezinger, I. Alamzadeh, M. F. Imani, H. Zhang, and Y. C. Eldar, "Hybrid reconfigurable intelligent metasurfaces: Enabling simultaneous tunable reflections and sensing for 6G wireless communications," [Online] https://arxiv.org/pdf/2104.04690.pdf, 2021.
[ASC151]	K. Achouri, M. A. Salem, and C. Caloz, "General metasurface synthesis based on susceptibility tensors", IEEE Trans. Antennas Propag., vol. 63, no. 7, pp. 2977-2991, Jul. 2015.

[ASC152]	K. Achouri, M. A. Salem, and C. Caloz, "Electromagnetic metasurface performing up to four independent wave transformations", in 2015 IEEE Conference on Antenna Measurements Applications (CAMA), Nov 2015, pp. 1-3.
[AV20]	G. C. Alexandropoulos and E. Vlachos, "A hardware architecture for reconfigurable intelligent surfaces with minimal active elements for explicit channel estimation," in Proc. IEEE International Conference on Acoustics, Speech, and Signal Processing, Barcelona, Spain, 4-8 May 2020, pp. 9175-9179.
[B12]	C. A. Balanis, Advanced engineering electromagnetics. John Wiley & Sons, 2012.
[B15]	Constantine A. Balanis, “Antenna Theory: Analysis and Design, 4th Edition”, Wiley, 2015
[BG20]	J. Budhu and A. Grbic, "Perfectly Reflecting Metasurface Reflectarrays: Mutual Coupling Modeling Between Unique Elements Through Homogenization," in IEEE Transactions on Antennas and Propagation, vol. 69, no. 1, pp. 122-134, Jan. 2021, doi: 10.1109/TAP.2020.3001450.
[BGM15]	L. Bastianelli, L. Giacometti, V. Mariani Primiani, and F. Moglie, "Effect of absorber number and positioning on the power delay profile of a reverberation chamber," in 2015 IEEE International Symposium on Electromagnetic Compatibility (EMC), Dresden, Germany, Aug. 2015, pp. 422-427.
[BKS19J]	C. Bucheli et al., "Reconfigurable intelligent surfaces: Bridging the gap between scattering/reflection", arXiv:1912.05344, 2019.
[BLY92]	J. H. Beggs, R. J. Luebbers, K. S. Yee, and K. S. Kunz, "Finite-difference time-domain implementation of surface impedance boundary conditions", IEEE Trans. Antennas Propag., vol. 40, no. 1, pp. 49-56, Jan. 1992.
[BMB17]	M. Barazzetta, D. Micheli, L. Bastianelli, R. Diamanti, M. Totta, P. Obino, R. Lattanzi, F. Moglie, V. Mariani Primiani, A comparison between different reception diversity schemes of a 4G-LTE base station in reverberation chamber: a deployment in a live cellular network, IEEE Trans. Electromagn. Compat. 59 (6) (2017) 2029-2037. doi:10.1109/TEMC.2017.2657122.
[BMM20]	M. Bodehou, E. Martini, S. Maci, I. Huynen, and C. Craeye, "Multibeam and beam scanning with modulated metasur-faces," IEEE Trans. Antennas Propag., vol. 68, no. 3, pp. 1273-1281, Mar. 2020.
[CCR21]	D. Chappell, J.J. Crofts, M. Richter, and G. Tanner. "A direction preserving discretization for computing phase-space densities." SIAM Journal on Scientific Computing 43, no. 4, B884-B906, 2021.
[DAH98]	D. A. Hill, “Plane wave integral representation for fields in reverberation chambers,” IEEE Trans. Electromagn. Compat., vol. 40, no. 3, pp. 209-217, Aug. 1998.
[DCD20]	L. Di Palma, A. Clemente, L. Dussopt, R. Sauleau, P. Potier, and P. Pouliguen, "Circularly-polarized reconfigurable transmitarray in Ka-band with beam scanning and polarization switching capabilities," IEEE Trans. Antennas Propag., vol. 65, pp. 529-540, Feb. 2017.
[DCS20]	F. Diaby, A. Clemente, R. Sauleau, K. Pham, and L. Dussopt, "2-bit reconfigurable unit-cell and electronically steera-ble transmitarray at Ka-band," IEEE Trans. Antennas Propag., accepted for publication, 2020.
[DDT21]	M. Di Renzo, F. H. Danufane, S. Tretyakov, "Communication Models for Reconfigurable Intelligent Surfaces: From Surface Electromagnetics to Wireless Networks Optimization," arXiv: 2110.00833, 2021.

[DFV+07]	V. Degli-Esposti, F. Fuschini, E. M. Vitucci, G. Falciasecca, “Measure- ment and modelling of scattering from buildings,” IEEE Trans. Antennas Propag., vol. 55 no 1, pp. 143–153, Jan. 2007
[DKT22]	A. Díaz-Rubio, S. Kosulnikov and S. A. Tretyakov, "On the Integration of Reconfigurable Intelligent Surfaces in Real-World Environments: A Convenient Approach for Estimation Reflection and Transmission," in IEEE Antennas and Propagation Magazine, vol. 64, no. 4, pp. 85-95, Aug. 2022, doi: 10.1109/MAP.2022.3169396.
[DGL20]	C. Della Giovampaola, F. Camminita, G. Labate, E. Martini, and S. Maci, "Reconfigurable metasurface antenna for 5G base stations," in Proc. EuCAP, Copenhagen, Denmark, 2020, pp. 1-6.
[DT21]	A. Diaz-Rubio and S. A. Tretyakov, “Macroscopic modeling of anoma- lously reflecting metasurfaces: Angular response and far-field scattering,” IEEE Trans. Antennas Propag., vol. 69, no. 10, pp. 6560–6571, Oct. 2021
[DZD20]	M. Di Renzo et al., "Smart Radio Environments Empowered by Reconfigurable Intelligent Surfaces: How It Works, State of Research, and The Road Ahead," in IEEE Journal on Selected Areas in Communications, vol. 38, no. 11, pp. 2450-2525, Nov. 2020, doi: 10.1109/JSAC.2020.3007211.
[FBP21]	A. Farasatul, V. Blakaj, S. Phang, T. M. Antonsen, S. C. Creagh, G. Gradoni, and G. Tanner. "Wireless power distributions in multi-cavity systems at high frequencies," Proceedings of the Royal Society A 477, no. 2245, 20200228, 2021.
[FCB21]	F. Costa and M. Borgese, "Electromagnetic Model of Reflective Intelligent Surfaces," in *IEEE Open Journal of the Communications Society*, vol. 2, pp. 1577-1589, 2021, doi: 10.1109/OJCOMS.2021.3092217.
[FLL04]	F. Falcone, T. Lopetegi, M.A.G. Laso, J.D. Baena, J. Bonache, M. Beruete, R. Marqu ?es, F. Mart?n, and M. Sorolla, "Babinet principle applied to the design of metasurfac-es and metamaterials", Phys. Rev. Lett., 93(19):197401, Nov 2004.
[F17]	O. Franek, “Phasor alternatives to Friis’ transmission equation,” IEEE Antennas and Wireless Propagation Letters, vol. 17, no. 1, pp. 90–93, 2017.
[FRP+22]	R. Fara, P. Ratajczak, D. -T. Phan-Huy, A. Ourir, M. Di Renzo and J. de Rosny, "A Prototype of Reconfigurable Intelligent Surface with Continuous Control of the Reflection Phase," in IEEE Wireless Communications, vol. 29, no. 1, pp. 70-77, February 2022.
[FSA22]	R. Faqiri, C. Saigre-Tardif, G. C. Alexandropoulos, N. Shlezinger, M. F. Imani, and P. del Hougne, "PhysFad: Physics-based end-to-end channel modeling of RIS-parametrized environments with adjustable fading," IEEE Transactions on Wireless Communications, to appear, 2022.
[GAA15]	G. Gradoni, T. M. Antonsen, S. M. Anlage and E. Ott, "A Statistical Model for the Excitation of Cavities Through Apertures," in IEEE Transactions on Electromagnetic Compatibility, vol. 57, no. 5, pp. 1049-1061, Oct. 2015, doi: 10.1109/TEMC.2015.2421346.
[GD21]	G. Gradoni and M. Di Renzo, "End-to-End Mutual Coupling Aware Communication Model for Reconfigurable Intelligent Surfaces: An Electromagnetic-Compliant Approach Based on Mutual Impedances," in IEEE Wireless Communications Letters, vol. 10, no. 5, pp. 938-942, May 2021, doi: 10.1109/LWC.2021.3050826.
[GDA16]	J. Gil Gil, Z. B. Drikas, T. D. Andreadis and S. M. Anlage, "Prediction of Induced Voltages on Ports in Complex, Three-Dimensional Enclosures With Apertures, Using the Random Coupling Model," in IEEE Transactions on Electromagnetic Compatibility, vol. 58, no. 5, pp. 1535-1540, Oct. 2016.

[GDD+21]	Gradoni, G., Di Renzo, M., Diaz-Rubio, A., Tretyakov, S., Caloz, C., Peng, Z., Alu, A., Lerosey, G., Fink, M., Galdi, V. and Cui, T.J., 2021. Smart radio environments. arXiv preprint arXiv:2111.08676.
[GFE09]	Guidelines for evaluation of radio interface technologies for IMT Advanced, International Telecommunication Union - ITU Report M.2135-1, Dec. 2009.
[GLL+21]	Gros, J.B., Lerosey, G., Lemoult, F., Lodro, M., Greedy, S. and Gradoni, G., 2022. Multi-path fading and interference mitigation with Reconfigurable Intelligent Surfaces. arXiv preprint arXiv:2206.08290.
[GR21]	G. Gradoni and M. Di Renzo, “End-to-end mutual coupling aware communication model for reconfigurable intelligent surfaces: An electromagnetic-compliant approach based on mutual impedances”, IEEE Wireless Commun. Lett., vol. 10, no. 5, pp. 938-942, 2021.
[GTB16]	S. B. Glybovski, S. A. Tretyakov, P. A. Belov et al., "Metasurfaces: From microwaves to visible," Phys. Rep., vol. 634, pp. 1 - 72, 2016.
[GYX14]	G. Gradoni, J.H. Yeh, B. Xiao, T.M. Antonsen, S.M. Anlage, E. Ott, “Predicting the statistics of wave transport through chaotic cavities by the random coupling model: A review and recent progress.,” Wave Motion, 51(4), 606-621, 2014.
[HC09]	T. H. Hand and S. A. Cummer, "A dynamic frequency selective surface using addressable metamaterials," 2009 IEEE Ant. and Prop. Soc. Inter. Symp., 2009.
[HC09]	T. H. Hand and S. A. Cummer, "A dynamic frequency selective surface using addressable metamaterials," 2009 IEEE Ant. and Prop. Soc. Inter. Symp., 2009.
[HGG16]	T. Hartmann, G. Tanner, G. Xie, D. Chappell, J. Bajars. "Modelling of high-frequency structure-borne sound transmission on FEM grids using the Discrete Flow Mapping technique," in Journal of Physics: Conference Series, vol. 744, no. 1, p. 012237. IOP Publishing, 2016.
[HGS08]	T.H. Hand, J. Gollub, S. Sajuyigbe, S.A. Cummer, and D.R. Smith, "Characterization of Complementary Electric Field Coupled (CELC) Resonator Surfaces", App. Phys. Lett. 93, 212504, 2008.
[HGS08]	T.H. Hand, J. Gollub, S. Sajuyigbe, S.A. Cummer, and D.R. Smith, "Characterization of Complementary Electric Field Coupled (CELC) Resonator Surfaces", App. Phys. Lett. 93, 212504, 2008.
[HMS+22]	D. Hanna, M. S. Melo, F. Shan and F. Capolino, "A Versatile Polynomial Model for Reflection by a Reflective Intelligent Surface with Varactors," 2022 IEEE International Symposium on Antennas and Propagation and USNC-URSI Radio Science Meeting (AP-S/URSI), 2022, pp. 679-680, doi: 10.1109/AP-S/USNC-URSI47032.2022.9887248.
[HMT19]	T. Hartmann, S. Morita, G. Tanner, and D. J. Chappell, “High-frequency structure- and air-borne sound transmission for a tractor model using Dynamical Energy Analysis”, Wave Motion, vol. 87, pp. 132–150, Apr. 2019, doi: 10.1016/j.wavemoti.2018.09.012.
[HSP12]	C. L. Holloway, H. A. Shah, R. J. Pirkl, K. A. Remley, D. A. Hill, and J. Ladbury, "Early time behavior in reverberation chambers and its effect on the relationships between coherence bandwidth, chamber decay time, RMS delay spread, and the chamber buildup time," IEEE Trans. Electromagn. Compat., vol. 54, no. 4, pp. 714-725, Aug. 2012.

[HVS17]	S. Hubert, A. Vallecchi, A. Schuchinsky and C. Craeye, "Modeling of impedance-loaded sub-wavelength metasurfaces," 2017 International Conference on Electromagnetics in Advanced Applications (ICEAA), 2017, pp. 1041-1044, doi: 10.1109/ICEAA.2017.8065438.
[JRZ21]	Z.-M. Jiang, M. Rihan, P. Zhang, L. Huang, Q. Deng, J. Zhang, and E. M. Mohamed, "Intelligent reflecting surface aided dual-function radar and communication system," IEEE Sensors Letters, 2021.
[JYL20]	X. Jia, F. Yang, X. Liu, M. Li and S. Xu, "Fast Nonuniform Metasurface Analysis in FDTD Using Surface Susceptibility Model," IEEE Transactions on Antennas and Propagation, vol. 68, no. 10, pp. 7121-7130, Oct. 2020.
[KYE13]	Theoretical analysis on reflection properties of reflectarray unit cells using quality factors," IEEE Trans. Antennas Prop., vol. 61, no. 1, pp. 201–210, Jan. 2013.
[LBD10]	Z. Lai, N. Bessis, G. de la Roche, P. Kuonen, J. Zhang and G. Clapworthy, "On the use of an Intelligent Ray Launching for indoor scenarios", Proceedings of the Fourth European Conference on Antennas and Propagation, 2010, pp. 1-5.
[LPP19]	C. Liaskos, G. Pirialakos, A. Pitilakis, S. Abadal, A. Tsioliaridou, A. Tasolamprou, O. Tsilipakos, N. Kantartzis, S. Ioannidis, E. Alarcon, A. Cabellos, M. Kafesaki, A. Pitsillides, K. Kossifos, J. Georgiou, and I. F. Akyildiz, "ABSense: Sensing Electromagnetic Waves on Metasurfaces via Ambient Compilation of Full Absorption," arXiv:1907.04811, July 2019.
[LSR14]	C. L"tb„ck Patan,, A. Sk†rbratt, R. Rehammar, C. Orlenius, Basic and advanced MIMO OTA testing of wireless devices using reverberation chamber, in: Proc. 8th Eur. Conf. Antennas Propag., The Hague, Netherlands, 2014, pp. 3488-3492. doi:10.1109/EuCAP.2014.6902581
[LU19]	J. S. Lu et al., "A discrete environment-driven GPU-based ray launching algorithm", IEEE Trans. Antennas Propag., vol. 67 no. 2, pp. 1558–2221,
[LU20]	J. S. Lu et al., "A discrete environment-driven GPU-based ray launching algorithm", IEEE Trans. Antennas Propag., vol. 67 no. 2, pp. 1180–1192, Feb. 2019, doi: 10.1109/TAP.2018.2880036.
[MAP06]	F. Moglie and A. P. Pastore, "FDTD analysis of plane wave superposition to simulate susceptibility tests in reverberation chambers," in *IEEE Transactions on Electromagnetic Compatibility*, vol. 48, no. 1, pp. 195-202, Feb. 2006, doi: 10.1109/TEMC.2006.870793.
[MBB20]	V. M. Primiani et al., "Reverberation chambers for testing wireless devices and systems," in IEEE Electromagnetic Compatibility Magazine, vol. 9, no. 2, pp. 45-55, 2nd Quarter 2020, doi: 10.1109/MEMC.2020.9133241.
[MBB21]	D. Micheli et al., "MIMO 4x4 vs. MIMO 2x2 Performance Assessment of a Real Life LTE Base Station in a Reverberation Chamber", in AEU - International Journal of Electronics and Communications, vol. 129, 2021, https://doi.org/10.1016/j.aeue.2020.153500
[MBC17]	D. Micheli, M. Barazzetta, C. Carlini, R. Diamanti, V. Mariani Primiani, F. Moglie, Testing of the carrier aggregation mode for a live LTE base station in reverberation chamber, IEEE Trans. Veh. Technol. 66 (4) (2017) 3024-3033. doi: 10.1109/TVT.2016.2587662.
[MBI17]	L. Pulido-Mancera, P. Bowen, M. Imani, N. Kundtz and D. Smith, "Polarizability extraction of complementary metamaterial elements in waveguides for aperture modeling", Phys. Rev. B, vol. 96, no. 23, Nov. 2017.

[MBI17]	L. Pulido-Mancera, P. Bowen, M. Imani, N. Kundtz and D. Smith, "Polarizability extraction of complementary metamaterial elements in waveguides for aperture modeling", Phys. Rev. B, vol. 96, no. 23, Nov. 2017.
[MBJ19]	Q. Ma, G. D. Bai, H. B. Jing, C. Yang, L. Li, and T. J. Cui, "Smart metasurface with self-adaptively reprogrammable functions," Light Sci Appl, vol. 8, p. 98, Oct. 2019.
[MBM15]	D. Micheli, M. Barazzetta, F. Moglie, V. Mariani Primiani, Power boosting and compensation during OTA testing of a real 4G LTE base station in reverberation chamber, IEEE Trans. Electromagn. Compat. 57 (4) (2015) 623-634. doi: 10.1109/TEMC.2015.2434277.
[MBM16]	F. Moglie, L. Bastianelli, V. Mariani Primiani, "Reliable Finite-Difference Time-Domain Simulations of Reverberation Chambers by Using Equivalent Volumetric Losses", IEEE Trans. on EMC, vol. 58, no.3, pp. 653-660 June 2016.
[MH73]	J. Mautz and R. Harrington, "Modal analysis of loaded N-port scatterers," in IEEE Transactions on Antennas and Propagation, vol. 21, no. 2, pp. 188-199, March 1973, doi: 10.1109/TAP.1973.1140431.
[MM22]	E. Martini and S. Maci, "Theory, Analysis, and Design of Metasurfaces for Smart Radio Environments," in Proceedings of the IEEE, vol. 110, no. 9, pp. 1227-1243, Sept. 2022, doi: 10.1109/JPROC.2022.3171921.
[MPD20]	S. Ma, S. Phang, Z. Drikas, B. Addissie, R. Hong, V. Blakaj, G. Gradoni, G. Tanner, T.M. Antonsen, E. Ott, S.M. Anlage, “Efficient statistical model for predicting electromagnetic wave distribution in coupled enclosures,” Physical Review Applied, 8;14(1):014022, Jul 2020.
[MSG+21]	P. Mursia, V. Sciancalepore, A. Garcia-Saavedra, L. Cottatellucci, X. C. Pérez and D. Gesbert, "RISMA: Reconfigurable Intelligent Surfaces Enabling Beamforming for IoT Massive Access," in IEEE Journal on Selected Areas in Communications, vol. 39, no. 4, pp. 1072-1085, April 2021, doi: 10.1109/JSAC.2020.3018829.
[IN10]	M. T. Ivrlač and J. A. Nossek, "Toward a Circuit Theory of Communication," in IEEE Transactions on Circuits and Systems I: Regular Papers, vol. 57, no. 7, pp. 1663-1683, July 2010, doi: 10.1109/TCSI.2010.2043994.
[NJS21]	M. Najafi, V. Jamali, R. Schober and H. V. Poor, "Physics-Based Modeling and Scalable Optimization of Large Intelligent Reflecting Surfaces," in IEEE Transactions on Communications, vol. 69, no. 4, pp. 2673-2691, April 2021, doi: 10.1109/TCOMM.2020.3047098.
[O16]	S. J. Orfanidis, Electromagnetic Waves and Antennas, CE Department, Rutgers University, 2016.
[P05]	D. M. Pozar, Microwave Engineering (3th Edition), New York, John Wiley & Sons, 2005.
[P22]	P. del Hougne. (2022) PhysFad. [Online]. Available: https://github.com/philipp-delhougne/PhysFad
[PBH22]	D.-T. Phan-Huy, Y. Bénedic, S. Herraiz-Gonzales, P; Ratajczak,“Creating and Operating Areas With Reduced Electromagnetic Field Exposure Thanks to Recon-figurable Intelligent Surfaces” IEEE International Workshop on Signal Processing Advances in Wireless Communications (SPAWC), Oulu, Finland, 4-6th July 2022.
[PDP12]	Propagation data and prediction methods for the planning of indoor radiocommunication systems and radio local area networks in the frequency range 900 MHz to 100 GHz, International Telecommunication Union - ITU Recommendation P.1238-7, Feb. 2012.

[PDS1]	Multipath and Doppler Characterization of an Electromagnetic Environment by Massive MDT Measurements From 3G and 4G Mobile Terminals, https://ieeexplore.ieee.org/document/8620498
[PRL21]	Z. Peng, C. Ross, Q. Jian Lim, G. Gradoni, Engineering Reflective Metasurfaces with Ising Hamiltonian and Quantum Annealing, under review, IEEE Transactions on Antennas and Propagation, (https://www.techrxiv.org/articles/preprint/Engineering_Reflective_Metasurfaces_with_Ising_Hamiltonian_and_Quantum_Annealing/14615031/1), 2021.
[PTG18]	S. Phang, M. T. Ivrlac, G. Gradoni, S. C. Creagh, G. Tanner and J. A. Nossek, "Near-Field MIMO Communication Links," in IEEE Transactions on Circuits and Systems I: Regular Papers, vol. 65, no. 9, pp. 3027-3036, Sept. 2018, doi: 10.1109/TCSI.2018.2796305.
[PTH20]	U. R. Patel, P. Triverio and S. V. Hum, "A Fast Macromodeling Approach to Efficiently Simulate Inhomogeneous Electromagnetic Surfaces," in IEEE Transactions on Antennas and Propagation, vol. 68, no. 11, pp. 7480-7493, Nov. 2020, doi: 10.1109/TAP.2020.3000857.
[QD21]	X. Qian and M. D. Renzo, "Mutual Coupling and Unit Cell Aware Optimization for Reconfigurable Intelligent Surfaces," in IEEE Wireless Communications Letters, vol. 10, no. 6, pp. 1183-1187, June 2021, doi: 10.1109/LWC.2021.3061449.
[QR21]	X. Qian and M. Di Renzo, “Mutual coupling and unit cell aware optimization for reconfigurable intelligent surfaces”, IEEE Wireless Commun. Lett., vol. 10, no. 6, pp. 1183-1187, 2021.
[RBF+13]	P. Ratajczak, P. Brachat, J. Fargeas, J. Baracco, “C-band active reflectarray based on high impedance surface,” in Proc. IEEE International Symposium on Phased Array Systems and Technology, Waltham, USA, Oct. 2013.
[RDT22]	M. Di Renzo, F. H. Danufane, and S. Tretyakov, “Communication models for reconfigurable intelligent surfaces: From surface electromagnetics to wireless networks optimization”, Proc. of the IEEE, vol. 110, no. 9, pp. 1164-1209, Sep. 2022.
[RGC22]	M. Di Renzo, V. Galdi and G. Castaldi, “Modeling the Mutual Coupling of Reconfigurable Metasurfaces”, Oct. 2022.
[RMG22]	M. Rossanese, P. Mursia, A. Garcia-Saavedra, V. Sciancalepore, A. Asadi, and X. Costa-Perez, “Designing, Building, and Characterizing RF Switch-based Reconfigurable Intelligent Surfaces”, in Proceedings of the 16th ACM Workshop on Wireless Network Testbeds, Experimental Evaluation & Characterization (WiNTECH'22), Sydney, NSW, Australia, 2022.
[RVC19]	J. R. Reis, M. Vala, R. F. S. Caldeirinha, "Review paper on transmitarray antennas," IEEE Access, vol. 7, pp. 94171-94188, Jun. 2019.
[SA21]	Sarkar, D. and Antar, Y., 2021. Electromagnetic Insights into Path Loss Modelling of IRS-Assisted SISO Links: Method-of-Moment Based Analysis. Frontiers in Communications and Networks, p.59.
[SCM22]	S. Shen, B. Clerckx and R. Murch, "Modeling and Architecture Design of Reconfigurable Intelligent Surfaces Using Scattering Parameter Network Analysis," in IEEE Transactions on Wireless Communications, vol. 21, no. 2, pp. 1229-1243, Feb. 2022, doi: 10.1109/TWC.2021.3103256.
[SGF15]	A. Sorrentino, A. Gifuni, G. Ferrara, and M. Migliaccio, "Mode-stirred reverberating chamber autocorrelation function: model, multifrequency measurements

	and applications," IET Science, Measurement Technology, vol. 9, no. 5, pp. 547-554, 2015.
[SMS06]	D. Schurig, J. J. Mock, and D. R. Smith, "Electric-field-coupled resonators for nega-tive permittivity metamaterials", Appl. Phys. Lett. 88, 041109, 2006.
[SMS06]	D. Schurig, J. J. Mock, and D. R. Smith, "Electric-field-coupled resonators for neg-ative permittivity metamaterials", Appl. Phys. Lett. 88, 041109, 2006.
[SN17]	I. V. Shadrivov and D. N. Neshev, Tunable Metamaterials, World Scientific, 2017, chapter 9, pp. 387-418.
[SPV00]	D.R. Smith, W.J. Padilla, D. Vier, S. Nemat-Nasser, and S. Schultz, "Composite me-dium with simultaneously negative permeability and permittivity", Phys. Rev. Lett., 84(18):4184-4187, May 2000.
[SPV00]	D.R. Smith, W.J. Padilla, D. Vier, S. Nemat-Nasser, and S. Schultz, "Composite me-dium with simultaneously negative permeability and permittivity", Phys. Rev. Lett., 84(18):4184-4187, May 2000.
[SYM17]	D. R. Smith, O. Yurduseven, L. P. Mancera, P. Bowen, and N. B. Kundtz, "Analysis of a waveguide fed metasurface antenna," Phys. Rev. App., Nov. 2017.
[SYM17]	D. R. Smith, O. Yurduseven, L. P. Mancera, P. Bowen, and N. B. Kundtz, "Analysis of a waveguide fed metasurface antenna," Phys. Rev. App., Nov. 2017.
[TAA21]	A. Taha, M. Alrabeiah and A. Alkhateeb, "Enabling Large Intelligent Surfaces With Compressive Sensing and Deep Learning," in IEEE Access, vol. 9, pp. 44304-44321, March 2021.
[TAF95]	A. Taflove, "Computational Electrodynamics: The Finite-Difference Time-Domain Method", Norwood, MA: Artech House, 1995.
[TBM14]	J. P. Turpin, J. A. Bossard, K. L. Morgan et al., "Reconfigurable and tunable met-amaterials: A review of the theory and applications," HINDAWI Int. J. Antennas. Propag., vol. 2014, 429837, 18 pages, 2014.
[TMN16]	V. Torres, F. Mesa, M. Navarro-Cia, R. Rodriguez-Berral, M. Beruete, and F. Me-dina, “Accurate circuit modeling of fishnet structures for negative-index-medium applications,” IEEE Trans. Microw. Theory Tech., vol. 64, no. 1, pp. 15-26, Jan. 2016.
[V07]	O. Roy and M. Vetterli, "The effective rank: A measure of effective dimensional-ity," 2007 15th European Signal Processing Conference, 2007, pp. 606-610.
[VAC16]	Y. Vahabzadeh, K. Achouri and C. Caloz, "Simulation of Metasurfaces in Finite Dif-ference Techniques", in IEEE Transactions on Antennas and Propagation, vol. 64, no. 11, pp. 4753-4759, Nov. 2016, doi: 10.1109/TAP.2016.2601347.
[VCA18]	Y. Vahabzadeh, N. Chamanara, K. Achouri and C. Caloz, "Computational Analysis of Metasurfaces", in IEEE Journal on Multiscale and Multiphysics Computational Techniques, vol. 3, pp. 37-49, 2018, doi: 10.1109/JMMCT.2018.2829871.
[VCC18]	Y. Vahabzadeh, N. Chamanara, and C. Caloz, "Generalized sheet transition condi-tion FDTD simulation of metasurface", IEEE Trans. Antennas Propag., vol. 66, no. 1, pp. 271-280, Jan. 2018.
[VVD+22]	V. Degli-Esposti, E. M. Vitucci, M. Di Renzo and S. Tretyakov, "Reradiation and Scattering from a Reconfigurable Intelligent Surface: A General Macroscopic Model," in IEEE Transactions on Antennas and Propagation, doi: 10.1109/TAP.2022.3149660.
[WRY+22]	R. J. Williams, P. Ramírez-Espinosa, J. Yuan and E. de Carvalho, "Electromagnetic Based Communication Model for Dynamic Metasurface Antennas," in IEEE Trans-actions on Wireless Communications, vol. 21, no. 10, pp. 8616-8630, Oct. 2022, doi: 10.1109/TWC.2022.3167783.

[XD21]	X. Qian and M. D. Renzo, "Mutual Coupling and Unit Cell Aware Optimization for Reconfigurable Intelligent Surfaces," in IEEE Wireless Communications Letters, vol. 10, no. 6, pp. 1183-1187, June 2021.
[YCY16]	H. Yang, X. Caon F. Yang, J. Gao, S. Xu, M. Li, X. Chen, Y. Zhao, Y. Zheng, and S. Li, "A programmable metasur-faces with dynamic polarization, scattering and focus-ing control," Scientific Reports, 6, 35692, Oct. 2016.
[YFY19]	Yang, Fan, and Yahya Rahmat-Samii. Surface Electromagnetics: With Applications in Antenna, Microwave, and Optical Engineering. 2019.
[YGK11]	N. Yu et al., “Light Propagation with Phase Discontinuities: Generalized Laws of Reflection and Refraction”, Science, vol. 334, no. 6054, pp. 333–337, Oct. 2011, doi: 10.1126/science.1210713.
[ZSA21]	H. Zhang, N. Shlezinger, I. Alamzadeh, G. C. Alexandropoulos, M. F. Imani, and Y. C. Eldar, "Channel estimation with simultaneous reflecting and sensing reconfig-urable intelligent metasurfaces," IEEE International Workshop on Signal Pro-cessing Advances in Wireless Communications, Lucca, Italy, 27-30 Sept. 2021.
[ZZD22]	S. Zeng, H. Zhang, B. Di, Y. Liu, M. Di Renzo, Z. Han, H. V. Poor, and L. Song, “Intel-ligent Omni-Surfaces: Reflection-Refraction Circuit Model, Full-Dimensional Beam-forming, and System Implementation”, IEEE Transactions on Communications, Sept. 2022.